Fall 12-2014

Fatigue Damage Prognosis of Internal Delamination in Composite Plates Under Cyclic Compression Loadings Using Affine Arithmetic as Uncertainty Propagation Tool

Audrey J-M Gbaguidi
Embry-Riddle Aeronautical University

Scholarly Commons Citation

Gbaguidi, Audrey J-M, "Fatigue Damage Prognosis of Internal Delamination in Composite Plates Under Cyclic Compression Loadings Using Affine Arithmetic as Uncertainty Propagation Tool" (2014). *Doctoral Dissertations and Master's Theses*. 267.
https://commons.erau.edu/edt/267

FATIGUE DAMAGE PROGNOSIS OF INTERNAL DELAMINATION IN COMPOSITE PLATES UNDER CYCLIC COMPRESSION LOADINGS USING AFFINE ARITHMETIC AS UNCERTAINTY PROPAGATION TOOL

By

Audrey J-M Gbaguidi

A Thesis Submitted to the College of Engineering Department of Aerospace Engineering
in Partial Fulfillment of the Requirements for the Degree of
Master of Science in Aerospace Engineering

Embry-Riddle Aeronautical University
Daytona Beach, Florida
December 2014

FATIGUE DAMAGE PROGNOSIS OF INTERNAL DELAMINATION IN COMPOSITE PLATES UNDER CYCLIC COMPRESSION LOADINGS USING AFFINE ARITHMETIC AS UNCERTAINTY PROPAGATION TOOL

By

Audrey J-M Gbaguidi

This thesis was prepared under the direction of the candidate's Thesis Committee Chair, Dr. DaeWon Kim, Assistant Professor, Daytona Beach Campus and Thesis Committee Member Dr. Frank Radosta, Professor, Daytona Beach Campus and Dr. Jeff Brown, Associate Professor, Daytona Beach Campus, and has been approved by the Thesis Committee. It was submitted to the Department of Aerospace Engineering in partial fulfillment of the requirements for the degree of Master of Science in Aerospace Engineering

Thesis Review Committee:

DaeWon Kim, Ph.D.
Committee Chair

Frank Radosta, Ph.D.
Committee Member

Jeff Brown, Ph.D.
Committee Member

Yi Zhao, Ph.D.
Graduate Program Chair

Robert Oxley, Ph.D.
Associate Vice President of Academics

12-5-14
Date

Dedication

To the memory of my grandmother
Augustine Dossa

Acknowledgements

It gives me pleasure to acknowledge the people that made this thesis possible, for all the support and strength that they have given to me.

I would like to thank my advisor, Dr. DaeWon Kim for his guidance, supervision, and above all, the moral support for the last two years. Throughout my thesis work he encouraged me to develop independent thinking and fostered a stress-free working relationship which was crucial for the completion of this work.

I would like to thank Dr. Jeff Brown for all of his advice and suggestions which have been greatly appreciated.

I would like to thank Dr. Frank Radosta for serving on the committee and for giving me his time out of his busy schedule to review my thesis and all of his advice.

I would like to express my deep appreciation to my friend, Boutros Azizi, for his support and encouragement throughout my thesis work.

I would like to share this achievement with my mother Juliette, my father Septime, my sisters and brother and my aunt Josianne for their love, motivation, support and faith in me.

Finally, I would like to thank my friends, and my relatives for all the support they gave me.

Table of Contents

List of Figures

List of Tables

Nomenclature

a = Crack half-length

a_{rc} = Critical crack half-length

a_o = Initial crack half-length

$\bar{a}$ = Dimensionless crack length

$(a\,)_n$ = Crack half-length at cycle n

C = Paris-Erdogan exponent or compliance

C( ) = Kardomateas law coefficient

C_I = Pure Mode I coefficient

C_{II} = Pure Mode II coefficient

dn = Cycle step-size

E = Normal modulus of elasticity

$G(\,)$ = Strain energy release rate

$\tilde{G}(\,)$ = Normalized strain energy release rate

G_I^c = Pure Mode I energy fracture toughness

G_{II}^c = Pure Mode II energy fracture toughness

h = Delamination thickness

k = Ratio of coefficients at pure Mode I and II

K_I = Mode I stress intensity factor

K_{I_c} = Fracture toughness in Mode I of crack opening

K_{II} = Mode II stress intensity factor

ΔK = Range of the stress intensity factor

l = Delamination half-length

l_o = Initial delamination half-length

l_{cr} = Critical delamination half-length

l_{tr} = Unstable-to-stable transition half-length

L = Composite plate half-length

m = Paris-Erdogan exponent
m( ) = Kardomateas exponent
m_I = Pure Mode I exponent
m_{II} = Pure Mode II exponent
n = Number of iteration
N = Number of load cycles
N_o = Initial number of cycles
N_f = Final number of cycles
R = Load ratio for Paris Erdogan law
t = Delamination thickness
T = Composite plate thickness
w = Width half-length
Y( ) = Geometric dimensionless parameter
α = Load ratio in Kardomateas law
$\Delta\sigma$ = Range of the cyclic stress amplitude
$\Delta\tilde{G}$ = Range of the energy release rate
Γ_0( ) = Mixed-mode adjusted fracture toughness
Ψ ( ) = Mode mixity
μ = Ratio of the exponents m at pure Mode I and II
ε_{cr} = Euler’s critical strain for the delaminated layer
ε_0 = Maximum applied strain
ξ = Amplitude of buckling deflection
δ = Vertical displacement
P = Load

Abstract

Researcher: Audrey Jean-Miche Gbaguidi

Title: Fatigue Damage Prognosis of Internal Delamination in Composite Plates
Under Cyclic Compression Loadings Using Affine Arithmetic as
Uncertainty Propagation Tool

Institution: Embry-Riddle Aeronautical University

Degree: Master of Science in Aerospace Engineering

Year: 2014

Structural health monitoring (SHM) has become indispensable for reducing maintenance costs and increasing the in-service capacity of a structure. The increased use of lightweight composite materials in aircraft structures drastically increased the effects of fatigue induced damage on their critical structural components and thus the necessity to predict the remaining life of those components. Damage prognosis, one of the least investigated fields in SHM, uses the current damage state of the system to forecast its future performance by estimating the expected loading environments. A successful damage prediction model requires the integration of technologies in areas like measurements, materials science, mechanics of materials, and probability theories, but most importantly the quantification of uncertainty in all these areas.

In this study, Affine Arithmetic is used as a method for incorporating the uncertainties due to the material properties into the fatigue life prognosis of composite plates subjected to cyclic compressive loadings. When loadings are compressive in nature, the composite plates undergo repeated buckling-unloading of the delaminated layer which induces mixed modes I and II states of stress at the tip of the delamination in the plates. The Kardomateas model-based prediction law is used to predict the growth of the delamination, while the integration of the effects of the uncertainties for modes I and II coefficients in the fatigue life prediction model is handled using Affine Arithmetic. The Mode I and Mode II interlaminar fracture toughness and fatigue characterization of the composite plates are first experimentally studied to obtain the material coefficients and fracture toughness, respectively. Next, these obtained coefficients are used in the Kardomateas law to predict the delamination lengths in the composite plates while using Affine Arithmetic to handle their uncertainties. At last, the fatigue characterization of the composite plates during compressive-buckling loadings is experimentally studied, and the delamination lengths obtained are compared with the predicted values to check the performance of Affine Arithmetic as an uncertainty propagation tool.

Chapter 1

Introduction

1.1 Significance

As mankind's technological imagination has become more of a reality in modern society, many engineering materials and structural systems have been progressively developed and have become increasingly complicated. Although these advanced systems have helped us in shaping our society and have provided much convenience, they occasionally result in unexpected blemishes and cause catastrophic failures. The possible causes for these failures could vary; however, some of the structural failures might be due to inaccurate design, miscalculated analysis, and/or manufacturing mistakes. Also, due to the repeated use and aging of the materials, a fatigue crack may initiate and propagate with time, leading to structural failure in these systems. For some structures that require high reliability, the severity of the fatigue damage must be identified and the remaining useful life should be accurately predicted for decision-making. Damage prognosis, as investigated in this paper, is related to forewarning of any undesirable structural failures through embedded sensor systems and data analysis.

The methods in prognosis are usually classified into data-driven, model-based and hybrid method [1-3]. The data-driven prediction is based on the data collected from structural health monitoring (SHM). This method tends to work generally for short term prediction and is usually not reliable for long term prediction under realistic service conditions, due to different uncertainties from material properties, manufacturing process, loading conditions, measurement errors as well as numerical evaluations [4]. It also requires a costly learning process for every new operational condition. The model-based method, on the other hand, uses the physics of failure approach (mathematic model) that allows accurate and both short and long term predictions. However, one of the drawbacks of this method is the rarity of model based equations for some of the failure mechanisms. The hybrid method is an approach combining these two methods and is relatively new in the prognosis fields. The general components of a damage prognosis process are shown in Figure 1.1. Because of the importance of uncertainty in any prediction method, the prognosis methods explained above can really not be used for serious and accurate health monitoring without coupling them to a tool that will propagate the uncertainty of the parameters these methods are based on into the predictions computed.

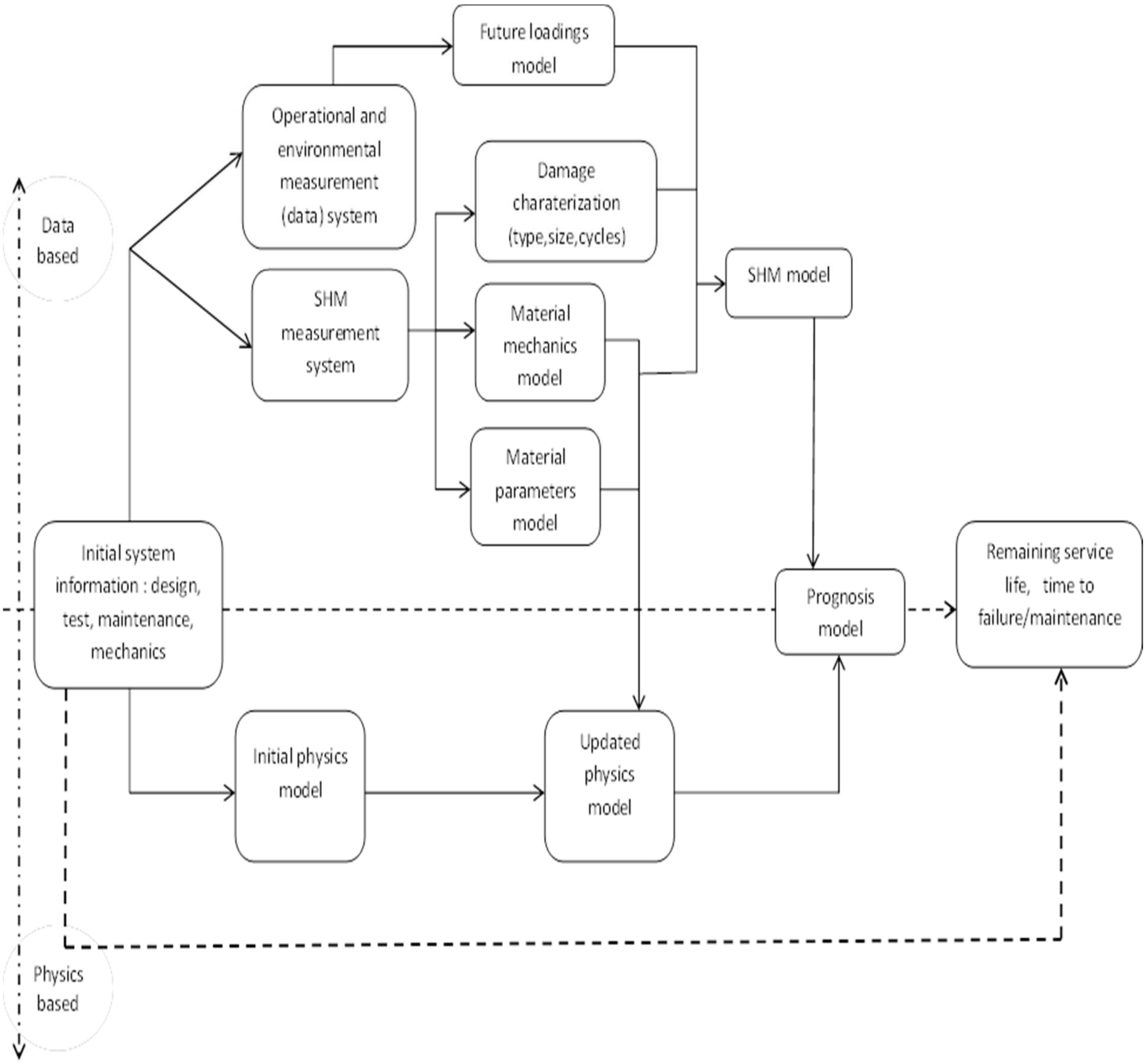

Figure 1.1. The General Components of a Damage Prognosis Process.

1.2 Sources of Uncertainty

Damage prediction in engineering structures involves three different types of uncertainty – physical variability, data uncertainty and model uncertainty – as discussed in [5].

Physical variability: The external loading state on aircraft structure components under service conditions depends on multiple factors, such as air flow, friction, air pressure and the weights of the different components. The variability of those factors are the reason for the stochastic nature of the loading state in damage prediction.

Also material properties are affected by many factors such as manufacturing process, sample composition, micro-structure, macro-structure and the errors in measurements. The material mechanics parameters such as fracture toughness, threshold stress intensity factor, and the material Paris Erdogan coefficients are all dependent of the factors cited above and should be treated as random variables.

Data uncertainty: The uncertainty in crack inspection data, including crack detection and measurement uncertainty due to the use of non-destructive evaluation (NDE) techniques, usually has a large impact on damage prediction. The probability distributions or range of values of some material properties are obtained from experiments and may be sparse or noisy. The loading data gathered might carry some measurement errors due to the environmental conditions they have been measured in.

Model uncertainty and errors: Different physics based models exist to predict specific damage characterization in more or less accurate ways. The errors induced by these different models, as well as the uncertainty in the choice of the right method for a specific damage state of loading conditions, should be considered. These errors and uncertainties, whether deterministic or stochastic occur at different stages of the prediction and may be combined in a linear, nonlinear, iterative or nested manner. In the case of the Kardomateas law studied in this work, model uncertainty usually comes from the uncertainty in the law coefficients such as C_I, C_{II}, m_I, m_{II}, K_{Ic}, K_{IIc}. The uncertainty of those parameters can be represented through their probability distribution or their range of values.

Chapter 2

Review of the Relevant Literature and Methodology

Model-based prognosis for crack growth has been actively investigated, as well as different ways of handling uncertainty, since the physics models for fatigue crack growth have been relatively well established compared to other failure mechanisms. Kulkarni and Achenbach [6] presented a methodology to predict macro crack-initiation, using a probabilistic method and the data from a pre-crack damage monitoring system. Orchard and Vachtsevanos [7] suggested an online particle filtering algorithm to handle the uncertain parameters for the crack growth of an UH-60 rotor gearbox. Leem *et al.* [8] studied the prognosis of crack damage under variable amplitude loading, using Huang's crack growth model and a particle filter algorithm for the estimation of uncertain parameters. Cross *et al.* [9] proposed prognosis based on Bayesian theory for the equivalent initial flaw size and crack growth. Ling and Mahadevan [10] presented a Bayesian Methodology to integrate the model-based prognosis using the Paris Erdogan law with online and offline SHM data in which the uncertainty due to loading conditions is handled by a Bayesian autoregressive integrated moving average (ARIMA) model. Worden and Manson studied the damage prognosis in an isotropic material using the Paris Erdogan law as the crack growth model [11]. They also studied the damage prognosis in a composite material using the Kardomateas delamination law [12]. In both studies, Interval Arithmetic is used to handle the uncertainty due to the model-based parameters. These results were compared to a case where a Monte Carlo analysis was used to handle those parameters uncertainty.

This work, will examine the fatigue damage prognosis of rectangular composite plates with an initial delamination, subjected to cyclic compression loading. First, the Kardomateas law is used as a damage growth model and the damage conditions it describes is explained. Then a general overview of Affine Arithmetic as well as its integration into the Kardomateas Law is explained. Affine Arithmetic is used to derive some mathematical equations that integrate the uncertainty of the model parameters in the Kardomateas law. The resulting equations can directly help to compute the lifetime range of the specimen, given the upper and lower values of the uncertain parameters. The Kardomateas law is built around different parameters characterizing, the Mode I and Mode II interlaminar fracture and fatigue. For that reason, the next part of this work is built around the experimental characterization of Mode I and Mode II interlaminar fracture and fatigue of composite plates in order to determine the Kardomateas law parameters as a range of values. The characterization of the mixed Modes I and II delamination growth in composite plates under cyclic compression is then experimentally examined. The delamination lengths are obtained using Thermal Imaging on the composite plates to accurately observe the delaminated layers. Affine Arithmetic is then used with the Kardomateas law to predict the delamination length in the same composite plates used in the experiments and the prediction is compared to the experimental results.

Chapter 3

Interval Arithmetic and Affine Arithmetic Method

In this chapter the usual method for computation with interval or range of values (Interval Arithmetic) is described and its main drawbacks discussed. The concept of Affine Arithmetic is then described as well as the derivations of Affine Arithmetic for the prognosis field.

3.1 Interval Arithmetic and Affine Arithmetic Concepts

The basic concepts and derivations of Affine Arithmetic used in this section are derived and well explained in [13].

Most of the uncertainty propagation tools are based on the use of the probability distributions of the uncertain parameters rather than their range values. One of the main drawback in the use of interval methods in numerical quantification, and more precisely in uncertainty quantification, is that the range estimation with standard Interval Arithmetic (IA) is usually too large, especially in complex expressions or iterative computations. The inherent assumption of IA, namely, that all the uncertain parameters vary independently over their given range, is usually not true when dealing with uncertainty. That is, there are usually mathematical relationships between some or all of the uncertain parameters. For that reason, the interval computed by interval arithmetic may be much wider than the exact range of the computed quantity. This problem is known as the “dependency problem”.

Affine Arithmetic (AA) is a self-validated numerical computation method that aims to solve the dependency problem in interval computations. AA keeps track of first-order correlations between uncertain parameters and the function computed. These correlations are automatically exploited in any operations of AA that leads to the computation of much better interval estimations than the ones with Interval Arithmetic. Also, AA implicitly provides a geometric representation for the joint range of related quantities that can be exploited to increase the efficiency of the interval method.

3.1.1 The Dependency Problem in Standard Interval Arithmetic

In Interval Arithmetic, quantities are represented by intervals and basic operations and functions are extended to operate on intervals. In AA, a quantity $x \in \mathbf{R}$ is represented by an interval $x \in [a,b]$, such that $a \leq x \leq b$. Basic arithmetic operations can be extended to intervals:

$$[a,b] + [c,d] = [a+c, b+d] \tag{3.1}$$

$$[a,b] - [c,d] = [a-d, b-c] \tag{3.2}$$

$$[a,b] \text{ x } [c,d] = \min(ac,ad,bc,bd), \max(ac,ad,bc,bd)] \tag{3.3}$$

$$[a,b] \,/\, [c,d] = [a,b] \text{ x } [1/d, 1/c] \quad (\text{with } c, d \neq 0) \tag{3.4}$$

It should be added that the lower bounds are rounded downwards and the upper bounds upwards. With the interval formulas for the basic operations and functions, any complex operation or function can be computed by combining these basic operations.

Overestimation happens frequently when a function f contains repeated variables in its formulation because the basic operations of IA given above assume that all the variables are independent. When the variables have some dependencies between them, not all of the combinations of values given by IA will be valid. The computed interval by IA will usually be smaller than the exact interval. This dependency problem gets worse with more complex functions. A simple but extreme example of IA computation happens when we consider the function $f(x) = x - x$. The exact value of that function is $\{0\}$. However, using IA operations formula for subtraction gives:

Assuming $x \in [a, b]$, $x - x = [a, b] - [a, b]$

$$= [a - b, b - a]$$

$$\neq \ 0$$

We see that the diameter of the computed interval is twice the diameter of $[a, b]$, instead of being zero. An example that shows the usual overestimation of IA is:

$f(x) = (20 - x)(20 + x), with\, x \in [-3, 3]$

Using IA addition formula we have:

$$(20 - x) = [17, 23]$$

$$(20 + x) = [17, 23]$$

$$(20 - x)(20 + x) = [289, 529]$$

The exact interval of f being $[391, 400]$ with a diameter of 9 whereas the IA computed interval diameter is 240, we can see the difficulty of IA in dealing with repeating variables.

When we rewrite $(x) = (20 - x)(20 + x) = 400 - x^2$, using IA gives :

$$x^2 = x * x = [-9, 9]$$

$$-x^2 = [-9, 9]$$

$$400 - x^2 = [391, 409]$$

The new computed interval now has ~~now~~ a diameter of 18 which is far better than 240. We see then the effect of repeating variables on the accuracy of IA.

3.1.2 Affine Arithmetic Concepts

While Interval Arithmetic represents quantities with intervals, in Affine Arithmetic a quantity x is represented by its affine form:

$$\hat{x} = x_0 + x_1\varepsilon_1 + x_2\varepsilon_2 + \cdots + x_n\varepsilon_n, \tag{3.5}$$

which is a function of the noise symbols ε_i and the floating-points coefficients x_i. Each noise symbol ε_i is a real parameter whose value is restricted to **U** = $[-1, +1]$ and is independent from the other noise parameters. The floating-point coefficient x_0 is called the central value of the affine form $\hat{x}$. The other floating-points coefficientsx_1,…, x_n are called the partial deviations linked to the noise parameters ε_1,…, ε_n. The number of noise parameters depends on the affine form. In fact different affine forms (representing different quantities) can use a different number of noise symbols, while some affine forms may share some noise parameters with other affine forms. Depending also on the accuracy of the quantity expressed by AA or its complexity, the same quantity can be expressed with just one noise symbol (simplest AA form) or with many more. Moreover affine forms provide the quantity expressed also in interval bounds: A quantity x expressed by Eq. (2.1) will have an interval bound $x \in [x_0 - r_x, x_0 + r_x]$, with $r_x = |x_1| + \cdots + |x_n|$, also called the total deviation of $\hat{x}$. Conversely, if $x \in [a, b]$, then x can be expressed with its simplest affine form:

$$\hat{x} = x_0 + x_1\varepsilon_1 \tag{3.6}$$

$$x_0 = (b + a)/2 \text{ and } x_1 = (b - a)/2 \tag{3.7}$$

$$b = (x_0 + x_1)/2 \text{ and } a = (x_0 - x_1)/2 \tag{3.8}$$

Eqs. (3.5), (3.6), (3.7) and (3.8) show that AA can, not only input or output quantities as interval bounds but also can be used for different levels of accuracy and complexity. But most importantly, as we shall see presently, affine forms give additional information that can be exploited to further bound the joint range of quantities.

3.1.3 Affine Arithmetic with Dependent (Uncertain) Quantities

The key property of AA for uncertainty computation is that two or more affine forms can share noise symbols. A noise symbol ε_1 is shared when it appears with non-zero coefficient in all affine forms in consideration. When this happens, the quantity defined by those affine forms are not completely independent: they have a partial dependency for each noise symbol shared by their affine forms. This dependency can be measured by the corresponding partial deviations.

For example, let's consider two quantities x and y defined by the affine forms:

$$\hat{x} = x_0 + x_1\varepsilon_1 + x_2\varepsilon_2 + \cdots + x_n\varepsilon_n$$

$$\hat{y} = y_0 + y_1\varepsilon_1 + y_2\varepsilon_2 + \cdots + y_n\varepsilon_n.$$

Anytime x_i and y_i are both non-zero, the values of x and y are partially dependent. Even though the affine forms above imply that x and y have a different interval bond of values, $x \in [x_0 - r_x, x_0 + r_x]$ and $y \in [y_0 - r_y, y_0 + r_y]$, the partial dependency implied by the shared noise symbols implies that the joint range Z of x and y is not simply the rectangle $R = [x_0 - r_x, x_0 + r_x] \times [y_0 - r_y, y_0 + r_y]$. In fact the joint range is

$$Z = \{(x, y) : \varepsilon_i \in \mathrm{U}, i = 1, \dots n\}.$$

In other words, Z is the image of the hypercube $\mathbf{U}^n$ under the affine transformation $\mathbf{R}^n \rightarrow \mathbf{R}^2$, given by :

$$\begin{pmatrix} x_0 \\ y_0 \end{pmatrix} + \begin{pmatrix} x_1 \dots x_n \\ y_1 \dots y_n \end{pmatrix} . (\varepsilon_1, \dots, \varepsilon_n)^T.$$

Therefore, Z is a Zonetope (convex polygon) that is centrally symmetric with respect to the point (x_0, y_0), the image of the origin $(0,\dots0) \in \mathbf{R}^n$. In general, the joint range of m affine forms is a zonotope in $\mathbf{R}^m$, that is, a centrally symmetric convex polytope in $\mathbf{R}^m$.

This geometric information provided by AA has immediate applications in geometric modeling. Let C be a parametric curve given by $\gamma : I$, where T is a subinterval of I. By representing $t \in$ T as an affine form and computing $\Upsilon(t) = \left(x(t), y(t)\right)$ for $t \ \in$ T with AA, we obtain, as explained above, a zonotope Z that contains P. To get a simpler enclosure for P, we compute the rectangle of minimal width that contains Z. If we do this for a covering of the domain I, we get a covering of C by rectangles (see Figure 3.1). When these coverings are organized hierarchically, we get a multi resolution representation that can be used to solve several geometric problems on C efficiently. In Figure 3.2 the rectangle approximation of a circle with Affine Arithmetic and Interval Arithmetic with the same tolerance are compared.

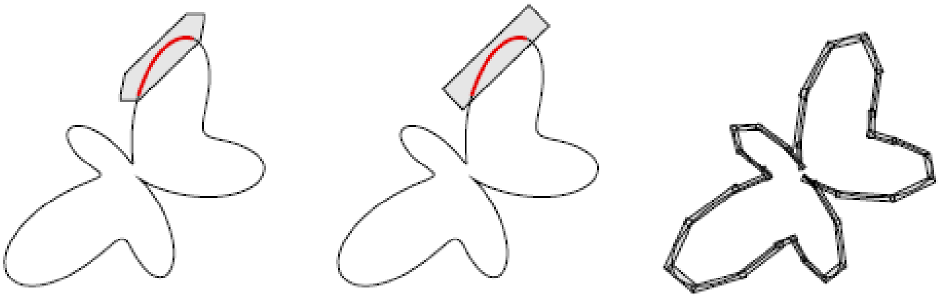

Figure 3.1. Approximation of a Parametric Curve with Rectangles Using AA [13].

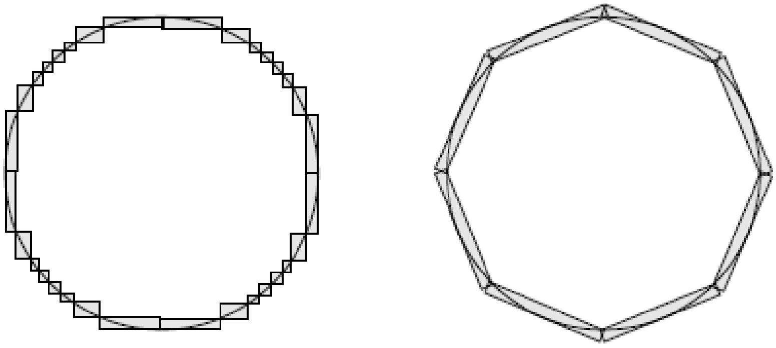

Figure 3.2. Comparison of Rectangle Approximation of a Circle Computed with Interval Arithmetic (left) and with Affine Arithmetic (right) Using the Same Tolerance [13].

3.1.4 Computing with Affine Arithmetic

As with IA, computations in Affine Arithmetic are performed by first extending basic operations (addition, subtraction) and functions to affine forms and then combining these operations to compute complex operations or functions. It is necessary to note that Affine Arithmetic's basic operations are only addition and subtraction.

Given two quantities x and y defined by the affine forms:

$$\hat{x} = x_0 + x_1\varepsilon_1 + x_2\varepsilon_2 + \cdots + x_n\varepsilon_n$$

$$\hat{y} = y_0 + y_1\varepsilon_1 + y_2\varepsilon_2 + \cdots + y_n\varepsilon_n.$$

and three real numbers α, β and μ we have

$$\alpha\hat{x} + \beta\hat{y} + \mu = (\alpha x_0 + \beta y_0 + \mu) + (\alpha x_1 + \beta y_1)\varepsilon_1 + \cdots + (\alpha x_n + \beta y_n)\varepsilon_n \qquad (3.9)$$

Extending non-affine operations (operations other than addition/subtraction) requires the use of a good approximation and an extra term to bound the error of the chosen approximation.

Suppose we have to compute a non-affine operation of two variables $w = f(x, y)$. Given x and y defined by Eq. 3.5, we want to compute and affine form $\hat{w}$ consistent with $\hat{x}$ and $\hat{y}$ and that preserves the information provided by them as much as possible. First, we write w as a function of the noise symbols in $\hat{x}$ and $\hat{y}$:

$$w = f^{*}(\varepsilon_1, \dots, \varepsilon_n) \tag{3.10}$$

with $f^{*} : \mathbf{U}^n \rightarrow \mathbf{R}$. In general, f^{*} is not an affine function of $\varepsilon_1, \dots, \varepsilon_n$. So, we approximate f^{*} over $\mathbf{U}^n$ by an affine function f^a with error bound δ:

$$|f^{*}(\varepsilon_1, \dots, \varepsilon_n) - f^a(\varepsilon_1, \dots, \varepsilon_n)\,| \leq \delta \text{ for all } \varepsilon_1, \dots, \varepsilon_n \in \mathbf{U}.$$

With $f^a(\varepsilon_1, \dots, \varepsilon_n) = w_0 + w_1\varepsilon_1 + w_2\varepsilon_2 + \cdots + w_n\varepsilon_n$, we obtain finally $w = f(x, y)$ expressed in it affine form:

$$\hat{w} = w_0 + w_1\varepsilon_1 + w_2\varepsilon_2 + \cdots + w_n\varepsilon_n + w_k\varepsilon_k$$

with $w_k = \delta$ and ε_k is a new noise symbol. The real challenge of AA is to find an affine approximation f^a that is easy to compute but which has a small error δ.

It should be noted that the introduction of the term $w_k\varepsilon_k$ to represent the non-affine part of $f^{*}(\varepsilon_1, \dots, \varepsilon_n)$ implies a loss of information. From this point on, the noise symbol ε_k

will be implicitly assumed to be independent of $\varepsilon_1, \dots, \varepsilon_n$, when in fact it is a non-affine function of them.

For simplicity, the formulas above, for both affine and non-affine operations, do not take into account rounding errors. In practice, though, rounding errors are handled by adding a new noise symbol or by absorbing them into the approximation error term $w_k \varepsilon_k$ in the case of non-affine operations. More details are given in [14].

3.1.5 Selection of a Good Affine Approximation

As said above, to compute with Affine Arithmetic, we must find a good affine approximation f^a for each primitive non-affine operation f. When we write f^a as a function of the noise symbols in the input forms $\hat{x}$ and $\hat{y}$,

$$f^a(\varepsilon_1, \dots, \varepsilon_n) = w_0 + w_1\varepsilon_1 + w_2\varepsilon_2 + \cdots + w_n\varepsilon_n,$$

we see that there are n+1 degrees of freedom for the choice of f^a, corresponding to the choices of $w_0, \dots, w_n$. For simplicity we usually consider only approximations f^a that are themselves affine combination of the input forms $\hat{x}$ and $\hat{y}$:

$$f^a = \alpha\hat{x} + \beta\hat{y} + \mu \tag{3.11}$$

This simplification reduces the number of parameters to determine from n+1 to just three. For univariate functions $f(x)$, the restriction is in fact harmless because the best affine approximation f^a is indeed of the form $\alpha\hat{x} + \mu$. In any case, the error term for the restricted approximation is still quadratic on the size of the input ranges.

There are two basics approaches to finding a good affine approximation to a non- affine univariate function: minimize the error or minimize the range.

To minimize the error, we select the affine approximation that has the smallest possible error over the given input interval. This affine approximation is then the best approximation in the Chebyshev (minimax) sense. This approximation is optimal in the sense that it minimize the measure of the polytope defined by the affine forms $\hat{x}$ and $\hat{y}$ and $\widehat{w}$. In other words it preserves the maximum information about $x, y\ and\ w$. However, the best approximation does not necessarily have the smallest range for $\widehat{w}$ alone.

At the end, the choice of which affine approximation to use depends on the application and on the function to approximate.

One important primitive operation that is not directly available in affine basic operations and that needs to be approximated is multiplication. Here we consider division as a multiplication ($x/y = x \times 1/y$).

Given two affine forms

$$\hat{x} = x_0 + x_1\varepsilon_1 + x_2\varepsilon_2 + \cdots + x_n\varepsilon_n$$

$$\hat{y} = y_0 + y_1\varepsilon_1 + y_2\varepsilon_2 + \cdots + y_n\varepsilon_n.$$

their product is

$$\hat{x}.\hat{y} = \left(x_0 + \sum_{i=1}^{n} x_i\varepsilon_i\right).\left(y_0 + \sum_{i=1}^{n} y_i\varepsilon_i\right)$$

$$= x_0y_0 + \sum_{i=1}^{n}(x_0y_i + y_0x_i)\,\varepsilon_i + \sum_{i=1}^{n} x_i\varepsilon_i\;.\sum_{i=1}^{n} y_i\varepsilon_i$$

We can then write the following rule for the affine form of multiplication:

$$\hat{x}.\hat{y} = x_0y_0 + \sum_{i=1}^{n}(x_0y_i + y_0x_i)\,\varepsilon_i + w_k\varepsilon_k\,, \tag{3.12}$$

where

$$|w_k| \geq \left|\sum_{i=1}^{n} x_i\varepsilon_i\;.\sum_{i=1}^{n} y_i\varepsilon_i\right|, \qquad \varepsilon_i \in \mathbf{U}\,,$$

is an upper bound for the approximation error, as before. The simplest bound is

$$w_k = \sum_{i=1}^{n}|x_i|\;.\sum_{i=1}^{n}|y_i|,$$

which is at most four times the error of the best affine approximation, but is very easily computed.

3.1.6 Affine Arithmetic with the Dependency Problem

Let’s return to the examples in Section 3.1.1 to check how Affine Arithmetic works on the dependency problem.

$$f(x) = x - x$$

Using the affine form of x in Eq. 3.5,

$$\hat{x} = x_0 + x_1\varepsilon_1 + x_2\varepsilon_2 + \cdots + x_n\varepsilon_n$$

$$\begin{aligned} f(x) &= x - x \\ &= (x_0 + x_1\varepsilon_1 + x_2\varepsilon_2 + \cdots + x_n\varepsilon_n) - (x_0 + x_1\varepsilon_1 + x_2\varepsilon_2 + \cdots + x_n\varepsilon_n) \\ &= 0\,, \end{aligned}$$

which gives the exact result of $f(x)$. With AA, the substraction formula actually recognizes that in this case the operands are actually the same quantity because they share the same noise symbols with the same coefficients and not just two quantities that happen to have the same range of possible values.

$$f(x) = (20 - x)(20 + x), with\, x\ \in\ [-3, 3]$$

First writing x in the simplest AA form as in Eq. (3.6),

$$\hat{x} = x_0 + x_1\varepsilon_1\ ,\ \ \varepsilon_1\ \ \in \mathbf{U}$$

with $x_0 = (-3 + 3)/2 = 0$ and $x_1 = (-3 - (3))/2 = -3$

$$\hat{x} = 0 - 3\varepsilon_1$$

$$(20 - x) = 20 + 3\varepsilon_1$$

$$(20 + x) = 20 - 3\varepsilon_1$$

$$(20 - x)(20 + x) = 400 - 9\varepsilon_1$$

Using Eqs. (3.7) and (3.8) to transform the affine form into an interval range of values

$$f(x) \in [391,409]$$

So AA gives a diameter of 18 while previously IA gave a diameter of 240.

These simple examples show that AA can easily replace IA even when no attempt was made to exploit the additional information on joint ranges provided by using more noise symbols for the affine form of x.

3.2 Affine Arithmetic in Prognosis Field

We have seen in the previous section that Affine Arithmetic can be a great tool for uncertainty propagation. The addition and subtraction operations are simple to use for quantities in their affine form and there is no need for approximations. Also in their affine forms it is simple to keep track of the dependency between the uncertain parameters, which is one of the main requirements for the prognosis field. However, the necessity to look for affine approximation functions when multiplication or division operations are needed or when complex combinations between the uncertain parameters are required for the computation of uncertainty makes Affine Arithmetic difficult for numerical computations ~~but~~ and also not competitive against uncertainty propagation methods like the Monte Carlo analysis.

In this work an experimentation is done, with a different methodology for Affine Arithmetic, specifically for the prognosis field to not only avoid the need of approximate affine functions in the case of multiplication (division) operations but also to challenge propagation methods like the Monte Carlo analysis.

3.2.1 Affine Arithmetic Applied to Paris Erdogan Law

The Paris Erdogan Law equation for constant amplitude loading is:

$$\frac{da}{dn} = C(\Delta K)^m \tag{3.13}$$

with

$$\Delta K = \bar{Y}(\bar{a})\Delta\sigma\sqrt{\pi a} \text{ and } \bar{a} = \frac{a}{2w} \tag{3.14}$$

The parameters, *C* and *m*, depend on the microstructure of the material, and therefore they can vary depending on the position in the specimen and the specimen samples chosen. *C* and *m* can be seen then as the uncertain parameters in Paris's law. The effects of the variation for these uncertain parameters on the crack length and thus the lifetime of the specimen are the driving force of this section. The parameter $Y(\bar{a})$ depends on the geometry of the structure, and its value for the different assumptions below, can be found in [15].

Replacing Eq. (3.14) into (3.13) gives:

$$\frac{da}{dn} = C\left(Y(\bar{a})\Delta\sigma\sqrt{\pi a}\right)^m \tag{3.15}$$

All the parameters are assumed to be known by their range. Assuming that C and m are independent (no noise symbol shared in their AA expression), we have:

$$a = [a_L, a_U] = a_1 + a_2\varepsilon \tag{3.16}$$

$$C = [C_L, C_U] = C_1 + C_2\varepsilon_1 \tag{3.17}$$

$$m = [m_L, m_U] = m_1 + m_2\varepsilon_2 \tag{3.18}$$

We know that a increases with time. So its noise symbol, ε also increases with time.

Note that from now on, for any variable x that has a dependency relationship with a; if x is increasing when a increases, its noise symbol will be replaced by $+\boldsymbol{\varepsilon}$ and by $-\boldsymbol{\varepsilon}$ otherwise. For any function $f(x)$, the derivative of f with respect with x will be called f_x.

Plugging Eqs. (3.16) to (3.17) into Eq. (3.15):

$$\frac{da}{dn} = (C_1 + C_2\varepsilon_1)\left(Y(\bar{a})\Delta\sigma\sqrt{\pi(a_1 + a_2\varepsilon)}\right)^{(m_1+m_2\varepsilon_2)} \tag{3.19}$$

Let's call

$$A(\varepsilon) = Y(\bar{a})\Delta\sigma\sqrt{\pi(a_1 + a_2\varepsilon)} \tag{3.20}$$

Assumption 1: $Y(\bar{a}) = 1$ (For an infinite plate or if the crack is very small compared to the plate's width)

$$\xrightarrow{yields} \quad A(\varepsilon) = \Delta\sigma\sqrt{\pi(a_1 + a_2\varepsilon)} \tag{3.21}$$

$$\xrightarrow{yields} \quad A_\varepsilon = \frac{0.5\pi a_2 \Delta\sigma}{\sqrt{\pi(a_1 + a_2\varepsilon)}} \geq 0, \text{because } a_2 \geq 0$$

It means that A increases for $A \in [-1,1]$:

$$A_U = A(1)$$

$$= \Delta\sigma\sqrt{\pi(a_1 + a_2)}$$

$$\boldsymbol{A_U = \Delta\sigma\sqrt{\pi a_U}\mathbf{Y}(a_U)} \tag{3.22}$$

and

$$A_L = A(-1)$$

$$= \Delta\sigma\sqrt{\pi(a_1 - a_2)}$$

$$\boldsymbol{A_L = \Delta\sigma\sqrt{\pi a_L}\mathbf{Y}(a_L)} \tag{3.23}$$

and we can then write A into its affine form :

$$A(\varepsilon) = A_1 + A_2\varepsilon$$

$$with\ A_1 = \frac{A_U + A_L}{2}\ and\ A_2 = \frac{A_U - A_L}{2}$$

- **Assumption 2:** $\bar{Y}(\bar{a}) = 1 + 0.256\bar{a} + 1.152\bar{a}^2 + 12.20\bar{a}^3$

In this case

$$A(\varepsilon) = \Delta\sigma\sqrt{\pi(a_1 + a_2\varepsilon)}\left[1 + 0.128\left(\frac{a_1 + a_2\varepsilon}{w}\right) + 0.288\left(\frac{a_1 + a_2\varepsilon}{w}\right)^2 + 1.525\left(\frac{a_1 + a_2\varepsilon}{w}\right)^3\right] \tag{3.24}$$

It can be shown that A monotonically increases for ε = [-1,1] and thus :

$$A_U = \Delta\sigma\sqrt{\pi(a_1+a_2)}\left(1+0.128\left(\frac{a_1+a_2}{w}\right)+0.288\left(\frac{a_1+a_2}{w}\right)^2+1.525\left(\frac{a_1+a_2}{w}\right)^3\right)$$

$$= \Delta\sigma\sqrt{\pi a_U}\left(1+0.128\left(\frac{a_U}{w}\right)+0.288\left(\frac{a_U}{w}\right)^2+1.525\left(\frac{a_U}{w}\right)^3\right)$$

$$\boldsymbol{A_U = \Delta\sigma\sqrt{\pi a_U}}\mathbf{Y}(\boldsymbol{a_U}) \tag{3.25}$$

and

$$A_L = \Delta\sigma\sqrt{\pi(a_1-a_2)}\left(1+0.128\left(\frac{a_1-a_2}{w}\right)+0.288\left(\frac{a_1-a_2}{w}\right)^2+1.525\left(\frac{a_1-a_2}{w}\right)^3\right)$$

$$= \Delta\sigma\sqrt{\pi a_L}\left(1+0.128\left(\frac{a_L}{w}\right)+0.288\left(\frac{a_L}{w}\right)^2+1.525\left(\frac{a_L}{w}\right)^3\right)$$

$$\boldsymbol{A_L = \Delta\sigma\sqrt{\pi a_L}}\mathbf{Y}(\boldsymbol{a_L}) \tag{3.26}$$

Then we can write: $A(\varepsilon) = A_1 + A_2\varepsilon$

With $A_1 = \frac{A_U+A_L}{2}$ and $A_2 = \frac{A_U-A_L}{2}$

Assumption 3: $Y(\bar{a}) = \sqrt{\sec(\pi\bar{a})} = \sqrt{\sec\left(\pi\frac{a}{2w}\right)}$ (For a center-cracked tension specimen)

In this case:

$$A(\varepsilon) = \Delta\sigma\sqrt{\pi(a_1+a_2\varepsilon)}\sqrt{\sec\left(\pi\frac{a_1+a_2\varepsilon}{2w}\right)} \tag{3.27}$$

It can be shown that A monotonically increases for ε =[-1,1]

$$A_U = A(1)$$

$$= \Delta\sigma\sqrt{\pi(a_1 + a_2)}\sqrt{\sec\left(\pi\frac{a_1 + a_2}{2w}\right)}$$

$$= \Delta\sigma\sqrt{\pi a_U}\sqrt{\sec\left(\pi\frac{\boldsymbol{a_U}}{2w}\right)}$$

$$\boldsymbol{A_U} = \Delta\boldsymbol{\sigma}\sqrt{\boldsymbol{\pi a_U}}\mathbf{Y}(\boldsymbol{a_U}) \tag{3.28}$$

and

$$A_L = A(-1)$$

$$= \Delta\sigma\sqrt{\pi(a_1 - a_2)}\sqrt{\sec\left(\pi\frac{a_1 - a_2}{2w}\right)}$$

$$= \Delta\sigma\sqrt{\pi a_L}\sqrt{\sec\left(\pi\frac{\boldsymbol{a_L}}{2w}\right)}$$

$$\boldsymbol{A_L} = \Delta\boldsymbol{\sigma}\sqrt{\boldsymbol{\pi a_L}}\mathbf{Y}(\boldsymbol{a_L}) \tag{3.29}$$

Then we can write: $(\varepsilon) = A_1 + A_2\varepsilon$,

with $A_1 = \frac{A_U+A_L}{2}$ and $A_2 = \frac{A_U-A_L}{2}$

Assumption 4: $Y(\bar{a}) = \frac{1}{\sqrt{1-(2\bar{a})^2}} = \frac{1}{\sqrt{1-\left(\frac{a}{w}\right)^2}}$

In this case:

$$A(\varepsilon) = \Delta\sigma\frac{\sqrt{\pi(a_1+a_2\varepsilon)}}{\sqrt{1-\left(\frac{a_1+a_2\varepsilon}{w}\right)^2}} \tag{3.30}$$

It can be shown that A monotonically increases for ε = [-1,1]

$$A_U = A(1)$$

$$= \Delta\sigma \frac{\sqrt{\pi(a_1 + a_2)}}{\sqrt{1 - \left(\frac{a_1 + a_2}{w}\right)^2}}$$

$$= \Delta\sigma\sqrt{\pi a_U}\frac{1}{\sqrt{1 - \left(\frac{a_U}{w}\right)^2}}$$

$$\boldsymbol{A_U = \Delta\sigma\sqrt{\pi a_U}\mathrm{Y}(a_U)} \tag{3.31}$$

and

$$A_L = A(-1)$$

$$= \Delta\sigma \frac{\sqrt{\pi(a_1 - a_2)}}{\sqrt{1 - \left(\frac{a_1 - a_2}{w}\right)^2}}$$

$$= \Delta\sigma\sqrt{\pi a_L}\frac{1}{\sqrt{1 - \left(\frac{a_L}{w}\right)^2}}$$

$$\boldsymbol{A_L = \Delta\sigma\sqrt{\pi a_L}\mathrm{Y}(a_L)} \tag{3.32}$$

Then then we can write: $A(\varepsilon) = A_1 + A_2\varepsilon$

with $A_1 = \frac{A_U + A_L}{2}$ and $A_2 = \frac{A_U - A_L}{2}$

We can conclude that for any assumption, A can be written as:

$$A(\varepsilon) = A_1 + A_2\varepsilon$$

with $A_1 = \frac{A_U + A_L}{2}$ and $A_2 = \frac{A_U - A_L}{2}$ and

$$\boldsymbol{A_U} = \Delta\boldsymbol{\sigma}\sqrt{\boldsymbol{\pi a_U}}\mathbf{Y}(\boldsymbol{a_U}) \tag{3.33}$$

$$\boldsymbol{A_L} = \Delta\boldsymbol{\sigma}\sqrt{\boldsymbol{\pi a_L}}\mathbf{Y}(\boldsymbol{a_L}) \tag{3.34}$$

Rewriting Eq. (3.19) gives:

$$\frac{da}{dn} = (C_1 + C_2\varepsilon_1)(A_1 + A_2\varepsilon)^{(m_1 + m_2\varepsilon_2)} \tag{3.35}$$

Using

$$f(\varepsilon, \varepsilon_2) = (A_1 + A_2\varepsilon)^{(m_1 + m_2\varepsilon_2)} \tag{3.36}$$

let's find the maximum and minimum value of f.

$$f_{\varepsilon_2} = m_2 \ln(A_1 + A_2\varepsilon_3)\, f(\varepsilon, \varepsilon_2)$$

$$f_\varepsilon = (m_1 + m_2\varepsilon_2)\frac{A_2}{A_1 + A_2\varepsilon} f(\varepsilon, \varepsilon_2)$$

$m_2 \geq 0,\ A = A_1 + A_2\varepsilon \geq 1$ and $f(\varepsilon, \varepsilon_2) > 0$ which yields $f_{\varepsilon_2} \geq 0$

$m_1 + m_2\varepsilon_2 \geq 0, A_2 \geq 0$ and $f(\varepsilon, \varepsilon_2) > 0$ which yields $f_\varepsilon \geq 0$

f is then increasing with respect to ε and with respect to ε_2

$$f_U = f(1,1)$$

$$= (A_1 + A_2)^{(m_1+m_2)}$$

$$\boldsymbol{f_U = A_U{}^{m_U}} \tag{3.37}$$

and

$$f_L = f(-1,1)$$

$$= (A_1 - A_2)^{(m_1-m_2)}$$

$$\boldsymbol{f_L = A_L{}^{m_L}} \tag{3.38}$$

Then we can write: $f(\varepsilon) = f_1 + f_2\varepsilon$

with $f_1 = \frac{f_U+f_L}{2}$ and $f_2 = \frac{f_U-f_L}{2}$

Then,

$$\frac{da}{dn} = (C_1 + C_2\varepsilon_1)(f_1 + f_2\varepsilon\ ) \tag{3.39}$$

$$\xrightarrow{yields} \qquad (a)_n = (C_1 + C_2\varepsilon_1)(f_1 + f_2\varepsilon\ )dn + (a)_{n-1}$$

$$\xrightarrow{yields} (a_1 + a_2\varepsilon_3\ )_n = (C_1 + C_2\varepsilon_1)(f_1 + f_2\varepsilon\ )dn + (a_1 + a_2\varepsilon\ )_{n-1} \tag{3.40}$$

Let’s call

$$g(\varepsilon, \varepsilon_1) = (C_1 + C_2\varepsilon_1)(f_1 + f_2\varepsilon\ )dn + (a_1 + a_2\varepsilon\ )_{n-1} \tag{3.41}$$

Let's find the maximum and minimum values of $(\varepsilon, \varepsilon_1)$:

$$g_{\varepsilon_1} = C_2(f_1 + f_2\varepsilon\ )dn$$

$$g_{\varepsilon} = f_2(C_1 + C_2\varepsilon_1)dn + (a_2\ )_{n-1}$$

$C_2 \geq 0$, $dn > 0$ and $(f_1 + f_2\varepsilon\ ) > 0$ which yields $g_{\varepsilon_1} \geq 0$

$f_2 \geq 0$,$(a_2\ )_{n-1} \geq 0,$ $dn > 0$ and $(C_1 + C_2\varepsilon_1) > 0$ which yields $g_{\varepsilon} \geq 0$

g is then increasing monotonically with respect to ε and with respect to ε_1

$$\begin{aligned} g_U &= g(1,1) \\ &= (C_1 + C_2)(f_1 + f_2\ )dn + (a_1 + a_2\ )_{n-1} \end{aligned}$$

$$\boldsymbol{g_U = C_U f_U dn + (a_U\ )_{n-1}} \tag{3.42}$$

and

$$\begin{aligned} g_L &= g(-1,-1) \\ &= (C_1 - C_2)(f_1 - f_2\ )dn + (a_1 - a_2\ )_{n-1} \end{aligned}$$

$$\boldsymbol{g_L = C_L f_L dn + (a_L\ )_{n-1}} \tag{3.43}$$

Then we can write: $(\varepsilon) = g_1 + g_2\varepsilon$, with $g_1 = \frac{g_U + g_L}{2}$ and $g_2 = \frac{g_U - g_L}{2}$

Since $(a_1 + a_2\varepsilon_3\ )_n = g(\varepsilon, \varepsilon_1)$, we have then:

$$\boldsymbol{(a_U)_n = C_U f_U dn + (a_U\ )_{n-1}} \tag{3.44}$$

$$\boldsymbol{(a_L)_n = C_L f_L dn + (a_L\ )_{n-1}} \tag{3.45}$$

Using Eqs. (3.33), (3.34), (3.37) and (3.38) into Eqs. (3.44) and (3.45) we then obtain two iterative formula for the range of $(a)_n$ as accurate as the real solution of the PE equation:

$$(\boldsymbol{a_U})_{\boldsymbol{n}} = \boldsymbol{C_U}\left[\Delta\boldsymbol{\sigma}\sqrt{\boldsymbol{\pi a_U}}\mathbf{Y}(\boldsymbol{a_U})\right]^{\boldsymbol{m_U}}\boldsymbol{dn} + (\boldsymbol{a_U}\,)_{\boldsymbol{n-1}} \tag{3.46}$$

$$(\boldsymbol{a_L})_{\boldsymbol{n}} = \boldsymbol{C_L}\left[\Delta\boldsymbol{\sigma}\sqrt{\boldsymbol{\pi a_L}}\mathbf{Y}(\boldsymbol{a_L})\right]^{\boldsymbol{m_L}}\boldsymbol{dn} + (\boldsymbol{a_L}\,)_{\boldsymbol{n-1}} \tag{3.47}$$

Since $(a)_n$ increases at each cycle, it increases then also with ε:

$$(\boldsymbol{a_1})_{\boldsymbol{n}} = \frac{\boldsymbol{C_U}\left[\Delta\boldsymbol{\sigma}\sqrt{\boldsymbol{\pi a_U}}\mathbf{Y}(\boldsymbol{a_U})\right]^{\boldsymbol{m_U}} + \boldsymbol{C_L}[\Delta\boldsymbol{\sigma}\sqrt{\boldsymbol{\pi a_L}}\mathbf{Y}(\boldsymbol{a_L})]^{\boldsymbol{m_L}}}{\mathbf{2}}\boldsymbol{dn} + (\boldsymbol{a_1})_{\boldsymbol{n-1}} \tag{3.48}$$

$$(\boldsymbol{a_2})_{\boldsymbol{n}} = \frac{\boldsymbol{C_U}\left[\Delta\boldsymbol{\sigma}\sqrt{\boldsymbol{\pi a_U}}\mathbf{Y}(\boldsymbol{a_U})\right]^{\boldsymbol{m_U}} - \boldsymbol{C_L}[\Delta\boldsymbol{\sigma}\sqrt{\boldsymbol{\pi a_L}}\mathbf{Y}(\boldsymbol{a_L})]^{\boldsymbol{m_L}}}{\mathbf{2}}\boldsymbol{dn} + (\boldsymbol{a_2})_{\boldsymbol{n-1}} \tag{3.49}$$

$$(a_1 + a_2\varepsilon_3\,)_n = (\boldsymbol{a_1})_{\boldsymbol{n}} + (\boldsymbol{a_2})_{\boldsymbol{n}}\varepsilon \tag{3.50}$$

The primary goal of using Affine Arithmetic is to be able to build some functions which could directly compute the lifetime of a specimen, given only the interval range of the parameters. To do so, all of the uncertain parameters of the crack growth equation were first written in their affine form. A study was done on the crack growth equation using different noise symbols in their affine forms to obtain the critical points of the crack growth law. Finally, two analytical equations [Eqs. (3.46) and (3.47)] for the maximum and the minimum values of the crack half-length at any loading cycle were obtained.

3.2.2 Prediction of Crack Growth Under Cyclic Loading in Isotropic Plates Using Affine Arithmetic on the Paris Erdogan Law

The isotropic plate structure investigated in this section is made of Titanium alloy Ti-6Al-4V and has a finite rectangular shape with a $2w$ width. A Mode I opening crack is centrally situated, and it is perpendicular to a uniform tensile loading axis. The tensile stress is denoted as σ and the crack length is given as $2a$. The Paris Erdogan law is used to quantify crack growth in terms of the number of loading cycles of a specimen given a particular crack size.

The parameters *C* and *m* are uncertain parameters in Paris's Law. The effects of their variation on the crack length, and thus the lifetime of the specimen, are the driving force of this section. $Y(\bar{a}) = 1$ in our analysis, which corresponds to the assumption of a center crack in an infinite plate. The Paris Erdogan Law is computed from the initial crack half-length a_0 of the specimen at zero cycle to a critical crack half-length a_{cr}, at the lifetime of the specimen. In our case, a_{cr} is chosen to be the crack half-length corresponding to when the crack-tip stress intensity factor reaches the fracture toughness of the material K_{I_c}(The subscript *I* denotes Mode I of crack opening).

The Paris Erdogan Law is integrated through the lifetime using a forward recursive Euler Method to give the following equation for the crack half-length at any cycle *N*:

$$(a)_{n+1} = C\left[\Delta\sigma\sqrt{\pi(a\,)_n}\mathrm{Y}((a\,)_n)\right]^m dn + (a\,)_n \tag{3.51}$$

3.2.2.1 Procedure

The parameters, C and m, are defined as interval/range and the lifetime N_f of the specimen is computed therefore as a range. It is important to understand that the upper/lower limits of the lifetime range corresponds to the best/worst combination of the uncertain parameters, respectively. The lower limit of the lifetime range is the minimum number of cycles before the critical crack length is reached while the upper limit is the maximum number of cycles the specimen can sustain before the crack grows to its critical length. At first, two Monte Carlos simulations with different number of samples are run from a_0 to a_{cr} using Eq. (3.51) to determine the specimen lifetime. Eqs. (3.46) and (3.47) are then used to predict the lifetime of the specimen using Affine Arithmetic. Finally, the lifetime range and the computation time for the Monte Carlo simulations as well as the one for the Affine Arithmetic method are compared.

3.2.2.2 Monte Carlo Analysis for Paris Erdogan Law

The Paris Erdogan's parameters and the specimen material properties are taken from [16]. The parameters are defined by an interval with $logC \in [-15.0 \ \ -11.6]$ and $m \in [3.7 \ \ 6.2]$. The fracture thoughness of the material is 75 MPa$\sqrt{m}$ with a load ratio R of 0.8. The Monte Carlo analysis is performed by sampling the parameters C and m with a uniform distribution over their interval. All the parameters are assumed to be independent and known by their ranges. Monte Carlo 1 and Monte Carlo 2 simulations with 1000 samples and 3000 samples of the uncertain parameters' values, respectively, are carried out. As mentioned above for each of the different Monte Carlo simulation cases, only the crack growth curves depicting the lifetime of the specimen in the worst case and in the best case of combination between the uncertain parameter values are useful here because they correspond to the minimum and the maximum values of the crack length, respectively. Table 3.1 summarizes the different lifetimes computed for each of the Monte Carlo simulations and their computation time.

3.2.2.3 Affine Arithmetic for Paris Erdogan Law

The primary goal of using Affine Arithmetic is to be able to build some functions which can directly compute the lifetime of a specimen, given only the interval range of the parameters. To do so, all the uncertain parameters of the crack growth law are first written in their affine form. A function study is done on the crack growth law that is a function of the different noise symbols in their affine forms to obtain the critical points of the crack growth law. Finally two analytical equations [Eqs. (3.46) and (3.47)] for the maximum and the minimum values of the crack half-length at any loading cycle are obtained.

The values of the upper limit $(\boldsymbol{a_U})_{\boldsymbol{n+1}}$ and the lower limit $(\boldsymbol{a_L})_{\boldsymbol{n+1}}$ of the crack half-length are then computed respectively from $(\boldsymbol{a_U})_{\boldsymbol{0}} = \boldsymbol{a_0}$ to $(\boldsymbol{a_U})_{\boldsymbol{n+1}} = \boldsymbol{a_{cr}}$ and from $(\boldsymbol{a_L})_{\boldsymbol{0}} = \boldsymbol{a_0}$ to $(\boldsymbol{a_L})_{\boldsymbol{n+1}} = \boldsymbol{a_{cr}}$. The value of the cycle step sizes *dn* is chosen here as a function so that it is small enough to have a smooth variation of $(\boldsymbol{a_U})_{\boldsymbol{n+1}}$ and $(\boldsymbol{a_L})_{\boldsymbol{n+1}}$. Figures 2.1 and 2.2 show the curves of Eqs. (3.46) and Eq. (3.47) plotted against the curves obtained from the two Monte Carlo simulations computed with Eq. (3.51). The curves in red color represent the plot of the upper value of the crack half-length range, whereas the curves in blue represent the plot of the lower values of the crack half-length range respectively for AA and for Monte Carlo simulations (triangle marker type).

We can see in Figure 3.3 that the first Monte Carlo simulation with 1000 samples predicts a faillure range of smaller diameter than the one of the prediction of Affine Arithmetic.

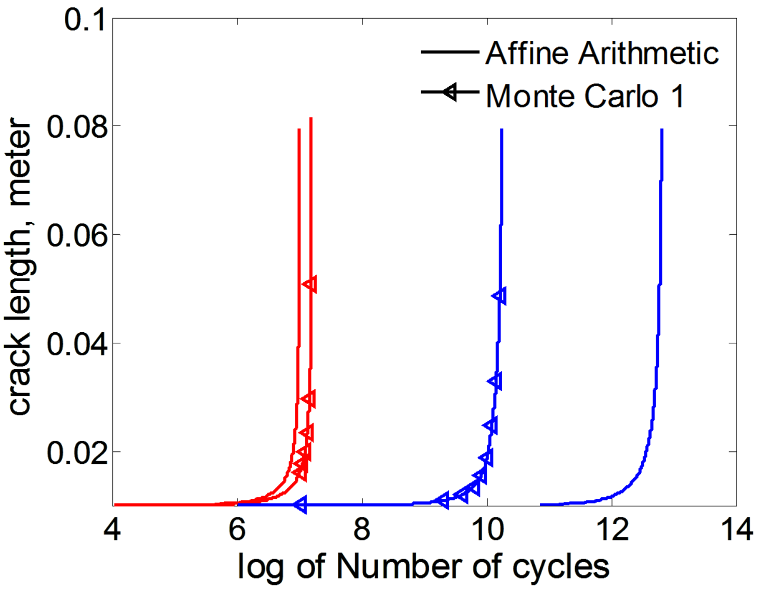

Figure 3.3. Comparison of Crack Growth Curves Between Monte Carlo 1 (1000 samples) and Affine Arithmetic.

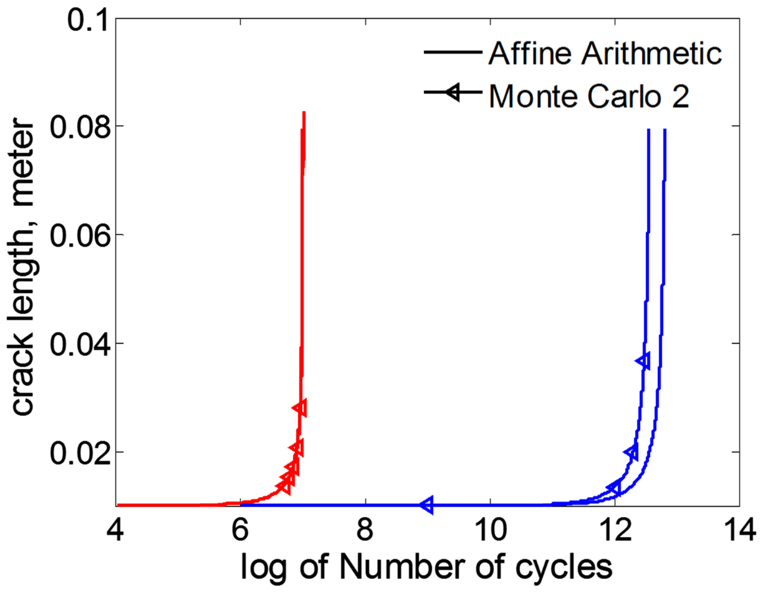

Figure 3.4. Comparison of Crack Growth Curves Between Monte Carlo 2 (3000 samples) and Affine Arithmetic.

It might seem that the AA prediction range is actually not accurate enough or too far off. However with an increased number of samples, Figure 3.4 shows that the Monte Carlo prediction range starts getting closer to the one of AA and the prediction curves of AA and Monte Carlo 2 are overlapped.

Table3.1 Comparison of Lifetime Prediction and Computation Times Between Affine Arithmetic and Two Monte Carlo Simulations for Fatigue Crack

Uncertainty propagation method	Affine Arithmetic	Monte Carlo 1	Monte Carlo 2
Number of samples	-	1000	3000
Computation time (sec)	2.22	62	3265
log (n)	[6.99, 12.80]	[7.18, 10.24]	[6.99, 12.56]
Number of days for 20 Hz load frequency	[5.62, 3677530]	[8.8, 10107]	[5.75, 2086682]

Table 3.1 shows the lifetime prediction yielded by each of the simulations and their computation times. We can see that the Monte Carlo 1 simulation predicts the possibility of occurrence of failure three days after the failure is predicted to happen by Affine Arithmetic. Simply increasing the number of samples to 3000 helps the Monte Carlo simulation ~~to~~ make predictions closer to AA but requires a longer computation time. It took almost an hour to run the second Monte Carlo simulation whereas Affine Arithmetic took only 2 seconds to give its prediction with that accuracy level.

Chapter 4

Kardomateas Law for Composite Materials Under Cyclic Compressive Loading

In [17], Kardomateas described a new law, that takes into account ~~the~~ both Modes I and II fracture toughness in the description of the delamination tip in a composite material under compressive loading. The major characteristic of delamination growth is the fact that the fracture path is constrained irrespective of the application of the globally-applied loads, hence growth is inherently mixed mode. Considering a plate of half-length *L* with a unit width, with a through-the-width delamination of half-length *l*, symmetrically located at an arbitrary position through the thickness *T* (Figure 4.1)

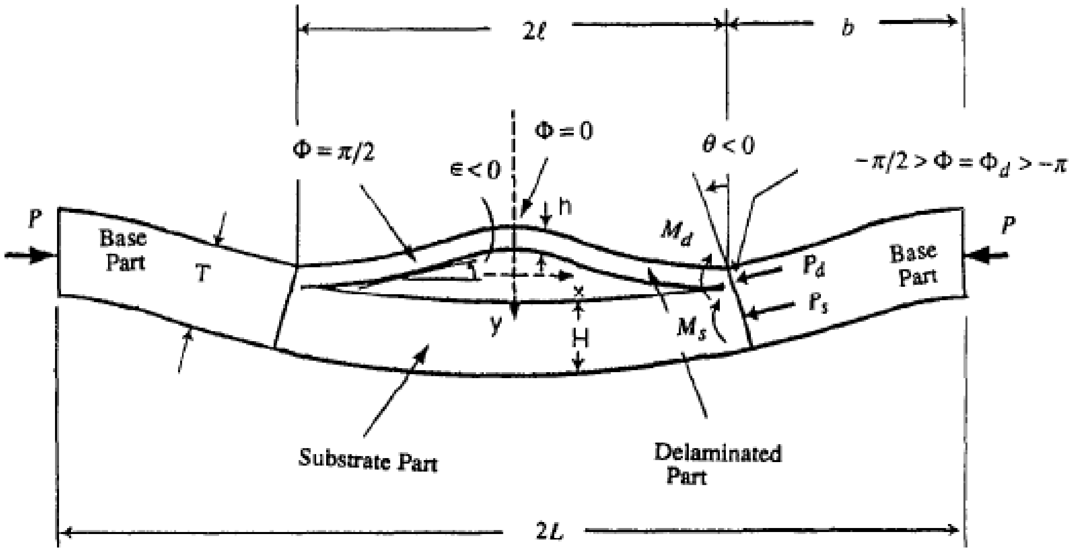

Figure 4.1. A One-Dimensional Delamination Configuration Under Compression [17].

For a cyclic loading that causes a variation of the strain energy release rate from G_{min} to G_{max}, the stresses near the tip of the delamination are totally described by G_{max}, the load ratio $\alpha = \frac{G_{min}}{G_{max}}$, which expresses the ratio of minimum to maximum loading, and the mixity parameter, $\Psi = \tan^{-1}(\frac{K_{II}}{K_I})$ that expresses the relative amounts of Mode I (opening) and Mode II (shearing) components. The pure Mode I corresponds to $\Psi = 0$ and the pure Mode II to $\Psi = \pm\frac{\pi}{2}$.

Kardomateas, based on experimental and mechanical observations, assumes that the toughness Γ_0 depends on the Mode mixity:

$$\Gamma_0(\Psi) = \mathrm{G}_{\mathrm{I}}^{\mathrm{c}}\left[1 + \left(\frac{\mathrm{G}_{\mathrm{I}}^{\mathrm{c}}}{\mathrm{G}_{\mathrm{II}}^{\mathrm{c}}} - 1\right)\sin^2\Psi\right]^{-1} \tag{4.1}$$

The effects of mode-dependent toughness on the delamination growth is accounted for by defining:

$$\tilde{G} = \frac{G}{\Gamma_0(\Psi)} \tag{4.2}$$

$\tilde{G}$ is regarded as a mode-adjusted crack driving force in the sense that the criterion for crack advance is $G/\Gamma_0 = 1$. In other words for a crack to growth, the value of $\tilde{G}$ should reach 1.

For slow growth of the delamination, Kardomateas defines the following law:

$$\frac{dl}{dN} = \frac{C(\Psi)(\Delta\tilde{G})^{m(\Psi)}}{1 - \tilde{G}_{max}} \tag{4.3}$$

$\Delta\tilde{G}$ is the range in the energy release rate, $\Delta\tilde{G} = \tilde{G}_{max} - \tilde{G}_{min}$.

The Mode dependence of the constants *C* and *m* is also defined. Of these two parameters the most important is *m* because of its impact on Eq. (4.3).

$$m(\Psi) = m_I(1 - \sin^2\Psi) + m_{II}\sin^2\Psi \tag{4.4}$$

$$C(\Psi) = C_I(1 - \sin^2\Psi) + C_{II}\sin^2\Psi \tag{4.5}$$

Since the uncertain parameters $\mathrm{G}_{\mathrm{I}}^{\mathrm{c}}$, $\mathrm{G}_{\mathrm{II}}^{\mathrm{c}}$, m_I, m_{II}, C_I and C_{II} are determined by experiments, let's consider as in the case of the Paris Erdogan Law in the previous section that $\mathrm{G}_{\mathrm{I}}^{\mathrm{c}}$, $\mathrm{G}_{\mathrm{II}}^{\mathrm{c}}$, m_I, m_{II}, C_I, C_{II} and *l* are defined by their interval:

$$l = [l_L, l_U] = l_1 + l_2\varepsilon \tag{4.6}$$

$$C_I = [C_{I_L}, C_{I_U}] = C_{I_1} + C_{I_2}\varepsilon_1 \tag{4.7}$$

$$m_I = [m_{I_L}, m_{I_U}] = m_{I_1} + m_{I_2}\varepsilon_2 \tag{4.8}$$

$$\mathrm{G}_{\mathrm{I}}^{\mathrm{c}} = [\mathrm{G}_{\mathrm{I}_L}^{\mathrm{c}}, \mathrm{G}_{\mathrm{I}_U}^{\mathrm{c}}] = \mathrm{G}_{\mathrm{I}_1}^{\mathrm{c}} + \mathrm{G}_{\mathrm{I}_2}^{\mathrm{c}}\varepsilon_6 \tag{4.9}$$

$$C_{II} = [C_{II_L}, C_{II_U}] = C_{II_1} + C_{II_2}\varepsilon_5 \tag{4.10}$$

$$m_{II} = [m_{II_L}, m_{II_U}] = \mathrm{m}_{II_1} + m_{II_2}\varepsilon_4 \tag{4.11}$$

$$\mathrm{G}_{\mathrm{II}}^{\mathrm{c}} = [\mathrm{G}_{\mathrm{II}_L}^{\mathrm{c}}, \mathrm{G}_{\mathrm{II}_U}^{\mathrm{c}}] = \mathrm{G}_{\mathrm{II}_1}^{\mathrm{c}} + \mathrm{G}_{\mathrm{II}_2}^{\mathrm{c}}\varepsilon_3 \tag{4.12}$$

The energy release rate is:

$$G(\varepsilon_0, l) = 0.5Eh(1-\nu^2)(\varepsilon_0 - \varepsilon_{cr})(\varepsilon_0 + 3\varepsilon_{cr}) \tag{4.13}$$

$$\varepsilon_{\boldsymbol{cr}}(\boldsymbol{l}) = \frac{\boldsymbol{\pi^2 h^2}}{\boldsymbol{3(1-\nu^2)l^2}} \tag{4.14}$$

$$\xrightarrow{\boldsymbol{yields}} \quad \varepsilon_{\boldsymbol{cr}}(\varepsilon) = \frac{\boldsymbol{\pi^2 h^2}}{\boldsymbol{3(1-\nu^2)}}(\boldsymbol{l_1} + \varepsilon\boldsymbol{l_2})^{\boldsymbol{-2}}$$

$$\xrightarrow{\boldsymbol{yields}} \quad \varepsilon_{\boldsymbol{cr}}(\varepsilon) = \boldsymbol{H}(\boldsymbol{l_1} + \varepsilon\boldsymbol{l_2})^{\boldsymbol{-2}} \tag{4.15}$$

with $H = \frac{\pi^2 h^2}{3(1-\nu^2)}$

Inserting Eq. (4.6) in Eq. (4.13) we have:

$$G(\varepsilon) = V[\varepsilon_0 - H(l_1 + \varepsilon l_2)^{-2}][\varepsilon_0 + 3H(l_1 + \varepsilon l_2)^{-2}] \tag{4.16}$$

with $V = 0.5Eh(1-\nu^2)$

$$\xrightarrow{yields} \quad G_{\varepsilon} = 4VHl_2(l_1 + \varepsilon l_2)^{-3}\left[-\varepsilon_0 + 3H(l_1 + \varepsilon l_2)^{-2}\right] \tag{4.17}$$

$$G_{\varepsilon} = 0 \quad \xrightarrow{yields} \quad \mathrm{l_{tr}} = \mathrm{l}_{\mathrm{tr}_{\mathbf{1}}} + \varepsilon_{tr}\mathrm{l}_{\mathrm{tr}_{\mathbf{2}}} = \sqrt{\frac{3H}{\varepsilon_0}} \tag{4.18}$$

$$\xrightarrow{yields} \quad \varepsilon_{tr} = \frac{\sqrt{\frac{3H}{\varepsilon_0}} - l_1}{l_2} \tag{4.19}$$

l_{tr} is the unstable - to - stable transition point (crack length) and it is the point where the energy rate G reaches its maximum value ($G_{\varepsilon} = 0$). In the case where the initial delamination length is below l_{tr} $(-1 \leq \varepsilon_{tr} \leq 1)$, then unstable but “contained growth” will occur. For this reason to have stable growth, the initial length should always be chosen so that:

$$l_0 > \mathrm{l_{tr}} \xrightarrow{yields} -1 > \mathcal{E}_{tr} \ or \ \mathcal{E}_{tr} > 1$$

$$l \geq l_0 > \mathrm{l_{tr}} \xrightarrow{yields} l > \mathrm{l_{tr}}$$

$$\xrightarrow{yields} l_1 + \mathcal{E} l_2 > \sqrt{\frac{3H}{\mathcal{E}_0}}$$

$$\xrightarrow{yields} (l_1 + \mathcal{E} l_2)^2 > \frac{3H}{\mathcal{E}_0}$$

$$\xrightarrow{yields} \mathcal{E}_0 > 3H(l_1 + \mathcal{E} l_2)^{-2}$$

$$\xrightarrow{yields} -\mathcal{E}_0 + 3H(l_1 + \mathcal{E} l_2)^{-2} < 0 \qquad (4.20)$$

Using Eq. (4.20) results:

$$G_{\mathcal{E}} = 4VHl_2(l_1 + \mathcal{E} l_2)^{-3}[-\mathcal{E}_0 + 3H(l_1 + \mathcal{E} l_2)^{-2}] < 0 \qquad (4.21)$$

since all the other terms in Eq. (4.17) are positive.

The Mode mixity is also defined by:

$$\tan \Psi = \frac{4\cos w + \sqrt{3}\xi \sin w}{-4\sin w + \sqrt{3}\xi \cos w} \qquad (4.22)$$

where

$$\xi = \left[\frac{4}{3}\left(\frac{\mathcal{E}_0}{\mathcal{E}_{cr}} - 1\right)\right]^{0.5} \tag{4.23}$$

Replacing Eq. (4.15) into Eq. (4.23):

$$\xi(\mathcal{E}) = \left[\frac{4}{3}(\mathcal{E}_0(l_1 + \mathcal{E}l_2)^2 H^{-1} - 1)\right]^{0.5}$$

$$\xrightarrow{yields} \xi_{\mathcal{E}} = \frac{4}{3}\mathcal{E}_0 H^{-1} l_2 (l_1 + \mathcal{E}l_2)\left[\frac{4}{3}(\mathcal{E}_0(l_1 + \mathcal{E}l_2)^2 H^{-1} - 1)\right]^{-0.5} \tag{4.24}$$

ξ is a square root function ($\xi > 0$) and all the other terms in the left side of Eq. (4.24) are positive, which yields $\xi_{\mathcal{E}} \geq 0$. Thus $\xi(\mathcal{E})$ monotonically increases for $\mathcal{E} = [-1,1]$ and:

$$\begin{aligned} \xi_U &= \xi(1) \\ &= \left[\frac{4}{3}(\mathcal{E}_0(l_1 + l_2)^2 H^{-1} - 1)\right]^{0.5} \end{aligned}$$

$$\boldsymbol{\xi_U} = \left[\frac{\mathbf{4}}{\mathbf{3}}\left(\mathcal{E}_{\mathbf{0}} \boldsymbol{l_U}^{\mathbf{2}} \boldsymbol{H}^{\mathbf{-1}} - \mathbf{1}\right)\right]^{\mathbf{0.5}} \tag{4.25}$$

and

$$\begin{aligned} \xi_L &= \xi(-1) \\ &= \left[\frac{4}{3}(\mathcal{E}_0(l_1 - l_2)^2 H^{-1} - 1)\right]^{0.5} \end{aligned}$$

$$\boldsymbol{\xi_L} = \left[\frac{\mathbf{4}}{\mathbf{3}}\left(\mathcal{E}_{\mathbf{0}} \boldsymbol{l_L}^{\mathbf{2}} \boldsymbol{H}^{\mathbf{-1}} - \mathbf{1}\right)\right]^{\mathbf{0.5}} \tag{4.26}$$

Then we can write: $\xi = \xi_1 + \mathcal{E}\xi_2$ and $\xi_1 = \frac{\xi_U+\xi_L}{2}$ and $\xi_2 = \frac{\xi_U-\xi_L}{2}$

Eq. (4.22) becomes:

$$\tan\Psi = \frac{4\cos w + \sqrt{3}(\xi_1 + \mathcal{E}\xi_2)\sin w}{-4\sin w + \sqrt{3}(\xi_1 + \mathcal{E}\xi_2)\cos w} \tag{4.27}$$

$$\xrightarrow{yields} \quad \Psi(\mathcal{E}) = \tan^{-1}\left[\frac{4\,cos\,w + \sqrt{3}(\xi_1 + \mathcal{E}\xi_2)\,sin\,w}{-4\,sin\,w + \sqrt{3}(\xi_1 + \mathcal{E}\xi_2)\,cos\,w}\right] \tag{4.28}$$

we know that Ψ exists and is real if only if :

$$-4\sin w + \sqrt{3}(\xi_1 + \mathcal{E}\xi_2)\cos w \neq 0$$

$$\xrightarrow{yields} \quad \xi_1 + \mathcal{E}\xi_2 \neq \frac{4\sin w}{\sqrt{3}\cos w}$$

$$\xrightarrow{yields} \quad \mathcal{E} \neq \frac{\frac{4}{\sqrt{3}}\tan(w) - \xi_1}{\xi_2}$$

By calling $\mathcal{E}_\Psi = \frac{\frac{4}{\sqrt{3}}\tan(w)-\xi_1}{\xi_2}$, we see that the domain of Ψ is:

$D = [-1, \mathcal{E}_\Psi[\ \text{U}\ ]\mathcal{E}_\Psi, 1]$

A function analysis of Ψ follows:

For $\mathcal{E} \epsilon [-1, \mathcal{E}_\Psi[$,

$$\mathcal{E} \leq \frac{\frac{4}{\sqrt{3}}\tan(w) - \xi_1}{\xi_2} \qquad \xrightarrow{yields} \qquad -4\sin w + \sqrt{3}(\xi_1 + \mathcal{E}\xi_2)\cos w \leq 0$$

We know that the term $4\cos w + \sqrt{3}(\xi_1 + \mathcal{E}\xi_2)\sin w > 0$ in Eq. (4.23) is always positive:

$$\xrightarrow{yields} \quad \tan\Psi < 0$$

$$\xrightarrow{yields} \quad \Psi \epsilon \ \left]\frac{\pi}{2}, \pi\right[\ \text{ or } \ \Psi \epsilon \ \left]-\frac{\pi}{2}, 0\right[$$

$$\lim_{\mathcal{E}\to\mathcal{E}_{\Psi_<}} \Psi(\mathcal{E}) = -\frac{\pi}{2} \qquad \xrightarrow{yields} \quad \Psi \epsilon \ \left]-\frac{\pi}{2}, 0\right[\tag{4.29}$$

$$\xrightarrow{yields} \quad \Psi \ \text{ decreases monotonically}$$

For $\mathcal{E} \ \epsilon \ ]\mathcal{E}_\Psi, 1]$,

$$\mathcal{E} \geq \frac{\frac{4}{\sqrt{3}}\tan(w) - \xi_1}{\xi_2} \qquad \xrightarrow{yields} \quad -4\sin w + \sqrt{3}(\xi_1 + \mathcal{E}\xi_2)\cos w \geq 0$$

$$\xrightarrow{yields} \quad \tan\Psi > 0$$

$$\xrightarrow{yields} \quad \Psi \epsilon \ \left]0, \frac{\pi}{2}\right[\ or \ \Psi \epsilon \ \left]-\pi, -\frac{\pi}{2}\right[$$

$$\lim_{\mathcal{E}\to\mathcal{E}_{\Psi_>}} \Psi(\mathcal{E}) = +\frac{\pi}{2} \qquad \xrightarrow{yields} \quad \Psi \epsilon \ \left]0, \frac{\pi}{2}\right[\tag{4.30}$$

$$\xrightarrow{yields} \quad \Psi \ \text{decreases monotonically}$$

We can see that the Mode mixity Ψ has a discontinuity at the noise symbol $\mathcal{E}_\Psi$. Since the delamination in mixed Modes I and II is described by the Mode mixity in the

Kardomateas Law, all the following derivations will depend on the Mode mixity, more precisely the Mode mixity noise symbol $\mathcal{E}_{\Psi}$ in all of the affine form derivations.

Since any noise symbol $\mathcal{E}$ should be such as $\mathcal{E} \epsilon [-1,1]$, three cases will happen as for the values of $\mathcal{E}_{\Psi}$: $\mathcal{E}_{\Psi} \epsilon [-1,1]$, $\mathcal{E}_{\Psi} < -1$ and $\mathcal{E}_{\Psi} > -1$.

- If $\mathcal{E}_{\Psi} \epsilon [-1,1]$

$D = [-1, \mathcal{E}_{\Psi}[\text{ U }]\mathcal{E}_{\Psi}, 1]$

$$\lim_{\mathcal{E} \to \mathcal{E}_{\Psi_<}} \Psi(\mathcal{E}) = -\frac{\pi}{2} \; and \lim_{\mathcal{E} \to \mathcal{E}_{\Psi_>}} \Psi(\mathcal{E}) = +\frac{\pi}{2}$$

$$\Psi_{\varepsilon} = \frac{-4\xi_2\sqrt{3}}{\left(4\cos w + \sqrt{3}(\xi_1 + \mathcal{E}\xi_2)\sin w\right)^2 + \left(-4\sin w + \sqrt{3}(\xi_1 + \mathcal{E}\xi_2)\cos w\right)^2}$$

$$\xi_2 \geq 0 \quad \xrightarrow{yields} \Psi_{\varepsilon} < 0$$

$$\xrightarrow{yields} \quad \Psi \text{ decreases monotonically}$$

The Affine Arithmetic formulation we are using involves only the noise symbol $\mathcal{E} \epsilon [-1,1]$, but since Ψ is not continuous on $\mathcal{E} \epsilon [-1,1]$, we need to separate the domain of Ψ into two sub-domain where Ψ is continuous:

$$D_1 = \{\mathcal{E} \epsilon [-1,1] \,/\, \mathcal{E} \epsilon [-1, \mathcal{E}_{\Psi}[\,\}$$

$$D_1 = \{\mathcal{E}' \epsilon [-1,1]\} \tag{4.31}$$

and

$$D_2 = \{\mathcal{E}\,\epsilon\,[-1,1]\,/\,\mathcal{E}\,\epsilon\,]\mathcal{E}_{\Psi},1]\,\}$$

$$D_2 = \{\mathcal{E}''\,\epsilon\,[-1,1]\} \tag{4.32}$$

To be able to easily continue the derivations in affine forms, a change of variable was made to obtain Eq. (4.31) and (4.32). The symbol $\mathcal{E}'$ is the noise symbol $\mathcal{E}\,\epsilon\,[-1,\mathcal{E}_{\Psi}[$ and the symbol $\mathcal{E}''$ the noise symbol $\mathcal{E}\,\epsilon\,]\mathcal{E}_{\Psi},1]$. It is now easy to continue the derivation in the affine forms since Ψ is continuous on each of the two domains above.

We know that:

$l = l_1 + \mathcal{E}l_2$, with $\mathcal{E}\,\epsilon\,[-1,\mathcal{E}_{\Psi}[$ U $]\mathcal{E}_{\Psi},1]$

For $\mathcal{E} = -1$,

$$\begin{aligned} l &= l_1 - l_2 \\ &= l_L \end{aligned}$$

for $\mathcal{E} = 1$,

$$\begin{aligned} l &= l_1 + l_2 \\ &= l_U \end{aligned}$$

and for $\mathcal{E} = \mathcal{E}_{\Psi}$,

$$\begin{aligned} l &= l_1 + \mathcal{E}_{\Psi} l_2 \\ &= \frac{l_U + l_L}{2} + \mathcal{E}_{\Psi}\frac{l_U - l_L}{2} \\ &= l_{\Psi} \end{aligned}$$

Since l increases monotonically with $\mathcal{E}$:

$$\mathcal{E} \in [-1, \mathcal{E}_{\Psi}[\xrightarrow{yields} l \in [l_L \,, l_{\Psi}[$$

$$\xrightarrow{yields} l = \frac{l_{\Psi}+l_L}{2} + \mathcal{E}'^{\frac{l_{\Psi}-l_L}{2}} \qquad (4.33)$$

and

$$\mathcal{E} \in]\mathcal{E}_{\Psi}, 1] \xrightarrow{yields} l \in]l_{\Psi}, l_U]$$

$$\xrightarrow{yields} l = \frac{l_{\Psi}+l_U}{2} + \mathcal{E}'' \frac{l_U-l_{\Psi}}{2} \qquad (4.34)$$

- For $\mathcal{E}' \in [-1,1]$ ($\mathcal{E} \in [-1, \mathcal{E}_{\Psi}[$)

The Mode mixity derivation:

Eqs. (4.25) and (4.26) give the upper and lower limits of ξ. We can then write:

$$\xi = \xi_1 + \mathcal{E}'\xi_2$$

From Eq. (4.29) we know that $\Psi \epsilon \left] -\frac{\pi}{2}, 0 \right[$ and $\Psi(\mathcal{E}')$ decreases monotonically :

$$\Psi_U = \Psi(-1)$$

$$= \tan^{-1}\left[\frac{4\cos w + \sqrt{3}(\xi_1 - \xi_2)\sin w}{-4\sin w + \sqrt{3}(\xi_1 - \xi_2)\cos w}\right]$$

$$\boldsymbol{\Psi_U = \tan^{-1}\left[\frac{4\cos w + \sqrt{3}\,\xi_L \sin w}{-4\sin w + \sqrt{3}\xi_L \cos w}\right]} \qquad (4.35)$$

$$\Psi_L = \Psi(1)$$

$$= \tan^{-1}\left[\frac{4\cos w + \sqrt{3}(\xi_1 + \xi_2)\sin w}{-4\sin w + \sqrt{3}(\xi_1 + \xi_2)\cos w}\right]$$

$$= \tan^{-1}\left[\frac{4\cos w + \sqrt{3}\,\xi_U \sin w}{-4\sin w + \sqrt{3}\xi_U \cos w}\right]$$

$$\boldsymbol{\Psi_L = -\frac{\pi}{2}} \qquad (4.36)$$

$$\Psi = \Psi_1 - \mathcal{E}'\Psi_2 \qquad (4.37)$$

<u>The energy release rate derivation:</u>

From Eq. (4.21), $G_{\mathcal{E}'} < 0$. Thus the energy release rate $G(\mathcal{E}')$ monotonically decreases:

$$G_U = G(-1)$$

$$\boldsymbol{G_U} = \boldsymbol{V}\left[\mathcal{E}_{\boldsymbol{0}} - \boldsymbol{H l_L}^{\boldsymbol{-2}}\right][\mathcal{E}_{\boldsymbol{0}} + \boldsymbol{3Hl\_l_L 1^{-2}}] \qquad (4.38)$$

and

$$G_L = G(1)$$

$$\boldsymbol{G_L} = \boldsymbol{V}\left[\mathcal{E}_{\boldsymbol{0}} - \boldsymbol{H}\boldsymbol{l_U}^{\boldsymbol{-2}}\right]\left[\mathcal{E}_{\boldsymbol{0}} + \boldsymbol{3}\boldsymbol{H}\boldsymbol{l_U}^{\boldsymbol{-2}}\right] \tag{4.39}$$

with $G = G_1 - \mathcal{E}'G_2$

The mixed-mode exponent:

$$m(\Psi) = m_I(1 - \sin^2\Psi) + m_{II}\sin^2\Psi$$

Using Eqs. (4.8), (4.11) and (4.37):

$m(\mathcal{E}', \mathcal{E}_2, \mathcal{E}_4) = \left(m_{I_1} + \mathcal{E}_2 m_{I_2}\right)\left(1 - \sin^2(\Psi_1 - \mathcal{E}'\Psi_2)\right) + \left(m_{II_1} + \mathcal{E}_4 m_{II_2}\right)\sin^2(\Psi_1 - \mathcal{E}'\Psi_2)$

$$\xrightarrow{yields} \quad m_{\mathcal{E}_2} = m_{I_2}\left(1 - \sin^2(\Psi_1 - \mathcal{E}\Psi_2)\right) > 0$$

and

$$\xrightarrow{yields} \quad m_{\mathcal{E}_4} = m_{II_2}\sin^2(\Psi_1 - \mathcal{E}\Psi_2) \ > 0$$

then $m(\mathcal{E}_2, \mathcal{E}_4)$ monotonically increases for $\mathcal{E}_2 = [-1,1]$ and $\mathcal{E}_4 = [-1,1]$

$m_{\mathcal{E}'} = 2\Psi_2 \sin(\Psi_1 - \mathcal{E}'\Psi_2)\cos(\Psi_1 - \mathcal{E}'\Psi_2)\left[\left(m_{I_1} + \mathcal{E}_2 m_{I_2}\right) - \left(m_{II_1} + \mathcal{E}_4 m_{II_2}\right)\right]$

we know that for $\mathcal{E}' \epsilon [-1,1]$, $\Psi < 0$

$$\xrightarrow{yields} \quad \sin(\Psi_1 - \mathcal{E}'\Psi_2) < 0 \; and \; \cos(\Psi_1 - \mathcal{E}'\Psi_2) > 0$$

Also we know that m_I is always greater than m_{II}

$$\xrightarrow{yields} \quad m_{I_1} + \mathcal{E}_2 m_{I_2} > m_{II_1} + \mathcal{E}_4 m_{II_2}$$

We can then conclude that $m_{\mathcal{E}'} \leq 0$

Thus *m* monotonically decreases with respect to $\mathcal{E}'$ and :

$$\begin{aligned} m_U &= m(-1,1,1) \\ &= \left(m_{I_1} + m_{I_2}\right)(1 - \sin^2\boldsymbol{\Psi_U}) + \left(m_{II_1} + m_{II_2}\right)\sin^2\boldsymbol{\Psi_U} \end{aligned}$$

$$m_U = \boldsymbol{m_{I_U}}(\mathbf{1} - \mathbf{sin^2}\boldsymbol{\Psi_U}) + \boldsymbol{m_{II_U}}\mathbf{sin^2}\boldsymbol{\Psi_U} \tag{4.40}$$

$$\begin{aligned} m_L &= m(1,-1,-1) \\ &= \left(m_{I_1} - m_{I_2}\right)(1 - \sin^2\boldsymbol{\Psi_L}) + \left(m_{II_1} - m_{II_2}\right)\sin^2\boldsymbol{\Psi_L} \\ &= m_{I_L}(1 - \sin^2\boldsymbol{\Psi_L}) + m_{II_L}\sin^2\boldsymbol{\Psi_L} = \boldsymbol{m_{II_L}} \end{aligned}$$

$$m_L = \boldsymbol{m_{II_L}} \tag{4.41}$$

with $m = m_1 - \mathcal{E}' m_2$

<u>The mixed-mode coefficient:</u>

$$C(\Psi) = C_I(1 - \sin^2\Psi) + C_{II}\sin^2\Psi$$

Using Eqs. (4.7), (4.10) and (4.37):

$$C(\mathcal{E}', \mathcal{E}_1, \mathcal{E}_5) = \left(C_{I_1} + \mathcal{E}_1 C_{I_2}\right)\left(1 - \sin^2(\Psi_1 - \mathcal{E}'\Psi_2)\right) + \left(C_{II_1} + \mathcal{E}_5 C_{II_2}\right)\sin^2(\Psi_1 - \mathcal{E}'\Psi_2)$$

$$\xrightarrow{yields} \quad C_{\mathcal{E}_1} = C_{I_2}\left(1 - \sin^2(\Psi_1 - \mathcal{E}'\Psi_2)\right) \geq 0$$

and

$$\xrightarrow{yields} C_{\mathcal{E}_5} = C_{II_2}\sin^2(\Psi_1 - \mathcal{E}'\Psi_2) \geq 0$$

then $C(\mathcal{E}_1, \mathcal{E}_5)$ monotonically increases for $\mathcal{E}_1 = [-1,1]$ and $\mathcal{E}_5 = [-1,1]$

$C_{\mathcal{E}'} = 2\Psi_2 \sin(\Psi_1 - \mathcal{E}'\Psi_2)\cos(\Psi_1 - \mathcal{E}'\Psi_2)\left[\left(C_{I_1} + \mathcal{E}_1 C_{I_2}\right) - \left(C_{II_1} + \mathcal{E}_5 C_{II_2}\right)\right]$

We know that for $\mathcal{E}' \epsilon [-1,1], \Psi < 0$

$$\xrightarrow{yields} \sin(\Psi_1 - \mathcal{E}'\Psi_2) < 0 \; and \; \cos(\Psi_1 - \mathcal{E}'\Psi_2) > 0$$

Also we know that C_{II} is always greater than C_I

$$\xrightarrow{yields} \quad C_{I_1} + \mathcal{E}_1 C_{I_2} < C_{II_1} + \mathcal{E}_5 C_{II_2}$$

We can then conclude that

$$C_{\mathcal{E}'} > 0$$

Thus *C* monotonically increases with respect to $\mathcal{E}'$ and :

$$\begin{aligned} C_U &= C(1,1,1) \\ &= \left(C_{I_1} + C_{I_2}\right)\left(1 - \sin^2(\Psi_1 - \Psi_2)\right) + \left(C_{II_1} + C_{II_2}\right)\sin^2(\Psi_1 - \Psi_2) \\ &= \boldsymbol{C_{I_U}(1 - \sin^2\Psi_L) + C_{II_U}\sin^2\Psi_L} \end{aligned}$$

$$\boldsymbol{C_U = C_{II_U}} \tag{4.42}$$

$$C_L = C(-1,-1,-1)$$

$$= \left(C_{I_1} - C_{I_2}\right)\left(1 - \sin^2(\Psi_1 + \Psi_2)\right) + \left(C_{II_1} - C_{II_2}\right)\sin^2(\Psi_1 + \Psi_2)$$

$$\boldsymbol{C_L = C_{I_L}(1 - \sin^2\Psi_U) + C_{II_L}\sin^2\Psi_U} \tag{443}$$

With $C = C_1 + \varepsilon' C_2$

The mixed-mode adjusted fracture criteria:

$$\Gamma_0(\Psi) = \mathrm{G}_1^c\left[1 + \left(\frac{\mathrm{G}_1^c}{\mathrm{G}_{11}^c} - 1\right)\sin^2\Psi\right]^{-1}$$

Using Eqs. (4.9), (4.12) and (4.37)

$$\Gamma_0(\varepsilon', \varepsilon_3, \varepsilon_6) = \left(\mathrm{G}_{\mathrm{I}\,1}^c + \varepsilon_6 \mathrm{G}_{\mathrm{I}\,2}^c\right)\left[1 + \left(\frac{\mathrm{G}_{\mathrm{I}\,1}^c + \varepsilon_6 \mathrm{G}_{\mathrm{I}\,2}^c}{\mathrm{G}_{\mathrm{II}_1}^c + \varepsilon_3 \mathrm{G}_{\mathrm{II}_2}^c} - 1\right)\sin^2(\Psi_1 - \varepsilon'\Psi_2)\right]^{-1}$$

$$\xrightarrow{yields} \quad \Gamma_{0_{\varepsilon_3}} = \left(\mathrm{G}_{\mathrm{I}\,1}^c + \varepsilon_6 \mathrm{G}_{\mathrm{I}\,2}^c\right)^2 \mathrm{G}_{\mathrm{II}_2}^c \sin^2(\Psi_1 - \varepsilon'\Psi_2)\left(\mathrm{G}_{\mathrm{II}_1}^c + \varepsilon_3 \mathrm{G}_{\mathrm{II}_2}^c\right)^{-2}\left[1 + \left(\frac{\mathrm{G}_{\mathrm{I}\,1}^c + \varepsilon_6 \mathrm{G}_{\mathrm{I}\,2}^c}{\mathrm{G}_{\mathrm{II}_1}^c + \varepsilon_3 \mathrm{G}_{\mathrm{II}_2}^c} - 1\right)\sin^2(\Psi_1 - \varepsilon'\Psi_2)\right]^{-2} > 0$$

and

$$\xrightarrow{yields} \quad \Gamma_{0_{\varepsilon_6}} = \mathrm{G}_{1_2}^c\left[1 + \left(\frac{\mathrm{G}_{\mathrm{I}\,1}^c + \varepsilon_6 \mathrm{G}_{\mathrm{I}\,2}^c}{\mathrm{G}_{\mathrm{II}_1}^c + \varepsilon_3 \mathrm{G}_{\mathrm{II}_2}^c} - 1\right)\sin^2(\Psi_1 - \varepsilon'\Psi_2)\right]^{-1}\left[1 - \frac{\mathrm{G}_{\mathrm{I}\,1}^c + \varepsilon_6 \mathrm{G}_{\mathrm{I}\,2}^c}{\mathrm{G}_{\mathrm{II}_1}^c + \varepsilon_3 \mathrm{G}_{\mathrm{II}_2}^c}\sin^2(\Psi_1 - \varepsilon'\Psi_2)\left[1 + \left(\frac{\mathrm{G}_{\mathrm{I}\,1}^c + \varepsilon_6 \mathrm{G}_{\mathrm{I}\,2}^c}{\mathrm{G}_{\mathrm{II}_1}^c + \varepsilon_3 \mathrm{G}_{\mathrm{II}_2}^c} - 1\right)\sin^2(\Psi_1 - \varepsilon'\Psi_2)\right]^{-2}\right] > 0$$

then $\Gamma_0(\varepsilon', \varepsilon_3, \varepsilon_6)$ increases monotonically for $\varepsilon_3 = [-1,1]$ and $\varepsilon_6 = [-1,1]$

$$\Gamma_{0_{\mathcal{E}'}} = 2\Psi_2\left(\mathrm{G}^{\mathrm{c}}_{\mathrm{I}_1} + \mathcal{E}_6\mathrm{G}^{\mathrm{c}}_{\mathrm{I}_2}\right)\left(\frac{\mathrm{G}^{\mathrm{c}}_{\mathrm{I}_1}+\mathcal{E}_6\mathrm{G}^{\mathrm{c}}_{\mathrm{I}_2}}{\mathrm{G}^{\mathrm{c}}_{\mathrm{II}_1}+\mathcal{E}_3\mathrm{G}^{\mathrm{c}}_{\mathrm{II}_2}} - 1\right)\sin(\Psi_1 - \mathcal{E}'\Psi_2)\cos(\Psi_1 - \mathcal{E}'\Psi_2)\left[1 + \left(\frac{\mathrm{G}^{\mathrm{c}}_{\mathrm{I}_1}+\mathcal{E}_6\mathrm{G}^{\mathrm{c}}_{\mathrm{I}_2}}{\mathrm{G}^{\mathrm{c}}_{\mathrm{II}_1}+\mathcal{E}_3\mathrm{G}^{\mathrm{c}}_{\mathrm{II}_2}} - 1\right)\sin^2(\Psi_1 - \mathcal{E}'\Psi_2)\right]^{-2}$$

We know from the derivations above that $\sin(\Psi_1 - \mathcal{E}'\Psi_2) < 0$ and $\cos(\Psi_1 - \mathcal{E}'\Psi_2) > 0$

Also we know that $\mathrm{G}^{\mathrm{c}}_{\mathrm{II}}$ is always greater than $\mathrm{G}^{\mathrm{c}}_{\mathrm{I}}$

$$\xrightarrow{yields} \quad \frac{\mathrm{G}^{\mathrm{c}}_{\mathrm{I}_1} + \mathcal{E}_6\mathrm{G}^{\mathrm{c}}_{\mathrm{I}_2}}{\mathrm{G}^{\mathrm{c}}_{\mathrm{II}_1} + \mathcal{E}_3\mathrm{G}^{\mathrm{c}}_{\mathrm{II}_2}} < 1$$

We can conclude that

$$\Gamma_{0_{\mathcal{E}'}} > 0$$

Thus Γ_0 monotonically increases with respect to $\mathcal{E}'$ and:

$$\begin{aligned}\Gamma_{0_U} &= \Gamma_0(1,1,1)\\ &= \left(\mathrm{G}^{\mathrm{c}}_{\mathrm{I}_1} + \mathrm{G}^{\mathrm{c}}_{\mathrm{I}_2}\right)\left[1 + \left(\frac{\mathrm{G}^{\mathrm{c}}_{\mathrm{I}_1} + \mathrm{G}^{\mathrm{c}}_{\mathrm{I}_2}}{\mathrm{G}^{\mathrm{c}}_{\mathrm{II}_1} + \mathrm{G}^{\mathrm{c}}_{\mathrm{II}_2}} - 1\right)\sin^2(\Psi_1 - \Psi_2)\right]^{-1}\\ &= \mathrm{G}^{\mathrm{c}}_{\mathrm{I}_U}\left[1 + \left(\frac{\mathrm{G}^{\mathrm{c}}_{\mathrm{I}_U}}{\mathrm{G}^{\mathrm{c}}_{\mathrm{II}_U}} - 1\right)\sin^2\Psi_L\right]^{-1}\end{aligned}$$

$$\Gamma_{0_U} = \mathbf{G}^{\mathbf{c}}_{\mathbf{I}_{\boldsymbol{U}}} \tag{4.44}$$

$$\begin{aligned}\Gamma_{0_L} &= \Gamma_0(-1,-1,-1)\\ &= \left(\mathrm{G}^{\mathrm{c}}_{\mathrm{I}_1} - \mathrm{G}^{\mathrm{c}}_{\mathrm{I}_2}\right)\left[1 + \left(\frac{\mathrm{G}^{\mathrm{c}}_{\mathrm{I}_1} - \mathrm{G}^{\mathrm{c}}_{\mathrm{I}_2}}{\mathrm{G}^{\mathrm{c}}_{\mathrm{II}_1} - \mathrm{G}^{\mathrm{c}}_{\mathrm{II}_2}} - 1\right)\sin^2(\Psi_1 + \Psi_2)\right]^{-1}\end{aligned}$$

$$\Gamma_{0_L} = \mathbf{G^c_{I}}_{\boldsymbol{L}}\left[\mathbf{1} + \left(\frac{\mathbf{G^c_{I}}_{\boldsymbol{L}}}{\mathbf{G^c_{II}}_{\boldsymbol{L}}} - \mathbf{1}\right)\mathbf{sin^2}\boldsymbol{\Psi_U}\right]^{\mathbf{-1}} \tag{4.45}$$

with $\Gamma_0 = \Gamma_{0_1} + \mathcal{E}'\Gamma_{0_2}$

- For $\mathcal{E}'' \epsilon [-1,1]$ ($\mathcal{E} \epsilon \left]\mathcal{E}_{\Psi}, 1\right]$)

<u>The mode mixity derivation</u>:

Eq. (4.25) and (4.26) give the upper and lower limit of ξ. We can then write:

$$\xi = \xi_1 + \mathcal{E}''\xi_2$$

From Eq. (4.30) we know that $\Psi \epsilon \left]0, \frac{\pi}{2}\right[$ and $\Psi(\mathcal{E}'')$ decreases monotonically:

$$\begin{aligned}
\Psi_U &= \Psi(-1) \\
&= \tan^{-1}\left[\frac{4\cos w + \sqrt{3}(\xi_1 - \xi_2)\sin w}{-4\sin w + \sqrt{3}(\xi_1 - \xi_2)\cos w}\right] \\
&= \mathbf{tan^{-1}}\left[\frac{\mathbf{4\,cos}\,\boldsymbol{w} + \sqrt{\mathbf{3}}\,\boldsymbol{\xi_L}\mathbf{sin}\,\boldsymbol{w}}{\mathbf{-4\,sin}\,\boldsymbol{w} + \sqrt{\mathbf{3}}\boldsymbol{\xi_L}\,\mathbf{cos}\,\boldsymbol{w}}\right] \\
&= \lim_{\mathcal{E} \to \mathcal{E}_{\Psi_>}} \Psi(\mathcal{E})
\end{aligned}$$

$$\boldsymbol{\Psi_U} = +\,\frac{\boldsymbol{\pi}}{\mathbf{2}} \tag{4.46}$$

$$\begin{aligned}
\Psi_L &= \Psi(1) \\
&= \tan^{-1}\left[\frac{4\cos w + \sqrt{3}(\xi_1 + \xi_2)\sin w}{-4\sin w + \sqrt{3}(\xi_1 + \xi_2)\cos w}\right]
\end{aligned}$$

$$\Psi_L \ = \boldsymbol{\tan^{-1}}\left[\frac{\boldsymbol{4\cos w+\sqrt{3}\,\xi_U \sin w}}{\boldsymbol{-4\sin w+\sqrt{3}\xi_U\cos w}}\right] \tag{4.47}$$

$$\Psi = \Psi_1 - \mathcal{E}''\Psi_2 \tag{4.48}$$

<u>The energy release rate derivation:</u>

From Eq. (4.21), $G_{\mathcal{E}''} < 0$. Thus the energy release rate $G(\mathcal{E}'')$ monotonically decreases:

$$G_U = G(-1)$$

$$G_U \ = V\left[\mathcal{E}_0 - H\boldsymbol{l_L}^{-2}\right][\mathcal{E}_0 + 3Hl\_\boldsymbol{l_L}1^{-2}] \tag{4.49}$$

and

$$G_L = G(1)$$

$$G_L = V\left[\mathcal{E}_0 - H\boldsymbol{l_U}^{-2}\right]\left[\mathcal{E}_0 + 3H\boldsymbol{l_U}^{-2}\right] \tag{4.50}$$

With $G = G_1 - \mathcal{E}''G_2$

<u>The mixed-mode exponent:</u>

$$m(\Psi) = m_I(1-\sin^2\Psi) + m_{II}\sin^2\Psi$$

Using Eqs. (4.8), (4.11) and (4.48):

$m(\mathcal{E}', \mathcal{E}_2, \mathcal{E}_4) = \left(m_{I_1} + \mathcal{E}_2 m_{I_2}\right)\left(1-\sin^2(\Psi_1 - \mathcal{E}'\Psi_2)\right) + \left(m_{II_1} + \mathcal{E}_4 m_{II_2}\right)\sin^2(\Psi_1 - \mathcal{E}'\Psi_2)$

$$\xrightarrow{yields} \ \ m_{\mathcal{E}_2} = m_{I_2}\left(1-\sin^2(\Psi_1 - \mathcal{E}\Psi_2)\right) > 0$$

and

$$\xrightarrow{yields} \quad m_{\mathcal{E}_4} = m_{II_2}\sin^2(\Psi_1 - \mathcal{E}\Psi_2) \ > 0$$

then $m(\mathcal{E}_2, \mathcal{E}_4)$ monotonically increases for $\mathcal{E}_2 = [-1,1]$ and $\mathcal{E}_4 = [-1,1]$

$$m_{\mathcal{E}''} = 2\Psi_2 \sin(\Psi_1 - \mathcal{E}''\Psi_2)\cos(\Psi_1 - \mathcal{E}''\Psi_2)\left[\left(m_{I_1} + \mathcal{E}_2 m_{I_2}\right) - \left(m_{II_1} + \mathcal{E}_4 m_{II_2}\right)\right]$$

we know that for $\mathcal{E}'' \epsilon\, [-1,1], \Psi > 0$

$$\xrightarrow{yields} \ \sin(\Psi_1 - \mathcal{E}''\Psi_2) > 0 \ and \ \cos(\Psi_1 - \mathcal{E}''\Psi_2) > 0$$

Also we know that m_I is always greater than m_{II}

$$\xrightarrow{yields} \quad m_{I_1} + \mathcal{E}_2 m_{I_2} > m_{II_1} + \mathcal{E}_4 m_{II_2}$$

We can then conclude that $m_{\mathcal{E}''} > 0$

Thus *m* monotonically increases with respect to $\mathcal{E}''$ and :

$$\begin{aligned} m_U &= m(1,1,1) \\ &= \left(m_{I_1} + m_{I_2}\right)(1 - \sin^2\Psi_L) + \left(m_{II_1} + m_{II_2}\right)\sin^2\Psi_L \end{aligned}$$

$$m_U = \boldsymbol{m_{I_U}(1 - \sin^2\Psi_L) + m_{II_U}\sin^2\Psi_L} \tag{4.51}$$

$$\begin{aligned} m_L &= m(-1,-1,-1) \\ &= \left(m_{I_1} - m_{I_2}\right)(1 - \sin^2\Psi_U) + \left(m_{II_1} - m_{II_2}\right)\sin^2\Psi_U \end{aligned}$$

$$= m_{I_L}(1-\sin^2\Psi_L) + m_{II_L}\sin^2\Psi_L = m_{II_L}$$

$$m_L = \boldsymbol{m_{II_L}} \tag{4.52}$$

With $m = m_1 + \mathcal{E}''m_2$

<u>The mixed-mode coefficient:</u>

$$C(\Psi) = C_I(1-\sin^2\Psi) + C_{II}\sin^2\Psi$$

Using Eqs. (4.7), (4.10) and (4.48):

$$C(\mathcal{E}'', \mathcal{E}_1, \mathcal{E}_5) = \left(C_{I_1} + \mathcal{E}_1 C_{I_2}\right)\left(1-\sin^2(\Psi_1 - \mathcal{E}''\Psi_2)\right)$$
$$+ \left(C_{II_1} + \mathcal{E}_5 C_{II_2}\right)\sin^2(\Psi_1 - \mathcal{E}''\Psi_2)$$

$$\xrightarrow{yields} \quad C_{\mathcal{E}_1} = C_{I_2}\left(1-\sin^2(\Psi_1 - \mathcal{E}''\Psi_2)\right) \geq 0$$

and

$$\xrightarrow{yields} C_{\mathcal{E}_5} = C_{II_2}\sin^2(\Psi_1 - \mathcal{E}''\Psi_2) \geq 0$$

then $C(\mathcal{E}_1, \mathcal{E}_5)$ monotonically increases for $\mathcal{E}_1 = [-1,1]$ and $\mathcal{E}_5 = [-1,1]$

$$C_{\mathcal{E}''} = 2\Psi_2 \sin(\Psi_1 - \mathcal{E}''\Psi_2)\cos(\Psi_1 - \mathcal{E}''\Psi_2)\left[\left(C_{I_1} + \mathcal{E}_1 C_{I_2}\right) - \left(C_{II_1} + \mathcal{E}_5 C_{II_2}\right)\right]$$

We know that for $\mathcal{E}'' \epsilon\ [-1,1]$, $\Psi > 0$

$$\xrightarrow{yields} \sin(\Psi_1 - \mathcal{E}''\Psi_2) > 0 \; and \; \cos(\Psi_1 - \mathcal{E}''\Psi_2) > 0$$

Also we know that C_{II} is always greater than C_I

$$\xrightarrow{yields} \quad C_{I_1} + \varepsilon_1 C_{I_2} < C_{II_1} + \varepsilon_5 C_{II_2}$$

We can then conclude that

$$C_{\varepsilon''} < 0$$

Thus *C* monotonically decreases with respect to ε'' and:

$$\begin{aligned} C_U &= C(-1,1,1) \\ &= \left(C_{I_1} + C_{I_2}\right)\left(1 - \sin^2(\Psi_1 + \Psi_2)\right) + \left(C_{II_1} + C_{II_2}\right)\sin^2(\Psi_1 + \Psi_2) \\ &= C_{I_U}(1 - \sin^2\Psi_L) + C_{II_U}\sin^2\Psi_U \end{aligned}$$

$$C_U = \boldsymbol{C_{II_U}} \tag{453}$$

$$\begin{aligned} C_L &= C(+1,-1,-1) \\ &= \left(C_{I_1} - C_{I_2}\right)\left(1 - \sin^2(\Psi_1 - \Psi_2)\right) + \left(C_{II_1} - C_{II_2}\right)\sin^2(\Psi_1 - \Psi_2) \end{aligned}$$

$$C_L = \boldsymbol{C_{I_L}}(\mathbf{1} - \mathbf{sin^2}\boldsymbol{\Psi_L}) + \boldsymbol{C_{II_L}}\mathbf{sin^2}\boldsymbol{\Psi_L} \tag{4.54}$$

With $C = C_1 - \varepsilon'' C_2$

<u>The mixed-mode adjusted fracture criteria:</u>

$$\Gamma_0(\Psi) = \mathrm{G}_1^c\left[1 + \left(\frac{\mathrm{G}_1^c}{\mathrm{G}_{11}^c} - 1\right)\sin^2\Psi\right]^{-1}$$

Using Eq. (4.9), (4.12) and (4.48)

$$\Gamma_0(\mathcal{E}'',\mathcal{E}_3,\mathcal{E}_6)=\left(G^{c}_{I_1}+\mathcal{E}_6G^{c}_{I_2}\right)\left[1+\left(\frac{G^{c}_{I_1}+\mathcal{E}_6G^{c}_{I_2}}{G^{c}_{II_1}+\mathcal{E}_3G^{c}_{II_2}}-1\right)\sin^2(\Psi_1-\mathcal{E}''\Psi_2)\right]^{-1}$$

$$\xrightarrow{yields}\qquad \Gamma_{0_{\mathcal{E}_3}}=\left(G^{c}_{I_1}+\mathcal{E}_6G^{c}_{I_2}\right)^2G^{c}_{II_2}\sin^2(\Psi_1-\mathcal{E}''\Psi_2)\left(G^{c}_{II_1}+\mathcal{E}_3G^{c}_{II_2}\right)^{-2}\left[1+\left(\frac{G^{c}_{I_1}+\mathcal{E}_6G^{c}_{I_2}}{G^{c}_{II_1}+\mathcal{E}_3G^{c}_{II_2}}-1\right)\sin^2(\Psi_1-\mathcal{E}''\Psi_2)\right]^{-2}>0$$

and

$$\xrightarrow{yields}\quad \Gamma_{0_{\mathcal{E}_6}}=G^{c}_{I_2}\left[1+\left(\frac{G^{c}_{I_1}+\mathcal{E}_6G^{c}_{I_2}}{G^{c}_{II_1}+\mathcal{E}_3G^{c}_{II_2}}-1\right)\sin^2(\Psi_1-\mathcal{E}''\Psi_2)\right]^{-1}\left[1-\frac{G^{c}_{I_1}+\mathcal{E}_6G^{c}_{I_2}}{G^{c}_{II_1}+\mathcal{E}_3G^{c}_{II_2}}\sin^2(\Psi_1-\mathcal{E}''\Psi_2)\left[1+\left(\frac{G^{c}_{I_1}+\mathcal{E}_6G^{c}_{I_2}}{G^{c}_{II_1}+\mathcal{E}_3G^{c}_{II_2}}-1\right)\sin^2(\Psi_1-\mathcal{E}''\Psi_2)\right]^{-2}\right]>0$$

then $\Gamma_0(\mathcal{E}'',\mathcal{E}_3,\mathcal{E}_6)$ increases monotonically for $\mathcal{E}_3=[-1,1]$ and $\mathcal{E}_6=[-1,1]$

$$\Gamma_{0_{\mathcal{E}''}}=2\Psi_2\left(G^{c}_{I_1}+\mathcal{E}_6G^{c}_{I_2}\right)\left(\frac{G^{c}_{I_1}+\mathcal{E}_6G^{c}_{I_2}}{G^{c}_{II_1}+\mathcal{E}_3G^{c}_{II_2}}-1\right)\sin(\Psi_1-\mathcal{E}''\Psi_2)\cos(\Psi_1-\mathcal{E}''\Psi_2)\left[1+\left(\frac{G^{c}_{I_1}+\mathcal{E}_6G^{c}_{I_2}}{G^{c}_{II_1}+\mathcal{E}_3G^{c}_{II_2}}-1\right)\sin^2(\Psi_1-\mathcal{E}''\Psi_2)\right]^{-2}$$

We know from the derivations above that $\sin(\Psi_1-\mathcal{E}''\Psi_2)>0$ and $\cos(\Psi_1-\mathcal{E}''\Psi_2)>0$

Also we know that G^{c}_{II} is always greater than G^{c}_{I}

$$\xrightarrow{yields}\quad \frac{G^{c}_{I_1}+\mathcal{E}_6G^{c}_{I_2}}{G^{c}_{II_1}+\mathcal{E}_3G^{c}_{II_2}}<1$$

We can conclude that

$$\Gamma_{0_{\mathcal{E}''}} < 0$$

Thus Γ_0 monotonically decreases with respect to $\mathcal{E}''$ and:

$$\Gamma_{0_U} = \Gamma_0(-1,1,1)$$

$$= \left(\mathrm{G}^{\mathrm{c}}_{\mathrm{I}_1} + \mathrm{G}^{\mathrm{c}}_{\mathrm{I}_2}\right)\left[1 + \left(\frac{\mathrm{G}^{\mathrm{c}}_{\mathrm{I}_1} + \mathrm{G}^{\mathrm{c}}_{\mathrm{I}_2}}{\mathrm{G}^{\mathrm{c}}_{\mathrm{II}_1} + \mathrm{G}^{\mathrm{c}}_{\mathrm{II}_2}} - 1\right)\sin^2(\Psi_1 + \Psi_2)\right]^{-1}$$

$$= \mathrm{G}^{\mathrm{c}}_{\mathrm{I}_U}\left[1 + \left(\frac{\mathrm{G}^{\mathrm{c}}_{\mathrm{I}_U}}{\mathrm{G}^{\mathrm{c}}_{\mathrm{II}_U}} - 1\right)\sin^2\Psi_U\right]^{-1}$$

$$\Gamma_{0_U} = \mathbf{G}^{\mathbf{c}}_{\mathbf{II}_{\boldsymbol{U}}} \tag{4.55}$$

$$\Gamma_{0_L} = \Gamma_0(+1,-1,-1)$$

$$= \left(\mathrm{G}^{\mathrm{c}}_{\mathrm{I}_1} - \mathrm{G}^{\mathrm{c}}_{\mathrm{I}_2}\right)\left[1 + \left(\frac{\mathrm{G}^{\mathrm{c}}_{\mathrm{I}_1} - \mathrm{G}^{\mathrm{c}}_{\mathrm{I}_2}}{\mathrm{G}^{\mathrm{c}}_{\mathrm{II}_1} - \mathrm{G}^{\mathrm{c}}_{\mathrm{II}_2}} - 1\right)\sin^2(\Psi_1 - \Psi_2)\right]^{-1}$$

$$\Gamma_{0_L} = \mathbf{G}^{\mathbf{c}}_{\mathbf{I}_{\boldsymbol{L}}}\left[\mathbf{1} + \left(\frac{\mathbf{G}^{\mathbf{c}}_{\mathbf{I}_{\boldsymbol{L}}}}{\mathbf{G}^{\mathbf{c}}_{\mathbf{II}_{\boldsymbol{L}}}} - \mathbf{1}\right)\mathbf{sin}^{\mathbf{2}}\boldsymbol{\Psi}_{\boldsymbol{L}}\right]^{\mathbf{-1}} \tag{4.56}$$

With $\Gamma_0 = \Gamma_{0_1} - \mathcal{E}''\Gamma_{0_2}$

- $If\ \mathcal{E}_\Psi > 1$

$\mathcal{E}_\Psi > 1$ means that the discontinuity in Ψ happens after the current length (range) $l = [l_L, l_U] = l_1 + l_2\mathcal{E}$, which is exactly the same case as when we were in $\mathcal{E} \epsilon [-1, \mathcal{E}_\Psi[$

$$\xrightarrow{yields}\ \Psi_{\varepsilon} \leq 0$$

thus $\Psi(\mathcal{E})$ decreases monotonically for $\mathcal{E} = [-1,1]$

$$\Psi_U = \Psi(-1)$$

$$= \tan^{-1}\left[\frac{4\cos w + \sqrt{3}(\xi_1 - \xi_2)\sin w}{-4\sin w + \sqrt{3}(\xi_1 - \xi_2)\cos w}\right]$$

$$\Psi_U = \boldsymbol{tan^{-1}}\left[\frac{\mathbf{4}\,\boldsymbol{cos\,w} + \sqrt{\mathbf{3}}\,\boldsymbol{\xi_L sin\,w}}{\mathbf{-4}\,\boldsymbol{sin\,w} + \sqrt{\mathbf{3}}\boldsymbol{\xi_L}\,\boldsymbol{cos\,w}}\right] \tag{4.57}$$

and

$$\Psi_L = \Psi(1)$$

$$= \tan^{-1}\left[\frac{4\cos w + \sqrt{3}(\xi_1 + \xi_2)\sin w}{-4\sin w + \sqrt{3}(\xi_1 + \xi_2)\cos w}\right]$$

$$\boldsymbol{\Psi_L} = \boldsymbol{tan^{-1}}\left[\frac{\mathbf{4}\,\boldsymbol{cos\,w} + \sqrt{\mathbf{3}}\boldsymbol{\xi_U}\,\boldsymbol{sin\,w}}{\mathbf{-4}\,\boldsymbol{sin\,w} + \sqrt{\mathbf{3}}\boldsymbol{\xi_U}\,\boldsymbol{cos\,w}}\right] \tag{4.58}$$

Using the definition of $\mathcal{E}_{\Psi}$ and knowing that $4\cos w + \sqrt{3}(\xi_1 + \xi_2)\sin w > 0$:

$$\mathcal{E}_{\Psi} > 1 \ \xrightarrow{yields}\ -4\sin w + \sqrt{3}(\xi_1 + \xi_2)\cos w < 0$$

$$\xrightarrow{yields}\ -4\sin w + \sqrt{3}(\xi_1 - \xi_2)\cos w < 0$$

$$\xrightarrow{yields}\ \tan^{-1}\left[\frac{4\cos w + \sqrt{3}(\xi_1 + \xi_2)\sin w}{-4\sin w + \sqrt{3}(\xi_1 + \xi_2)\cos w}\right] < 0$$

and

$$\tan^{-1}\left[\frac{4\cos w+\sqrt{3}(\xi_1-\xi_2)\sin w}{-4\sin w+\sqrt{3}(\xi_1-\xi_2)\cos w}\right]<0$$

Thus $\Psi_U < 0$ and $\Psi_L < 0$ and then $\Psi < 0$ and $\Psi = \Psi_1 - \mathcal{E}\Psi_2$ (Note that for this particular variable $\Psi_1 < 0$ and $\Psi_2 > 0$)

<u>The energy release rate derivation:</u>

From Eq. (4.21),$G_\mathcal{E} < 0$, thus the energy release rate $G(\mathcal{E})$ monotonically decreases and:

$$G_U = \boldsymbol{V}\left[\mathcal{E}_\mathbf{0} - \boldsymbol{H}\boldsymbol{l_L}^{-\mathbf{2}}\right]\left[\mathcal{E}_\mathbf{0} + \mathbf{3}\boldsymbol{H}\boldsymbol{l_L}^{-\mathbf{2}}\right] \tag{4.59}$$

and

$$G_L = \boldsymbol{V}\left[\mathcal{E}_\mathbf{0} - \boldsymbol{H}\boldsymbol{l_U}^{-\mathbf{2}}\right]\left[\mathcal{E}_\mathbf{0} + \mathbf{3}\boldsymbol{H}\boldsymbol{l_U}^{-\mathbf{2}}\right] \tag{4.60}$$

With $G(\mathcal{E}) = G_1 - \mathcal{E}G_2$

<u>The mixed-mode exponent:</u>

We already know that $m(\mathcal{E}_2, \mathcal{E}_4)$ monotonically increases for $\mathcal{E}_2 = [-1,1]$ and $\mathcal{E}_4 = [-1,1]$.

As in the case of $\mathcal{E} \in [-1, \mathcal{E}_\Psi[$,

$$m_\mathcal{E} \leq 0$$

Thus *m* monotonically decreases with respect to $\mathcal{E}$ and :

$$m_U = m(-1,1,1)$$

$$= \left(m_{1_1} + m_{1_2}\right)\left(1 - \sin^2(\Psi_1 + \Psi_2)\right) + \left(m_{11_1} + m_{11_2}\right)\sin^2(\Psi_1 + \Psi_2)$$

$$m_U = \boldsymbol{m_{1_U}}(\mathbf{1} - \mathbf{sin^2}\boldsymbol{\Psi_U}) + \boldsymbol{m_{11_U}}\mathbf{sin^2}\boldsymbol{\Psi_U} \qquad (4.61)$$

$$m_L = m(1, -1, -1)$$

$$= \left(m_{1_1} - m_{1_2}\right)\left(1 - \sin^2(\Psi_1 - \Psi_2)\right) + \left(m_{11_1} - m_{11_2}\right)\sin^2(\Psi_1 - \Psi_2)$$

$$m_L = \boldsymbol{m_{1_L}}(\mathbf{1} - \mathbf{sin^2}\boldsymbol{\Psi_L}) + \boldsymbol{m_{11_L}}\mathbf{sin^2}\boldsymbol{\Psi_L} \qquad (4.62)$$

With $m(\mathcal{E}) = m_1 - \mathcal{E} m_2$

<u>The mixed-mode coefficient:</u>

We already know that $C(\mathcal{E}_1, \mathcal{E}_5)$ monotonically increases for $\mathcal{E}_1 = [-1,1]$ and $\mathcal{E}_5 = [-1,1]$.

As in the case of $\mathcal{E} \epsilon [-1, \mathcal{E}_\Psi[$,

$$C_{\mathcal{E}} > 0$$

Thus *C* monotonically increases with respect to Ɛ and:

$$C_U = C(1,1,1)$$

$$= \left(C_{1_1} + C_{1_2}\right)\left(1 - \sin^2(\Psi_1 - \Psi_2)\right) + \left(C_{11_1} + C_{11_2}\right)\sin^2(\Psi_1 - \Psi_2)$$

$$C_U = \boldsymbol{C_{1_U}}(\mathbf{1} - \mathbf{sin^2}\boldsymbol{\Psi_L}) + \boldsymbol{C_{11_U}}\mathbf{sin^2}\boldsymbol{\Psi_L} \qquad (4.63)$$

$$C_L = C(-1, -1, -1)$$

$$= \left(C_{1_1} - C_{1_2}\right)\left(1 - \sin^2(\Psi_1 + \Psi_2)\right) + \left(C_{11_1} - C_{11_2}\right)\sin^2(\Psi_1 + \Psi_2)$$

$$C_L = \boldsymbol{C_{1_L}(1 - \sin^2\Psi_U) + C_{11_L}\sin^2\Psi_U} \tag{4.64}$$

With $C(\mathcal{E}) = C_1 + \mathcal{E}C_2$

<u>The mixed-mode adjusted fracture criteria:</u>

We already know that $\Gamma_0(\mathcal{E}_3, \mathcal{E}_6)$ increases monotonically for $\mathcal{E}_3 = [-1,1]$ and $\mathcal{E}_6 = [-1,1]$.

As in the case of $\mathcal{E} \epsilon [-1, \mathcal{E}_\Psi[$,

$$\Gamma_{0_{\mathcal{E}'}} > 0$$

Thus Γ_0 monotonically increases with respect to $\mathcal{E}$ and:

$$\begin{aligned}\Gamma_{0_U} &= \Gamma_0(1,1,1)\\ &= \left(\mathrm{G}^{\mathrm{c}}_{1_1} + \mathrm{G}^{\mathrm{c}}_{1_2}\right)\left[1 + \left(\frac{\mathrm{G}^{\mathrm{c}}_{1_1} + \mathrm{G}^{\mathrm{c}}_{1_2}}{\mathrm{G}^{\mathrm{c}}_{11_1} + \mathrm{G}^{\mathrm{c}}_{11_2}} - 1\right)\sin^2(\Psi_1 - \Psi_2)\right]^{-1}\end{aligned}$$

$$\Gamma_{0_U} = \boldsymbol{\mathrm{G}^{\mathrm{c}}_{1_U}\left[1 + \left(\frac{\mathrm{G}^{\mathrm{c}}_{1_U}}{\mathrm{G}^{\mathrm{c}}_{11_U}} - 1\right)\sin^2\Psi_L\right]^{-1}} \tag{4.65}$$

$$\begin{aligned}\Gamma_{0_L} &= \Gamma_0(-1,-1,-1)\\ &= \left(\mathrm{G}^{\mathrm{c}}_{1_1} - \mathrm{G}^{\mathrm{c}}_{1_2}\right)\left[1 + \left(\frac{\mathrm{G}^{\mathrm{c}}_{1_1} - \mathrm{G}^{\mathrm{c}}_{1_2}}{\mathrm{G}^{\mathrm{c}}_{11_1} - \mathrm{G}^{\mathrm{c}}_{11_2}} - 1\right)\sin^2(\Psi_1 + \Psi_2)\right]^{-1}\end{aligned}$$

$$\Gamma_{0_L} = \boldsymbol{\mathrm{G}^{\mathrm{c}}_{1_L}\left[1 + \left(\frac{\mathrm{G}^{\mathrm{c}}_{1_L}}{\mathrm{G}^{\mathrm{c}}_{11_L}} - 1\right)\sin^2\Psi_U\right]^{-1}} \tag{4.66}$$

With $\Gamma_0(\mathcal{E}) = \Gamma_{0_1} + \mathcal{E}\Gamma_{0_2}$

- If $\mathcal{E}_\Psi < -1$

$\mathcal{E}_\Psi < -1$ means that the discontinuity in Ψ happens before the current length (range) $l = [l_L, l_U] = l_1 + l_2\mathcal{E}$, which is exactly the same case as when we were in $\mathcal{E} \epsilon\ ]\mathcal{E}_\Psi, 1]$

$\xrightarrow{yields}\ \Psi_\varepsilon \leq 0$

thus $\Psi(\mathcal{E})$ decreases monotonically for $\mathcal{E} = [-1,1]$

$$\Psi_U = \Psi(-1)$$

$$= \tan^{-1}\left[\frac{4\cos w + \sqrt{3}(\xi_1 - \xi_2)\sin w}{-4\sin w + \sqrt{3}(\xi_1 - \xi_2)\cos w}\right]$$

$$\Psi_U = \boldsymbol{tan^{-1}}\left[\frac{\boldsymbol{4\,cos\,w + \sqrt{3}\,\xi_L sin\,w}}{\boldsymbol{-4\,sin\,w + \sqrt{3}\xi_L\,cos\,w}}\right] \tag{4.67}$$

and

$$\Psi_L = \Psi(1)$$

$$= \tan^{-1}\left[\frac{4\cos w + \sqrt{3}(\xi_1 + \xi_2)\sin w}{-4\sin w + \sqrt{3}(\xi_1 + \xi_2)\cos w}\right]$$

$$\Psi_L = \boldsymbol{tan^{-1}}\left[\frac{\boldsymbol{4\,cos\,w + \sqrt{3}\xi_U\,sin\,w}}{\boldsymbol{-4\,sin\,w + \sqrt{3}\xi_U\,cos\,w}}\right] \tag{4.68}$$

Using the definition of $\mathcal{E}_\Psi$ and knowing that $4\cos w + \sqrt{3}(\xi_1 + \xi_2)\sin w > 0$:

$$\mathcal{E}_\Psi < -1 \xrightarrow{yields} -4\sin w + \sqrt{3}(\xi_1 - \xi_2)\cos w > 0$$

$$\xrightarrow{yields} -4\sin w + \sqrt{3}(\xi_1 + \xi_2)\cos w > 0$$

$$\xrightarrow{yields} \tan^{-1}\left[\frac{4\cos w + \sqrt{3}(\xi_1 - \xi_2)\sin w}{-4\sin w + \sqrt{3}(\xi_1 - \xi_2)\cos w}\right] > 0$$

$$\xrightarrow{yields} \tan^{-1}\left[\frac{4\cos w + \sqrt{3}(\xi_1 + \xi_2)\sin w}{-4\sin w + \sqrt{3}(\xi_1 + \xi_2)\cos w}\right] > 0$$

Thus $\Psi_U > 0$, $\Psi_L > 0$ and then $\Psi > 0$

With $\Psi = \Psi_1 - \mathcal{E}\Psi_2$

The energy release rate derivation:

From Eq. (4.21),$G_\mathcal{E} < 0$, thus the energy release rate $G(\mathcal{E})$ monotonically decreases and:

$$G_U = \boldsymbol{V}\left[\boldsymbol{\mathcal{E}_0} - \boldsymbol{Hl_L}^{-2}\right]\left[\boldsymbol{\mathcal{E}_0} + \boldsymbol{3Hl_L}^{-2}\right] \tag{4.69}$$

and

$$G_L = \boldsymbol{V}\left[\boldsymbol{\mathcal{E}_0} - \boldsymbol{Hl_U}^{-2}\right]\left[\boldsymbol{\mathcal{E}_0} + \boldsymbol{3Hl_U}^{-2}\right] \tag{4.70}$$

With $G(\mathcal{E}) = G_1 - \mathcal{E}G_2$

<u>The mixed-mode exponent:</u>

We already know that $m(\mathcal{E}_2, \mathcal{E}_4)$ monotonically increases for $\mathcal{E}_2 = [-1,1]$ and $\mathcal{E}_4 = [-1,1]$.

As in the case of $\mathcal{E} \epsilon \,]\mathcal{E}_{\Psi}, 1]$,

$$m_{\mathcal{E}} \geq 0$$

Thus *m* monotonically increases with respect to Ɛ and :

$$\begin{aligned} m_U &= m(1,1,1) \\ &= \left(m_{I_1} + m_{I_2}\right)\left(1 - \sin^2(\Psi_1 - \Psi_2)\right) + \left(m_{II_1} + m_{II_2}\right)\sin^2(\Psi_1 - \Psi_2) \end{aligned}$$

$$m_U = \boldsymbol{m_{I_U}}(\mathbf{1} - \mathbf{sin^2}\boldsymbol{\Psi_L}) + \boldsymbol{m_{II_U}}\mathbf{sin^2}\boldsymbol{\Psi_L} \tag{4.71}$$

$$\begin{aligned} m_L &= m(-1,-1,-1) \\ &= \left(m_{I_1} - m_{1_2}\right)\left(1 - \sin^2(\Psi_1 + \Psi_2)\right) + \left(m_{II_1} - m_{II_2}\right)\sin^2(\Psi_1 + \Psi_2) \end{aligned}$$

$$m_L = \boldsymbol{m_{I_L}}(\mathbf{1} - \mathbf{sin^2}\boldsymbol{\Psi_U}) + \boldsymbol{m_{II_L}}\mathbf{sin^2}\boldsymbol{\Psi_U} \tag{4.72}$$

With $m(\mathcal{E}) = m_1 + \mathcal{E}m_2$

<u>The mixed-mode coefficient:</u>

We already know that $C(\mathcal{E}_1, \mathcal{E}_5)$ monotonically increases for $\mathcal{E}_1 = [-1,1]$ and $\mathcal{E}_5 = [-1,1]$.

As in the case of $\mathcal{E} \epsilon \,]\mathcal{E}_{\Psi}, 1]$,

$$C_{\mathcal{E}} < 0$$

Thus *C* monotonically decreases with respect to $\mathcal{E}$ and:

$$\begin{aligned} C_U &= C(-1,1,1) \\ &= \left(C_{I_1} + C_{I_2}\right)\left(1 - \sin^2(\Psi_1 + \Psi_2)\right) + \left(C_{II_1} + C_{II_2}\right)\sin^2(\Psi_1 + \Psi_2) \end{aligned}$$

$$C_U = \boldsymbol{C_{I_U}}(\mathbf{1} - \mathbf{sin^2}\boldsymbol{\Psi_U}) + \boldsymbol{C_{II_U}}\mathbf{sin^2}\boldsymbol{\Psi_U} \tag{4.73}$$

$$\begin{aligned} C_L &= C(1,-1,-1) \\ &= \left(C_{I_1} - C_{I_2}\right)\left(1 - \sin^2(\Psi_1 - \Psi_2)\right) + \left(C_{II_1} - C_{II_2}\right)\sin^2(\Psi_1 - \Psi_2) \end{aligned}$$

$$C_L = \boldsymbol{C_{I_L}}(\mathbf{1} - \mathbf{sin^2}\boldsymbol{\Psi_L}) + \boldsymbol{C_{II_L}}\mathbf{sin^2}\boldsymbol{\Psi_L} \tag{4.74}$$

with $C(\mathcal{E}) = C_1 - \mathcal{E}C_2$

<u>The mixed-mode adjusted fracture criteria:</u>

We already know that $\Gamma_0(\mathcal{E}_3, \mathcal{E}_6)$ increases monotonically for $\mathcal{E}_3 = [-1,1]$ and $\mathcal{E}_6 = [-1,1]$.

As in the case of $\mathcal{E} \epsilon \,]\mathcal{E}_{\Psi}, 1]$,

$$\Gamma_{0_{\mathcal{E}}} < 0$$

Thus Γ_0 monotonically decreases with respect to $\mathcal{E}$ and:

$$\Gamma_{0_U} = \Gamma_0(-1,1,1)$$

$$= \left(\mathrm{G}^{\mathrm{c}}_{\mathrm{I}_1} + \mathrm{G}^{\mathrm{c}}_{\mathrm{I}_2}\right)\left[1 + \left(\frac{\mathrm{G}^{\mathrm{c}}_{\mathrm{I}_1} + \mathrm{G}^{\mathrm{c}}_{\mathrm{I}_2}}{\mathrm{G}^{\mathrm{c}}_{\mathrm{II}_1} + \mathrm{G}^{\mathrm{c}}_{\mathrm{II}_2}} - 1\right)\sin^2(\Psi_1 + \Psi_2)\right]^{-1}$$

$$\Gamma_{0_U} = \boldsymbol{\mathrm{G}^{\mathrm{c}}_{\mathrm{I}_U}\left[1 + \left(\frac{\mathrm{G}^{\mathrm{c}}_{\mathrm{I}_U}}{\mathrm{G}^{\mathrm{c}}_{\mathrm{II}_U}} - 1\right)\sin^2\Psi_U\right]^{-1}} \tag{4.75}$$

$$\Gamma_{0_L} = \Gamma_0(1,-1,-1)$$

$$= \left(\mathrm{G}^{\mathrm{c}}_{\mathrm{I}_1} - \mathrm{G}^{\mathrm{c}}_{\mathrm{I}_2}\right)\left[1 + \left(\frac{\mathrm{G}^{\mathrm{c}}_{\mathrm{I}_1} - \mathrm{G}^{\mathrm{c}}_{\mathrm{I}_2}}{\mathrm{G}^{\mathrm{c}}_{\mathrm{II}_1} - \mathrm{G}^{\mathrm{c}}_{\mathrm{II}_2}} - 1\right)\sin^2(\Psi_1 - \Psi_2)\right]^{-1}$$

$$\Gamma_{0_L} = \boldsymbol{\mathrm{G}^{\mathrm{c}}_{\mathrm{I}_L}\left[1 + \left(\frac{\mathrm{G}^{\mathrm{c}}_{\mathrm{I}_L}}{\mathrm{G}^{\mathrm{c}}_{\mathrm{II}_L}} - 1\right)\sin^2\Psi_L\right]^{-1}} \tag{4.76}$$

With $\Gamma_0(\mathcal{E}) = \Gamma_{0_1} - \mathcal{E}\Gamma_{0_2}$

In Chapter 6, Eqs. (4.6) to (4.12) and all the equations in bold are used and numerically computed in Matlab to predict the lower and upper value of the delamination growth range of values at every cycle N. We have now equations that can directly be used for prognosis for any material as long as the growth law used is Kardomateas Law.

Chapter 5

Mode I and Mode II Interlaminar Fracture Toughness and Fatigue Characterization of Carbon-Fiber Epoxy Composite Material

In this section the steps necessary to compute the uncertain parameters of Kardomateas Law are shown. The average value (obtained by average summation or using fitting curves) of these parameters as well as their range is obtained. In the case of Kardomateas, all the necessary parameters are obtained by characterizing the pure Mode I and pure Mode II of a specimen built ~~in~~ of the same material as the one that will be studied using the Kardomateas Law in mixed Modes I and II.

5.1 Mode I Interlaminar Fracture Toughness and Fatigue Characterization of Carbon-Fiber Epoxy Composite Material

5.1.1 Scope

This section describes the characterization of the Mode I fracture opening of fiber-reinforced carbon materials. The characterization included both the determination of the value of the interlaminar fracture toughness $\mathrm{G}_{\mathrm{I}}^{\mathrm{c}}$, the Kardomateas Law exponent, and coefficient values m_I and C_I. The fracture thoughness value, which is the critical amount of energy required to propagate a pure Mode I crack, is determined by following the Griffith criterion [18], under a quasi-static Mode I test. The fatigue delamination growth on pure Mode I is then studied to obtain the Kardomateas Law exponent and coefficient.

All the tests are conducted using Double Cantilever Beam (DCB) specimens (see Figures 5.1).

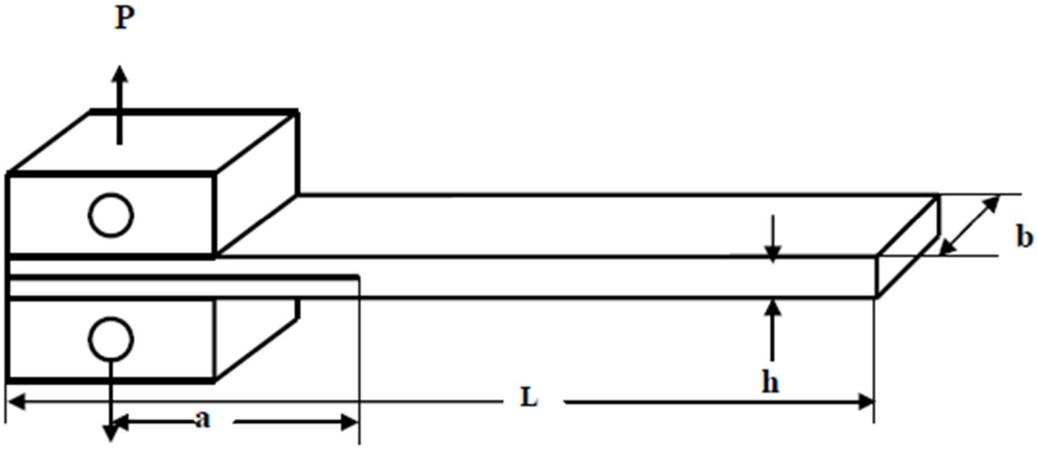

Figure 5.1a. Double Cantilever Beam (DCB) Specimen.

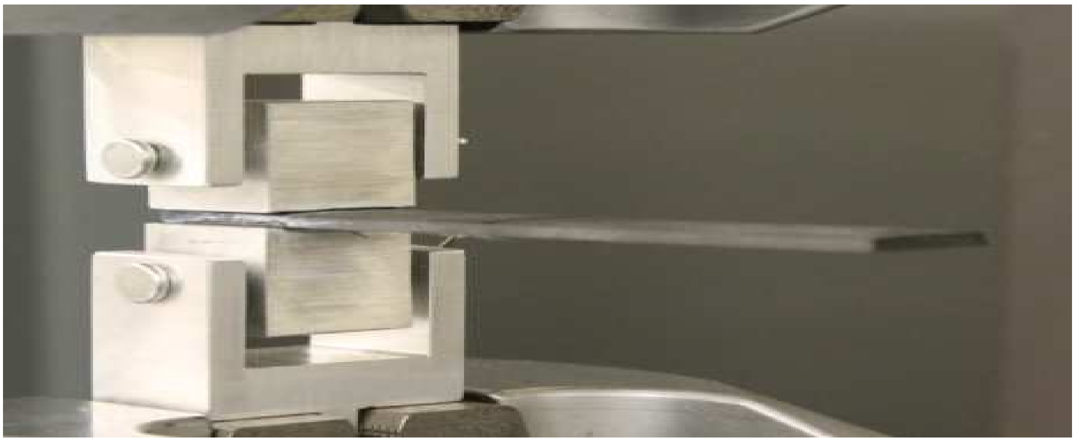

Figure 5.1b. DCB test configuration for fracture and fatigue characterization.

5.1.2 Summary of the Double Cantilever Beam Test

The DCB specimen shown in Figures 5.1a and 5.1b consist of a rectangular laminate composite beam of uniform thickness, with a midplane nonadhesive insert at one end that serves as a delamination initiator. Tension forces are applied to the beam by means of loading blocks, bonded to the insert end of the beam. The delamination length is measured from the load blocks rotation axis.

5.1.3 Methodology

The characterization of the Mode I fracture opening depends on several measurements that should be made with a properly calibrated test machine. It is necessary to determine with accuracy the following variables: the initial delamination length a_0, the delamination length during the test a, the applied load and the opening displacement at the point of the load application P and δ. Since the Mode I fracture is well known and defined by ASTM standards, only the data and information needed for our prognosis model are shown in this section.

5.1.3.1 Determination of the Delamination Length

According to ASTM D5528-13 standard [19], the device pinpointing the delamination front should have an accuracy of at least $\pm 0.5\ mm$ $(\pm 0.02\ in)$. Two main methods have been frequently used to measure the delamination length: the use of crack length gages or visual methods.

The use of crack length gages bonded to the specimen has several disadvantages [20]:

The sensors are manufactured usually in relatively small sizes and may not always measure the full length of the delamination.

The sensors may become unreliable during fatigue tests because of the fatigue of the sensors.

Visual methods, on the other hand usually require putting some precision marks on the laminates. Also the tests usually have to be stopped for each of the length readings to be performed. Small delamination growths are also very difficult to measure accurately with this method. Another big issue is the synchronization of load-displacement data with the delamination length data.

As good alternative to conventional visual systems, an automated delamination length measurement system has been proposed by Yarlagadda *et al.* [21] where a time domain reflectometry system would be used by equipping the laminates with wires. Richter *et al.* [22] described a set of image processing trials for static Mode I laminates. In [20] F.Lahuerta *et al.* used a visual technique based on video image processing for measurements of the delamination length in Mode I for both static and fatigue tests for glass fiber reinforced composites.

In this paper a visual method was used for both quasi-static and fatigue loading of the composite beam to determine the delamination length due to the opening of the beam.

5.1.3.2 Use of Camera Recorder in Synchronization with the Load Displacement Signal

To be able to meet the accuracy requirement for the delamination measurements procedure some steps advised in [20] were followed:

- The laminates were painted in white and matte paint was used to avoid light reflection
- A thin layer of water-based typewriter correction fluid was used to coat both edges of the specimen just ahead of the insert to aid in the visual detection of the delamination onset
- The laminate was oriented perpendicular to the camera
- The initial delamination tip, at the end of the insert was marked with a thick vertical line. The entire 2.5 inch length of the non-cracked specimen was marked at every 1/16 inch, from the tip of the insert
- Since the part of the composite that has not been delaminated yet is not deforming, it remains horizontal. The undelaminated part is then measured using the vertical marks in the images taken by the camera recorder. The delamination length of the laminate is then calculated as the total marked length + the initial delamination length due to the insert – the undelaminated length.

LabVIEW was used to automatically and externally control the camera recorder and the loading machine. Since LabVIEW was used as the data acquisition system to retrieve the load-displacement data from the loading machine, both the camera and the loading machine were synchronized following the logic flow below.

- An output signal was sent from LabVIEW to start the loading machine and to control the displacement rate of the loading blocks fixed to the loading machine
- Two synchronized and simultaneous signals are periodically sent from LabVIEW; one to trigger the camera to make a video snapshot of the opened beam and the second to record the corresponding load-displacement data
- Every snapshot ~~is~~ was then linked to a load-displacement data point and to a precise time during the whole test procedure

5.1.3.3 *Load Versus Opening Displacement Record*

The opening displacement was estimated as the crosshead separation of the composite. The internal X-Y plotter of the loading test device was used as a permanent record during the test. Also, the load vs. displacement data was digitally extracted from the loading test device through LabVIEW.

5.1.4 Material and Test Specimens

Twenty-two plies zero-degree unidirectional test specimens following the

ASTM D5528-13 specimen size specifications were used. 5 in long by 0.8 in wide specimens made of carbon reinforced unidirectional fiber T700S manufactured by TORAYCA, were built. Actual specimen dimensions were measured at three different locations and the average values shown. A 13 μm thick and 2.5 in long Teflon film was inserted between the tenth and eleventh plies which corresponds to a value of a_0 of 1.7 in. Steel loading blocks of 1 x 1 x 1 in^3were properly cleaned before usage and bonded to the laminates with a cyanoacrylate adhesive to avoid debonding of the tab during the testing.

5.1.5 Static Mode I Fracture Characterization

The aim of the static tests was only to determine the value of G_I^c . Three definitions for an initiation value of G_I^c have been evaluated during round-robin testing [23]. In our study only G_I^c values determined using the load and deflection measured at the point of deviation from linearity in the load-displacement curve (NL) was used. All tests performed for the static characterization of the laminates were carried out on the MTS machine, 100 KN maximum capacity with a 50 KN load cell, following ASTM D5528-13. Six specimens were tested in fracture Mode I. For the calculation of the Mode I fracture toughness of the laminates, only the Compliance Calibration Method (CC) [24] was used. The testing machine was operated in the displacement control mode during the characterization.

5.1.5.1 Initial Loading

The specimens were loaded at a constant displacement rate of 0.25 in/min starting from a zero load applied. The loading was stopped after the delamination reached 2/16 in from the film insert. The point on the load-displacement curve and data value that corresponds to a sudden drop of the load value was recorded. The specimens were then unloaded at a constant crosshead rate of 1.2 in/min. The position of the delamination's tip was marked in red on both edges after unloading the specimens.

5.1.5.2 *Reloading*

The specimens were reloaded at a constant displacement rate of 0.25 in/min again from a zero load until the delamination's tip reached the last vertical marks on the specimens. Finally the specimens were unloaded again at a constant crosshead rate of 1.2 in/min. During both the initial loading and the reloading the load and displacement signals as well as the snapshot of the delamination's tip position were recorded.

5.1.6 Fatigue Mode I Characterization

The DCB fatique tests were performed to determine the Kardomateas constants (m_I and C_I). To do so the delamination growth had to be studied. All the fatigue tests were performed also on the same MTS machine as for the static tests. Six specimens with the same dimensions, same material and same initial delamination properties as the static test specimens were used for the fatigue tests. The fatigue tests were operated also in displacement control mode with constant displacement amplitude. The specimens were cycled between a minimum displacement δ_{min} and maximum displacement δ_{max} such that the value of the load ratio $\delta_{min}/\delta_{max}$ was chosen equal to 0.1. The maximum displacement δ_{max} was chosen by setting the value of the ratio between δ_{max}^2 and the square of the average displacements at maximum load in the static tests ($\delta_{max}^2/[\delta_{cr}]_{avg}^2$) between 0.1 and 0.6. The specimens were then subjected to a sinusoidal cyclic loading at a frequency of 8 Hz with the stress values described above. Video snapshots were taken at every 1000 cycles below a number of test cycles of 200,000 cycles and every 5000 cycles above that value, for the delamination length records. The force and displacement data were acquired at the same time as the snapshot (every 500 cycles below a number of test cycle of 200,000 cycles and every 5000 cycles above that value). The number of cycles N_a at which the delamination onset happened was recorded.

5.1.7 Data Reduction Methods

5.1.7.1 Static Tests

Data reduction was conducted to obtain the Mode I fracture toughness G_I^c of the specimens. Only the Compliance Calibration method (CC) was used. All the data (load, displacement and delamination) used for the data reduction were the data corresponding to the visually observed delamination onset as well as the delamination propagation values.

Compliance Calibration (CC) Method:

Using the visually observed delamination onset values and all the propagation values of the delamination, a least squares plot of $log(C)$ versus $log\ (a)$ was generated. The exponent n, that is the slope of the straight line through the data that results in the best least-squares fit, was calculated such as $= \Delta y / \Delta x$. b is the specimen width and a the crack delamination. The interlaminar Mode I fracture toughness is then:

$$G_I = \frac{nP\delta}{2ba} \tag{5.1}$$

5.1.7.2 *Fatigue Tests*

In order to perform the differentiation of the delamination length with respect to the number of cycles da/dN, two different methods were described in ASTM E647-13a [25] . In our study only the incremental polynomial method was used as for data reduction.

The Incremental Polynomial Method

This method involves fitting a second order polynomial to a set of (2n+1) successive data points, where n is a non-zero integer, usually between 1 and 4. The equation for the crack length fit is

$$\hat{a}_i = b_0 + b_1\left(\frac{N_i - C_1}{C_2}\right) + b_2\left(\frac{N_i - C_1}{C_2}\right)^2 \qquad (5.2)$$

with

$$-1 \leq \left(\frac{N_i - C_1}{C_2}\right) \leq 1$$

and b_0, b_1 and b_2 are the regression parameters that are determined by the least squares method over the range $a_{i-n} \leq a \leq a_{i-n}$. The value of $\hat{a}_i$ is the fitted value of the crack length corresponding to N_i. The parameters $C_1 = (N_{i-n} + N_{i+n})/2$ and $C_2 = (N_{i+n} - N_{i-n})/2$ are used to scale the input data to avoid numerical difficulties in determining the regression parameters. The parabola computed by the fitted crack length $\hat{a}_i$ is obtained to compute the growth rate:

$$(da/dN)_{\hat{a}_i} = b_1/C_2 + \frac{2b_2(N_i - C_1)}{{C_2}^2} \qquad (5.3)$$

The data points $(\hat{a}_i, N_i)$ are used to compute the value of ΔG.

For our data reduction Eqs. 5.2 and 5.3, for n = 3, for 7 successive data points were used.

5.1.8 Mode I Fracture and Fatigue Tests Results

The different values of $\mathrm{G_I^c}$ obtained for the differents specimen are summarized in Table 5.1. These values were averaged in order to be used in the prediction of the Kardomateas Law. The range in Table 5.1 will be used for the uncertainty of $\mathrm{G_I^c}$ in Chapter 6 for Affine Arithmetic prediction. The displacement values corresponding to the maximum load during the fracture test are also shown.

The fatigue tests were run at maximum displacement corresponding to a ratio of $\delta_{max}^2 / [\delta_{cr}]_{avg}^2$ between 0.1 and 0.6. Table 5.2 shows the differents specimens used for the fatigue test as well as their displacement ratio and their maximum fatigue cycles.

The maximum fracture toughness G_{Imax}, during each fatigue test was determined for every delamination length a, using Eq. 5.1:

$$G_I = \frac{nP\delta}{2ba}$$

$$G_{Imax} = \frac{nP\delta_{max}}{2ba} \tag{5.4}$$

with δ_{max} as given in Table 5.2, P being measure at every delamination length a. For every fatigue test, δ_{max} will be constant but P, G_{Imax} and a will vary.

Table 5.1 Mode I Interlaminar Fracture Toughness Values

Specimen ID	G_I^c $(in.\frac{lb}{in^2})$	F_{max} (lb)	$\delta_{cr}\ at\ F_{max}$ (in)
1	1.03	20	0.595
2	1.10	19	0.62
3	1.015	18.5	0.59
4	1.02	22	0.605
5	1.11	20.2	0.62
6	1.07	21	0.603
Average	1.0575	-	0.606
Range for AA	**[1.02,1.11]**	-	-

After the fatigue tests were completed, the fatigue growth curves of each of the six specimens were plotted.

Since the purpose of this section is to obtain the Mode I coefficient for the Kardomateas Law, the growth curves were plotted following the Kardomateas equation:

$$\frac{da}{dN} = \frac{C_I \tilde{G}_{max}{}^{m_I}}{1 - \tilde{G}_{max}} \tag{5.5}$$

where $\tilde{G}_{max} = G_{Imax}/G_I^c$

Table 5.2 Fatigue Mode I Test Matrix

Specimen ID	$\frac{\delta_{max}^2}{[\delta_{cr}]_{avg}^2}$	δ_{max} (in)	Max. Cycles
F1	0.6	0.469	1,550,280
F2	0.6	0.469	1,348,500
F3	0.5	0.429	578,450
F4	0.5	0.429	602,540
F5	0.1	0.192	250348
F6	0.1	0.192	264800

Eq. 5.4 is the same as Eq. 4.3 just that here it is applied to only Mode I instead of a mixed Modes I and II. Eq. 5.4 was transformed to:

$$(1 - \tilde{G}_{max})\frac{da}{dN} = C_I \tilde{G}_{max}{}^{m_I} \tag{5.6}$$

Eq. 5.6 was then plotted for each of the fatigue specimens and ~~fits~~ fit to a power law $y = ax^t$. The coefficient C_I ~~is~~ was then equal to a and the exponent $m_I = t$. The lower value of C_I and m_I from all the power law fits were taken as, respectively, the lower value of the range of C_I and the range of m_I and the ~~t~~ largest value of C_I and m_I, taken as the upper value of the range of C_I and the range of m. Finally all of the fatigue growth curves were plotted together on one graph and a unique power law fit was obtained. The coefficient and exponent of that power law fit were used respectively as the mean value of C_I and the mean value of m_I.

Table 5.3 shows the Kardomateas coefficient and exponent obtained from each of the fatigue specimens as well as their mean value.

Table 5.3 Kardomateas Mode I Coefficient and Exponent Values

Specimen ID	C_I	m_I
F1	0.00015	9.21
F2	0.00006	9.15
F3	0.00006	8.42
F4	0.00004	6.83
F5	0.00002	5.42
F6	0.00001	5.26
Mean	0.00002	5.42
Range	[0.00001,0.00015]	[5.23,9.21]

5.2 Mode II Interlaminar Fracture Toughness and Fatigue Characterization of Carbon-Fiber Epoxy Composite Material

5.2.1 Scope

This section describes the characterization of the Mode II fracture opening of fiber-reinforced composite materials. The characterization included both the determination of the value of the interlaminar fracture toughness $\mathrm{G}_{\mathrm{II}}^{\mathrm{c}}$ and the Paris Law exponent and coefficient values m_{II} and C_{II}. All the tests were conducted using the End-Notched Flexure (ENF) specimens (Figure 5.2).

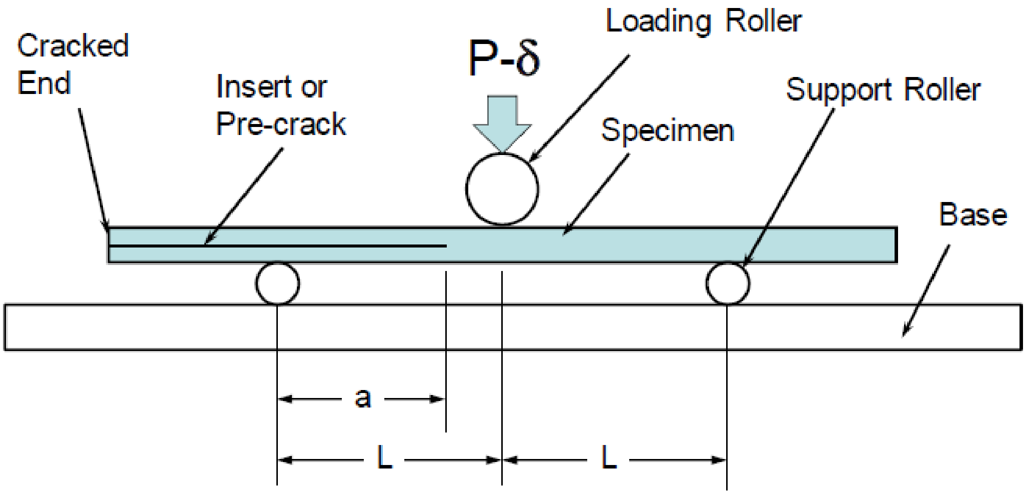

Figure 5.2. End-Notched Flexure (ENF) or 3-Point Bending Test [26].

Unlike the Mode I fracture toughness DCM test which is described in ASTM D5528-13, the ENF test for Mode II fracture toughness is currently under review by ASTM as a potential standard test method. In [26], T. Kevin O'Brien *et al*. following the ASTM draft for Mode II fracture toughness using the ENF test, studied the Mode II interlaminar fracture toughness and fatigue characterization of a graphite epoxy composite material. Their test approach, methods and procedures were followed in this report to characterize the Mode II fracture and fatigue of our specimens. The fatigue delamination onset and growth on pure Mode II were then studied to obtain the Kardomateas Mode II exponent and coefficient.

5.2.2 Summary of the End-Notched Flexure Test

The ENF specimens consisted of rectangular laminate composite beams of uniform thickness, with a midplane nonadhesive insert at one end that serves at a delamination initiator. The specimen were then loaded in three-point-bending as shown in Figure 5.2. The delamination length ~~is~~ was measured from the left support roller and the half-span length, L is the distance from the support rollers to the center loading roller.

5.2.3 Methodology

The characterization of a Mode II fracture opening depends on several measurements that should be made with a properly calibrated test machine. It is necessary to determine with accuracy the following variables: the initial delamination length a_0, the delamination length during the test a, the applied load and the opening displacement at the point of the load application P and δ.

5.2.4 Determination of the Delamination Length

Unlike the Mode I experiments, no camera or recording device was used to measure the delamination length during the tests. A compliance calibration (CC) was performed for the specimens, before testing them, to obtain the relationship between the specimens' compliance (δ/P) and their delamination length a. δ is the vertical displacement due to the applied load P. The compliance calibration relationship obtained was then used to estimate the delamination length during the tests.

5.2.5 Load Versus Opening Displacement Record

The displacement was estimated as the vertical displacement of the loading roller. The internal X-Y plotter of the loading test device was used as a permanent record during the test. Also the load vs. displacement data was digitally extracted from the loading test device through LabVIEW to compute the compliance values.

5.2.6 Material and Test Specimens

Twenty-two plies, zero-degree unidirectional specimens, following the specimens used in [26], were used. 7 in long by 1 in wide specimens made of carbon reinforced unidirectional fiber T700S manufactured by TORAYCA, were built. Actual specimen dimensions were measured at three different locations and the average values shown. A 13 μm thick and 3 in long Teflon film was inserted between the eleventh and twelfth plies which corresponds to a value of a_0 of 1.5 in, to build the specimen. The specimens' both edges were coated with white or yellow spray paint to easily detect the onset of the delamination from the insert.

5.2.7 Static Mode II Fracture Characterization

The aim of the static tests ~~was~~ were to determine the value of G_{II}^{c} and also to determine the compliance calibration relationship between compliance and delamination length values. All tests performed for the static characterization of the laminates were carried out on the MTS machine, 100 KN maximum capacity with a 50 KN load cell, following [26]. Six specimens were tested in fracture Mode II and the values of G_{II}^{c} are obtained.

5.2.7.1 *Fracture Toughness Tests*

The specimens were marked with tick black marks at their middle and then at + 6/16 in and - 6/16 in. away from the mark in the middle. Those marks were used as guides for positioning the center load nose during compliance calibration loadings. The compliance calibration along with the fracture tests consisted of three loading sets. At first the specimens were put in the three-point bending fixture with the center load above the + 6/16 in. mark and loaded with a maximum load below the failure load value. Then the specimens were shifted to have the center load nose above the – 6/16 in. mark, and loaded again with the same maximum load value. The load-displacement data of the specimens at those two positions were obtained to determine the two compliance values. The specimens were finally put in the three-point bending fixture at the testing position with the center load nose at the middle mark position (Figure 5.3) and loaded until the initial delamination grew away from the insert and then unloaded. The load-displacement of the specimens was also obtained during the loading and unloading period. The last load-displacement data point right before the initial delamination started growing was used to compute the third calibration value for the compliance calibration. The first load-displacement data point right after the specimen unloading began was used with the compliance calibration to obtain the precrack length (delamination length after the delamination grew from the insert). During the fracture tests the delamination grew about 0.5 in from the insert end to the middle mark on the specimens. Photos taken after unloading the specimens gave a visual estimation of the delamination length on the two edges of the specimens. The tic marks used for the compliance calibration also can be seen in Figure 5.4.

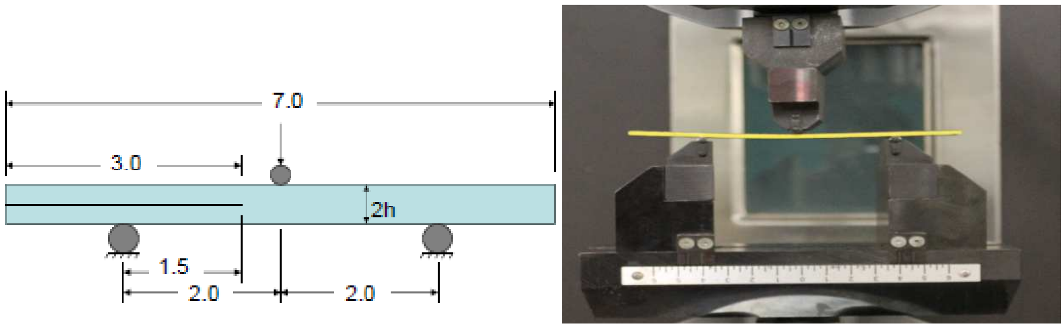

Figure 5.3. Static ENF Fracture Test Configuration (dimensions are in inches).

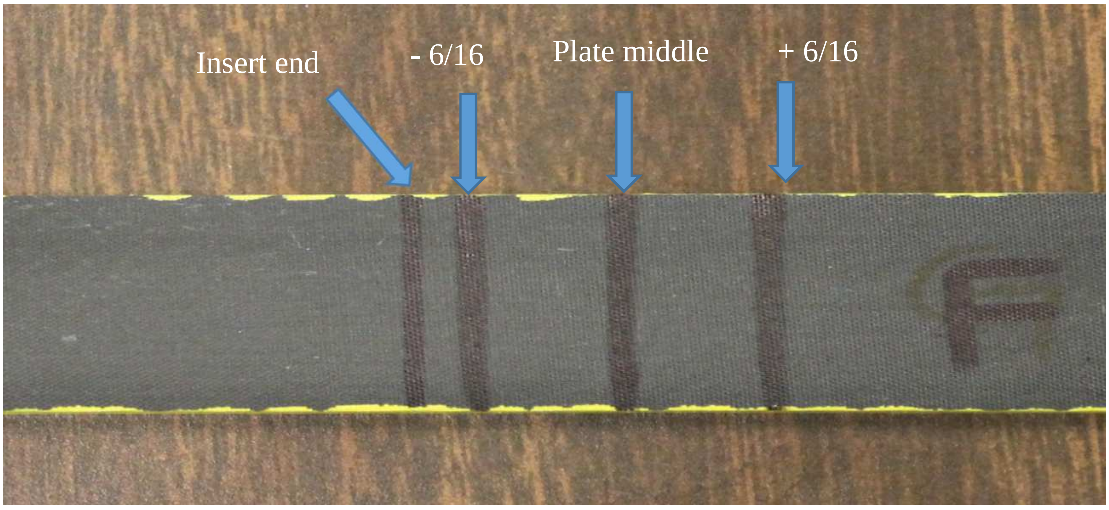

Figure 5.4. Specimen Top Surface Showing the Positions for the Compliance Calibration.

5.2.8 Fatigue Testing Characterization of the Specimens

The ENF fatigue tests were performed to determine the Kardomateas constants (m_{II} and C_{II}) in Mode II. To do so the delamination growth had to be studied. All the fatigue tests were performed also on the same MTS machine as the static tests. Six specimens with the same dimensions, the same material and the same initial delamination properties as the static tests specimens were used for the fatigue tests as shown in Figure 5.3. The fatigue testing machine was operated in load control mode with a constant load amplitude. The specimens were cycled between a minimum displacement load P_{min} and maximum load P_{max} such that the value of the load ratio P_{min}/P_{max} was set to 0.1. The maximum load P_{max} corresponding to G_{IImax} values equal to 60 %, 40% and 20% of the average value of G_{IIC} from the fracture tests were chosen. For each of the three values of P_{max} two specimens were fatigue tested. The specimens were subjected to a sinusoidal cyclic loading at a frequency of 8 Hz. Before the fatigue tests a compliance calibration (following the same procedure as in the fracture tests) was conducted to determine the relationship between compliance and crack length and to calculate the appropriate P_{max} for each of the two specimens being tested at the same G_{IImax} value. For all three delamination lengths used to obtain this compliance calibration, the load was kept below a level that would cause further delamination growth. During fatigue, the compliance (load-displacement data) was measure at a frequency of 4 Hz until the tests were stopped. The compliance values were used with the compliance calibration to calculate the corresponding delamination lengths. The fatigue tests were conducted for almost 1 million cycles.

5.2.8.1 Data Reduction

As in the Mode I fracture case, data reduction was conducted to obtain the Mode II fracture toughness G_{II}^{c} of the specimens. Here only the compliance calibration method was used. Also as said before for the Mode II the compliance calibration was not only used during the static testing but also during the fatigue testing, to determine the crack lengths.

5.2.8.2 Compliance Calibration

As said above three loadings were used to determine the compliance - crack length data points, at $a_0 - 6/16$, $a_0 + 6/16$ and from the initial portion of the fracture test. a_0 is the specimens initial delamination.

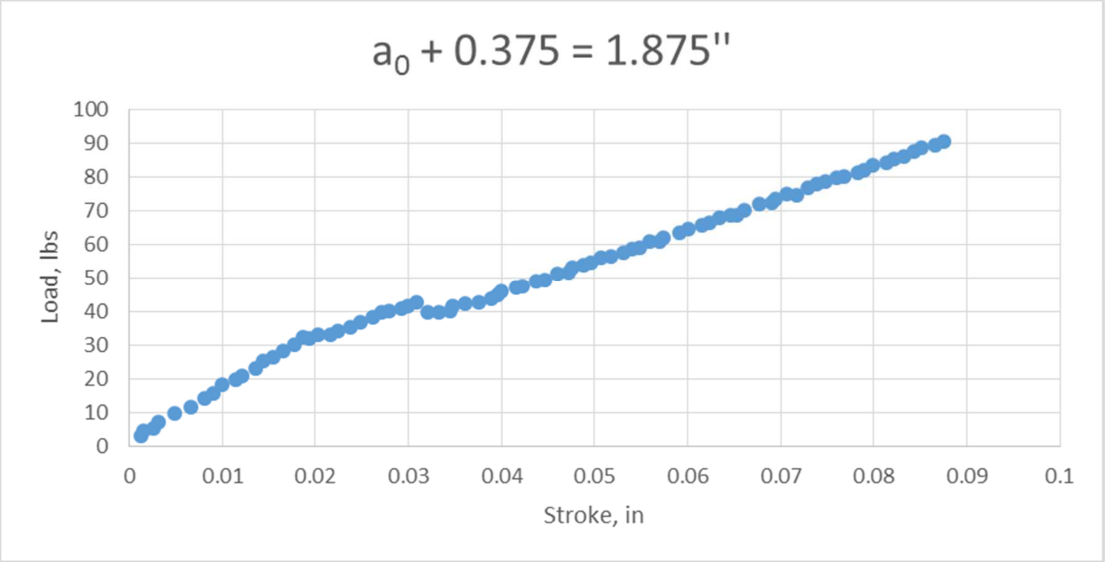

Figure 5.5a. Typical Compliance Calibration Load-Displacement Graph at - 6/16.

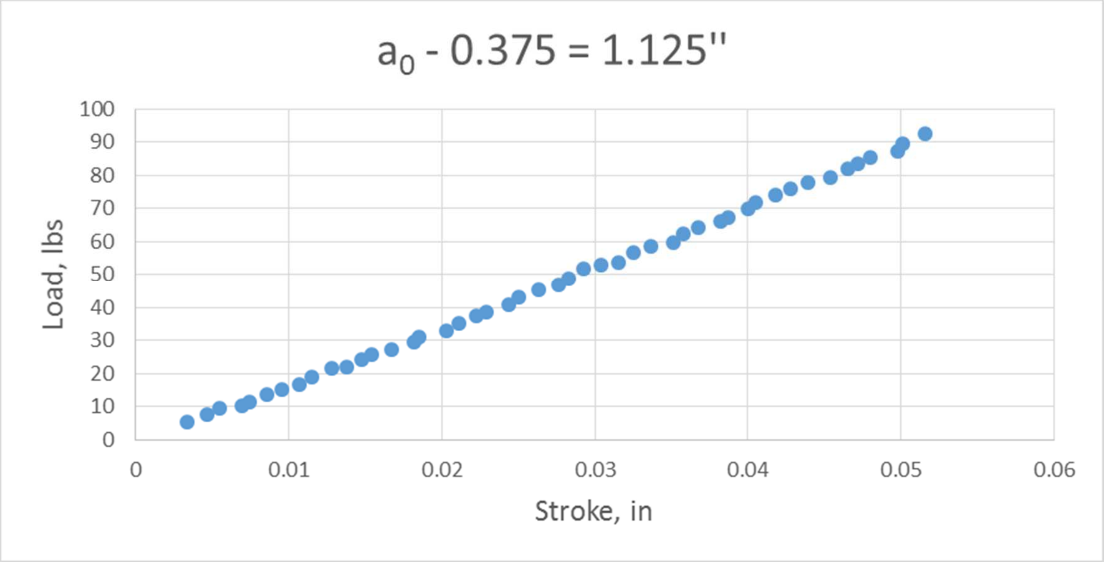

Figure 5.5b. Typical Compliance Calibration Load-Displacement Graph at + 6/16.

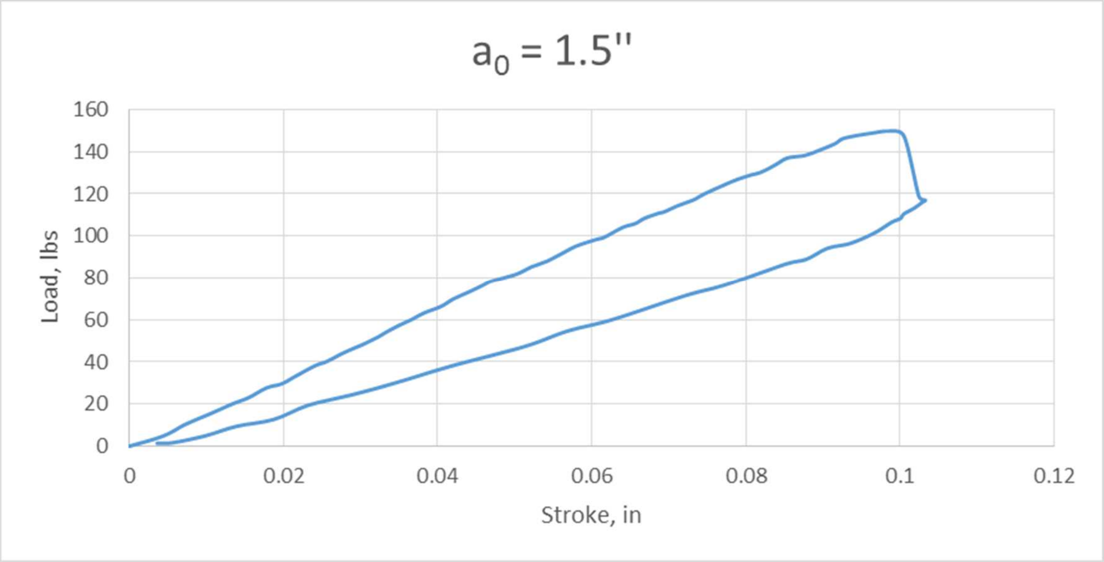

Figure 5.6. Typical Fracture Test Load-Displacement Graph for Determination of G_{II}^{c}.

Figures 5.5a and 5.5b show typical compliance calibration load-displacement graphs from the fracture tests and Figure 6 shows a typical ENF load-displacement plot from the fracture test for the determination of G_{II}^{c}.

The compliance was determined using the load-displacement data. The compliance versus crack length data point were fitted to the following equation

$$C = A_2 + A_1 a^3 \tag{5.7}$$

The coefficients A_2 and A_1 were determined using a least-squares linear regression method of C at each crack length as a function of the cubed crack length. With those coefficients the crack length corresponding to any compliance value (δ vs P data points) can be determined using

$$a = \left(\frac{C - A_2}{A_1}\right)^{1/3} \tag{5.8}$$

A typical fracture test fit of compliance as a function of crack length is shown in Figure 5.7.

The energy release rate $G_{II}$was determined using the compliance calibration relation specified in [26]:

$$G_{II} = \frac{P^2}{2B}\frac{\partial C}{\partial a} \tag{5.9}$$

Which gives us the equation below when C is replaced by Eq. 5.6.

$$G_{II} = \frac{3A_1 P^2 a^2}{2B} \tag{5.10}$$

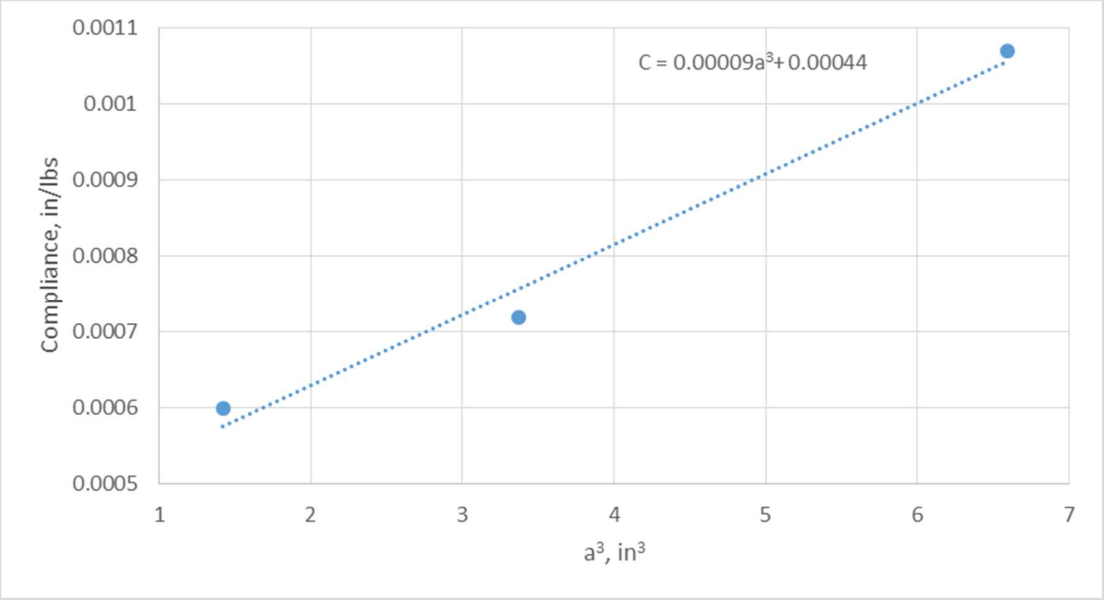

Figure 5.7. Typical Fit of Compliance as a Function of Crack Length Cubed.

5.2.8.3 Fracture Toughness Calculations

The Mode II fracture toughness G_{IIc} for the specimen was determined using Eq. 5.10:

$$\mathrm{G}_{\mathrm{II}}^{\mathrm{c}} = \frac{3mP_{max}{}^{2}a^{2}}{2B} \tag{5.11}$$

Where P_{max} is the maximum load from the respective fracture test and a is the initial half crack length (first crack length measured from the insert tip).

5.2.84 *Fatigue Test Property Calculations*

The maximum load P_{max} corresponding to G_{IImax} values equal to 60 %, 35% and 20% of the average value of G_{IIC} from the pre-cracked fracture tests were chosen. P_{max} was obtained by solving Eq. 5.11 and substituting the corresponding value of G_{IImax},

$$P_{max} = \frac{1}{a_0}\left(\frac{2BG_{IImax}}{3m}\right) \tag{5.12}$$

For the calculation of the crack growth rate, the values of the crack length at a specific number of cycles was needed. Since the data acquisition system used during the fatigue test only produced (δ, P) data points at every specific number of cycles, those data points were first converted into crack length, using Eq. 5.8. Figure 5.8 shows the fracture surface of a typical ENF fatigue specimen.

The compliance data was recorded at every 4 cycles to ensure that no data were lost. The data were then used to calculate the fatigue crack growth rate using the incremental polynomial method with 7 successive points as explained for the Mode I fracture. Typical results for a fatigue crack growth curve is shown in Figure 5.9.

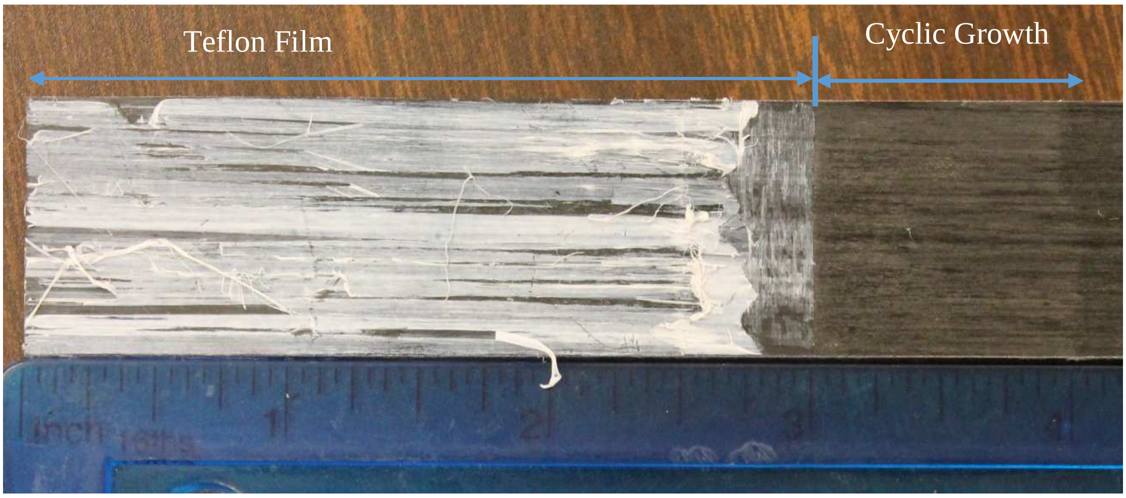

Figure 5.8. Fracture Surfaces of Typical ENF Fatigue Specimen.

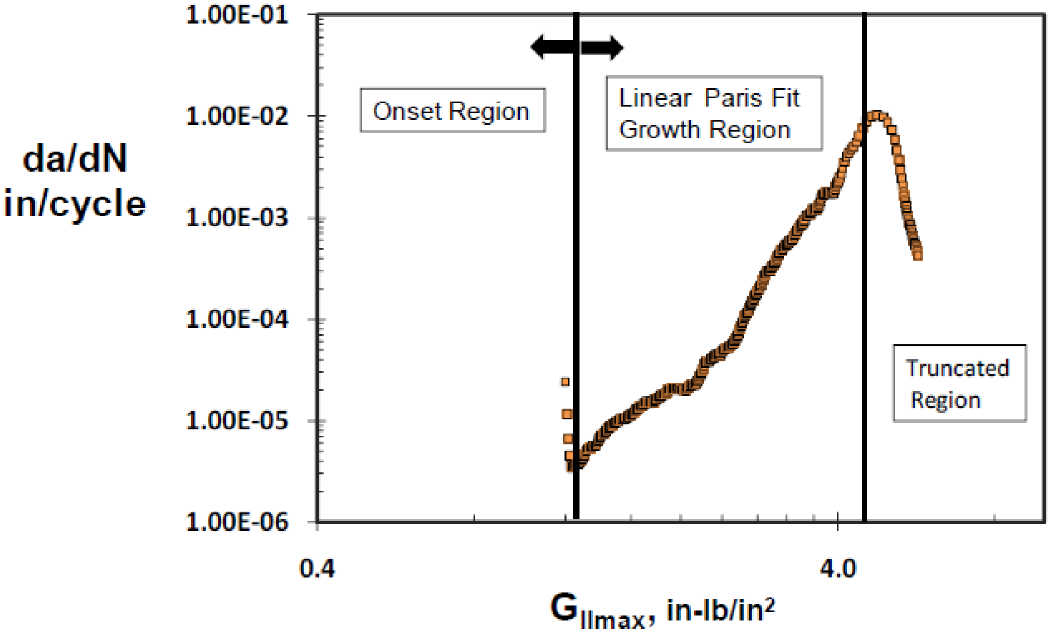

Figure 5.9. Reduced Fatigue Crack Growth Data with Onset and Growth Regions Shown [26].

Only the section of the graph that shows stable fatigue crack growth was used for our analysis (Figure 5.8). That section starts at the onset delamination length.

For each specimen the fatigue growth curve was plotted in the typical log-log form of the Kardomateas Law and the data were fitted to a relationship on the form of:

$$\frac{da}{dN} = \frac{C_{II}\tilde{G}_{IImax}{}^{m_{II}}}{1 - \tilde{G}_{IImax}} \tag{5.13}$$

$$\xrightarrow{yields} \left(1 - \tilde{G}_{\mathrm{IImax}}\right)\frac{da}{dN} = C_{II}\tilde{G}_{IImax}{}^{m_{II}} \tag{5.14}$$

where $\tilde{G}_{max} = G_{IImax}/\mathrm{G}_{\mathrm{II}}^{\mathrm{c}}$

The procedure explained in the previous section for Eq. 5.6 was used here with Eq. 5.14 to plot the delamination growth curves in the form of Eq. 5.14 and to determine the values (interval and mean) of m_{II} and C_{II}.

5.2.9 Fracture and Fatigue Test Results

Fracture toughness results for all the specimens tested are shown in Table 5.4.

Table 5.4 Mode II Interlaminar Fracture Toughness Values

Specimen ID	G_{II}^{c} (in-lb/in^2)
7	4.68
8	4.6
9	5.1
10	4.57
11	4.72
12	4.75
Average	4.73
Range of values	[4.57,5.10]

The different values of G_{IImax}, for the fatigue tests are shown on Figure 5.10. Those values were used to determine the values of P_{max} for the cyclic loading. The values of G_{IImax} for each of the fatigue tests and the number of cycles before the delamination onset for all of the specimens are plotted in Figure 5.10 as well as a power law curve fit.

Finally the delamination crack growth results were first plotted in the Paris Law form in Figure 5.11. Then the same delamination crack growth were plotted in the Kardomateas Law form in Figure 5.12. We can see that the plots are not the same and the parameters

C_{II} and m_{II} have different values for the two different laws. Also a power law fit curve was computed for all of the fatigue specimen crack growths on the same graph

(Figure 5.12) to get the mean value of C_{II} and m_{II}.

It should be noticed that Figures 5.11 and 5.12 depict the delamination growth laws derived by combining the results of all of the three different cyclic loads (60%, 40% and 20 %) into one plot.

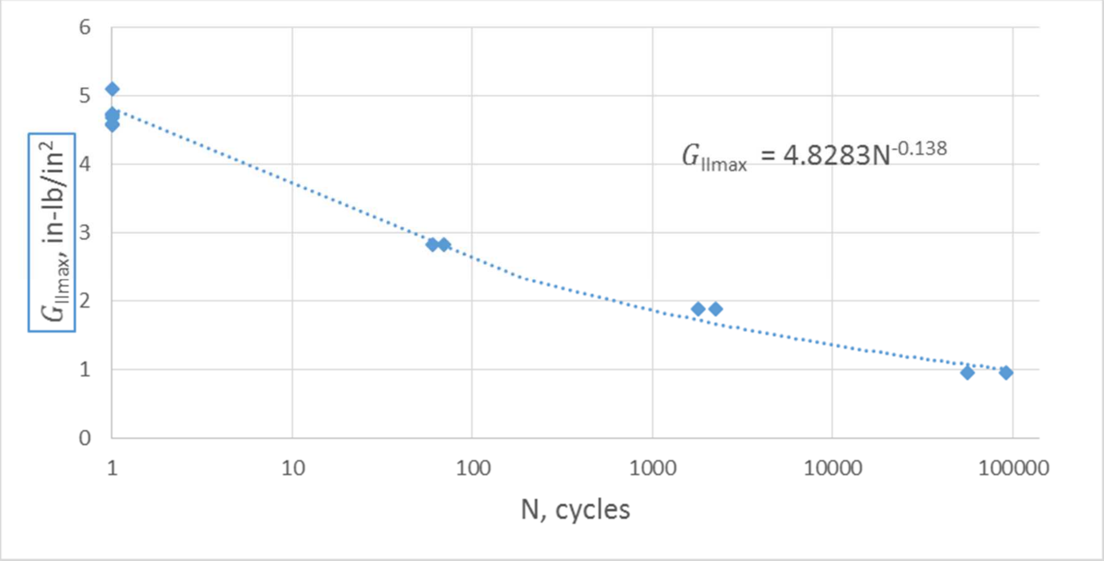

Figure 5.10. Power Law Fits Applied to the Delamination Onset Threshold Data.

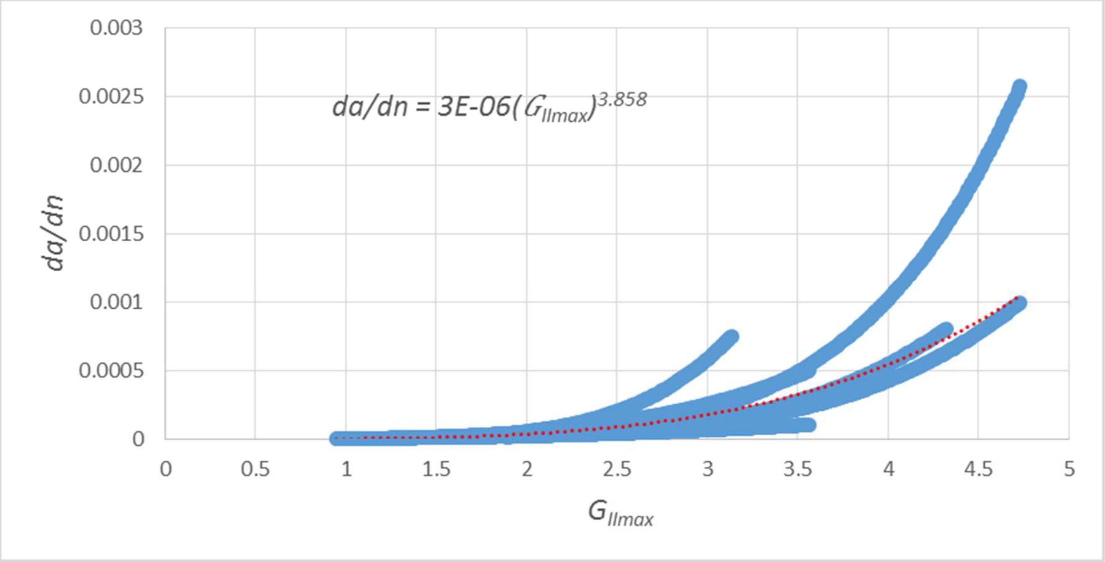

Figure 5.11. Paris Law Fits Applied to All Six Specimen Delamination Growth Data.

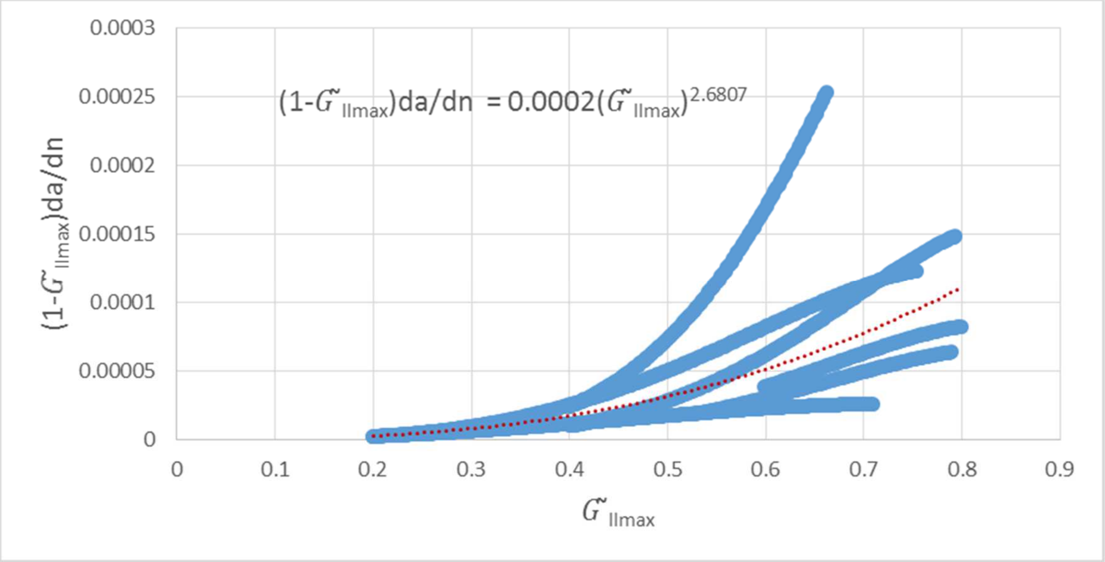

Figure 5.12. Kardomateas Law Fits Applied to All Six Specimen Delamination Growth Data.

Table 5.5 Kardomateas Mode II Coefficient and Exponent Values

Specimen ID/color	C_{II}	m_{II}
F7 /yellow	0.0018	4.6735
F8/green	0.0004	3.0565
F9/gray	0.0004	3.9605
F10/orange	0.0002	2.6947
F11/blue	0.0001	2.9145
F12/dark blue	0.00006	1.8265
Mean (Fit)	0.0002	2.6807
Range	[0.00006,0.0018]	[1.8265,4.6735]

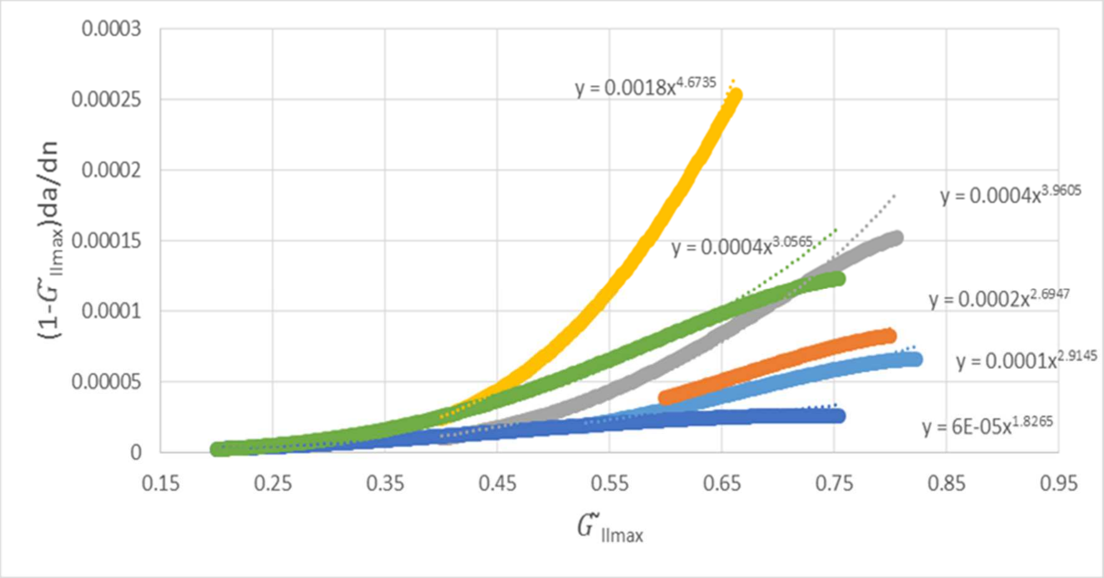

Figure 5.13. Kardomateas Law Fits Applied to Each of the Six Specimen Delamination Growth Data.

Figure 5.13 shows each specimen with both its Kardomateas growth curve as well as its power fit curve.

Table 5.5 shows the values of C_{II} and m_{II} obtained for each of the fatigue specimens with the power fit curves as well as their mean value and interval range. Each specimen ID is also linked to its color on the graph.

Table 5.6 shows a summary of all the uncertain parameters range of values and mean values.

Table 5.6 Kardomateas Law Uncertain Parameter Values

Parameters	Range	Mean value
C_I	[0.00001,0.00015]	0.00002
C_{II}	[0.00006,0.0018]	0.0002
m_I	[5.23,9.21]	5.42
m_{II}	[1.8265,4.6735]	2.6807
$\mathrm{G}_\mathrm{I}^\mathrm{c}$	[1.02,1.11]	1.0575
$\mathrm{G}_\mathrm{II}^\mathrm{c}$	[4.57,5.10]	4.73

Chapter 6

Mixed-Mode I and II Experiments and Comparison between Affine Arithmetic Predictions and Monte Carlo Predictions

In the previous section all of the uncertain parameters range values and mean values were obtained and summarized in Table 5.6. This section will present how these parameter values were used to predict the delamination length.

6.1 Determination of the Theoretical Unstable-to-Stable Half Length

The theory described in Chapter IV will now be applied to some specimens, consisting of a delaminated plate made of the same composite material as in the previous chapter. This step in necessary to obtain information that will be used in the mixed mode experiments such as the unstable-to-stable transition point l_{tr}. The half-length of the plates are L = 2.5 in with a width of 0.48 in. The toughness data used were the average values in Table 5.6. First, we need to determine the theoretical value of the unstable-to-stable growth transition point, l_{tr}, by examining the $\tilde{G}_{max}$ vs l curves (which would have a zero slope or peak value at this point). If the initial delamination half-length in the plate is below l_{tr}, then unstable but contained growth will occur once the delamination grows to the length corresponding to Γ_0. Figure 6.1 shows the maximum energy release rate $\tilde{G}_{max}$ as a function of the delamination half-length ratio l/L, for the applied strain peak value that will be used in the experiments : $\mathcal{E}_{max} = 2.5 \times 10^{-3}$ and the three cases of delamination location : $h/T = 0.25$, $h/T = 0.40$ and $h/T = 0.50$.

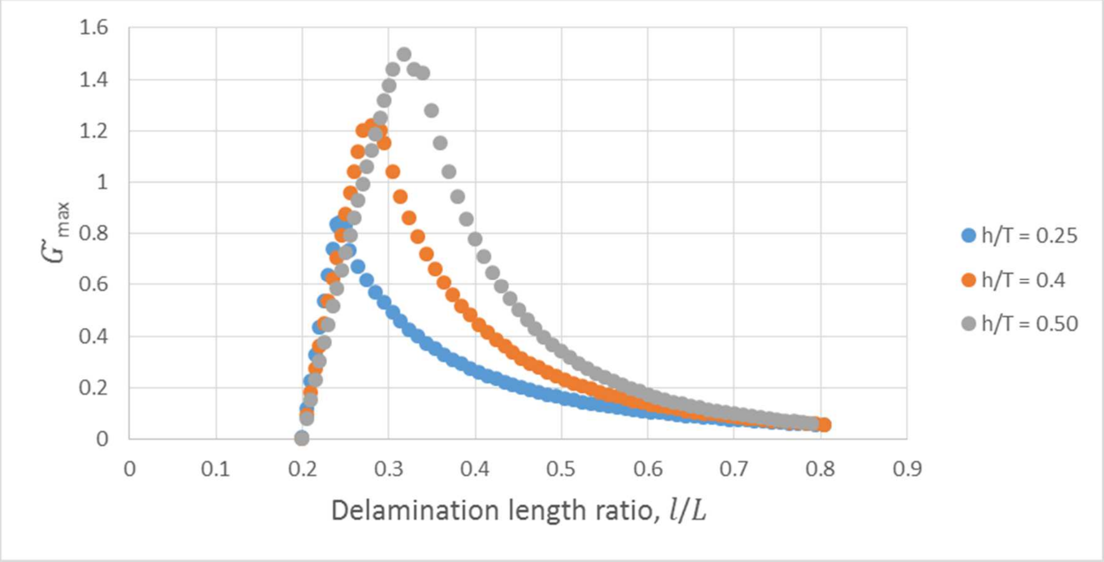

Figure 6.1. Maximum Energy Release Rate $\tilde{G}_{max}$ as a Function of Delamination Ratio, in Order to Determine l_{tr}.

In Figure 6.1 it is seen that for a delamination half-length $l_0 = 0.125\ in$, which correspond to a ratio $l/L = 0.45$, we are already at a point beyond l_{tr} and beyond the critical length ($\tilde{G}_{max} = 1$) for all of the three different specimens. Therefore slow fatigue growth is expected. The initial delamination half-length in all of the three different specimens tested was set to $l_0 = 0.125\ in$. In figure 6.2 we can see the maximum energy release rate as a function of the delamination half-length ratio for the specimen tested. Only the part of Figure 6.1 starting by the ratio $l/L = 0.45$ was used. Figure 6.3 shows the theoretical number of compressive cycles (strain between 0 and $\mathcal{E}_{max}$) expected to reach a certain delamination half-length using the Kardomateas law. We can see that for the same initial delamination half-length, the lower the ratio h/T is, the more growth resistant the specimen is. Moreover in the case of the same specimen thickness (specimens $\frac{8}{16}$ and $\frac{4}{16}$), we see that the closer to the surface that the delamination is, the more resistant the specimen is.

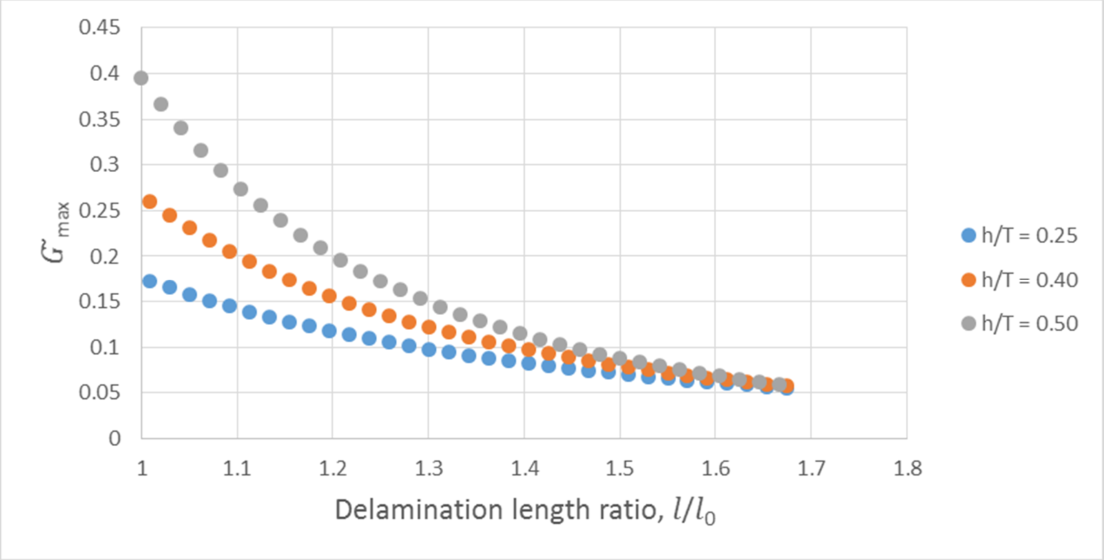

Figure 6.2. Maximum Energy Release Rate $\tilde{G}_{max}$ as a Function of Delamination Ratio.

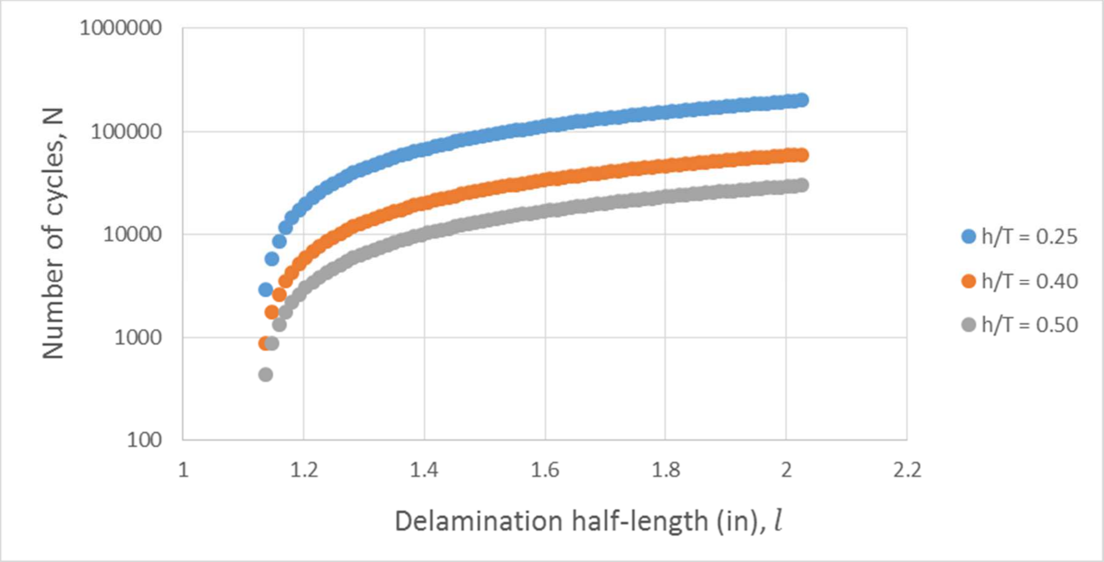

Figure 6.3. Number of Compressive Cycles as a Function of the Delamination Ratio (semi logarithmic plot).

6.2 Prediction Using Affine Arithmetic

Once the initial delamination half-length necessary to have slow and stable growth was determined, all the characteristics of the specimens were known. The prediction of the delamination half-length was done using the Affine Arithmetic equations for lower and upper limits of the different functions of the Kardomateas Law. The range values of the Kardomateas uncertain parameters, from the characterization of Mode I and Mode II were used here. Figures 6.4a, 6.4b and 6.4c depict the curves of the lower limit values of the delamination half-length range for every cycle as well as the corresponding upper limit values for each of the different specimens tested. The lower limits correspond to the worst combination of the uncertain parameters (the minimum number of cycles it will take for the delamination to reach a certain half-length a) , while the upper limits corresponds to the best combination of the uncertain parameters (the maximum number of cycles before the delamination reach a certain half-length a).

Figure 6.4 (a, b and c) shows that the prediction of the Kardomateas Law using the average values of the uncertain parameters is always contained inside the prediction made using the range of values of these uncertain parameters. That is always a good sign when a prediction method is being studied.

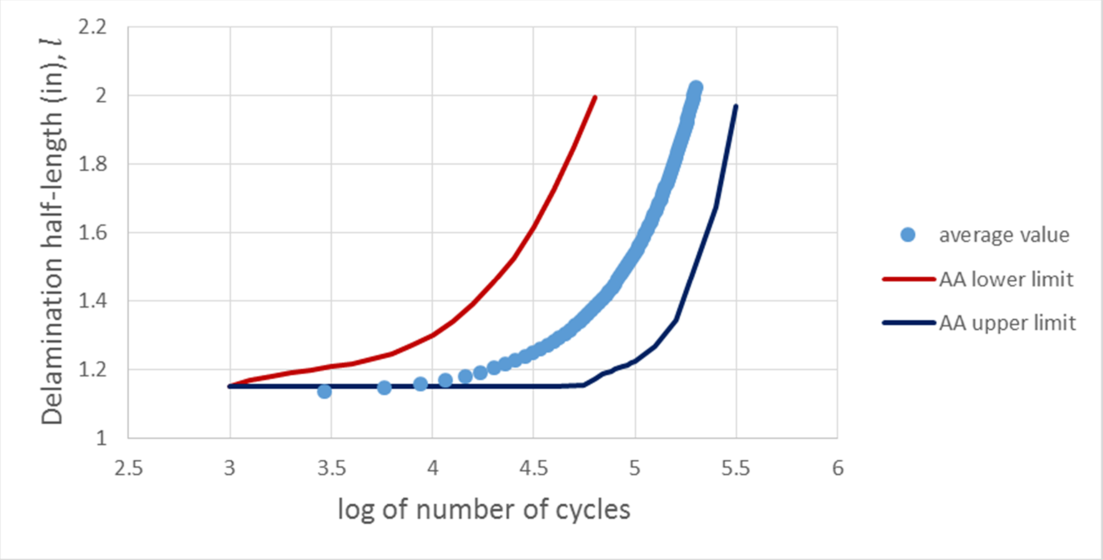

Figure 6.4a. Comparison of Delamination Growth Curves by Affine Arithmetic and by the Average Value for Specimen h/T = 0.25.

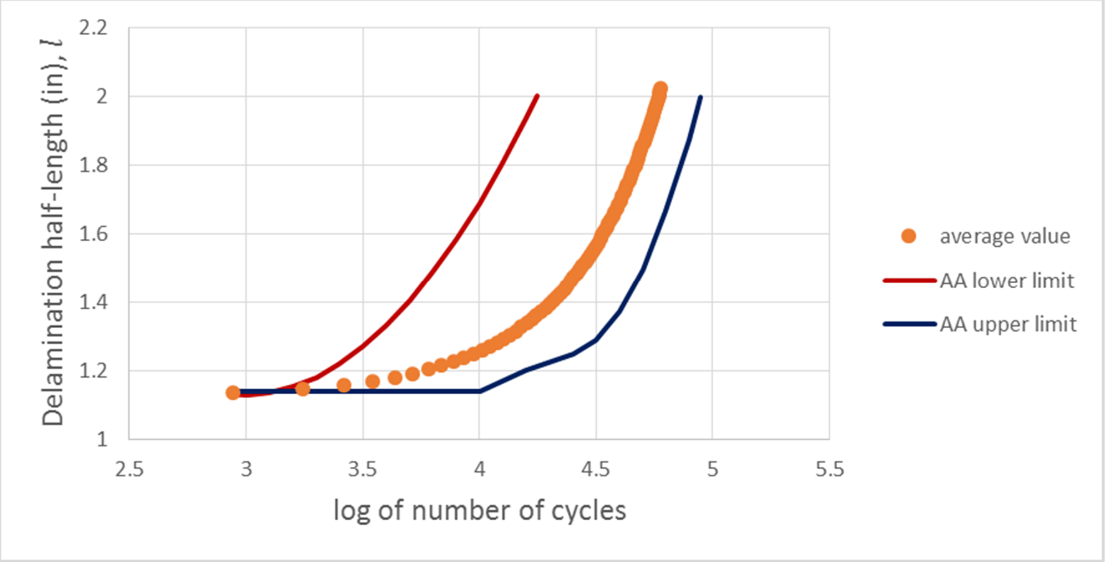

Figure 6.4b. Comparison of Delamination Growth Curves by Affine Arithmetic and by the Average Value for Specimen h/T = 0.40.

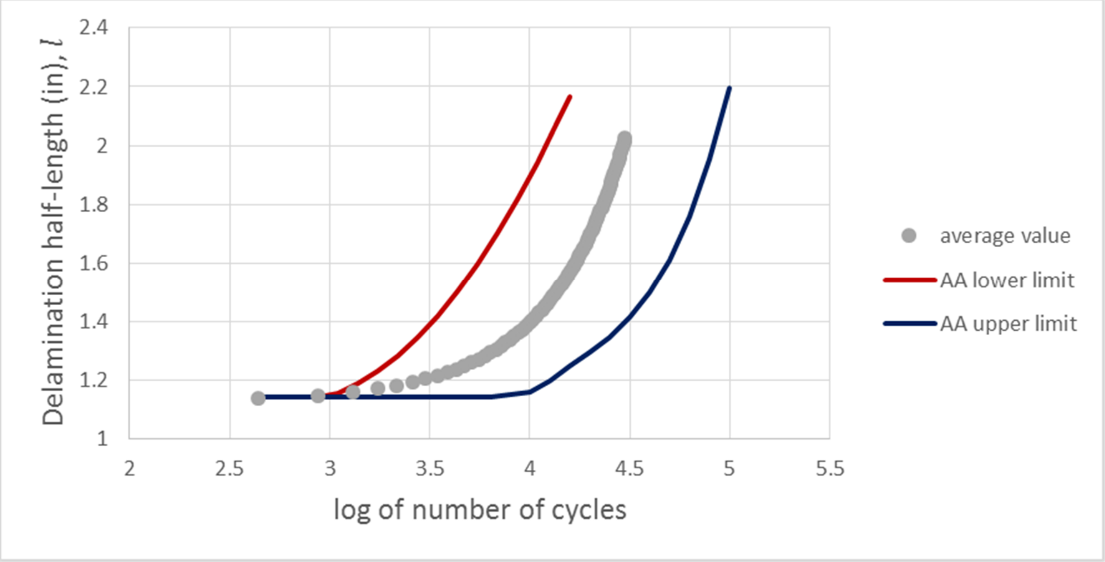

Figure 6.4c. Comparison of Delamination Growth Curves by Affine Arithmetic and by the Average Value for Specimen /T = 0.50.

6.3 Prediction Using Monte Carlo Analysis

Since Monte Carlo analysis is the most used uncertainty propagation method, the prediction made with Affine Arithmetic is compared with the one made using the Monte Carlo Analysis. Monte Carlo simulation is mainly defined by the number of samples chosen for the computation. The number of samples are the number of data points randomly chosen in the range of values of the uncertain parameters for the computation of the prediction half-length. The higher that number is, the more accurate the prediction will be; however a higher number of samples is usually followed by a longer computation time.

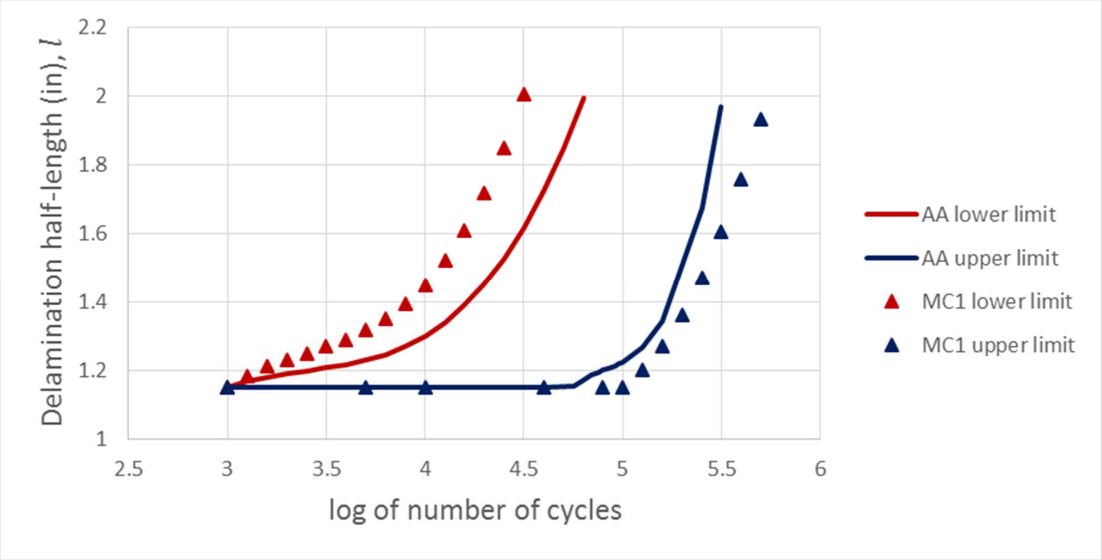

Figure 6.5. Comparison of Delamination Growth Curves Between Monte Carlo 1 and Affine Arithmetic for Specimen h/T = 0.25.

Two Monte Carlo simulations are computed for the prediction. The first one with 2000 samples is compared to the prediction of Affine Arithmetic in Figure 6.5. Then the second Monte Carlo simulation with 6000 samples was compared against the Affine Arithmetic prediction (see Figure 6.6) to see the difference in terms of prediction accuracy.

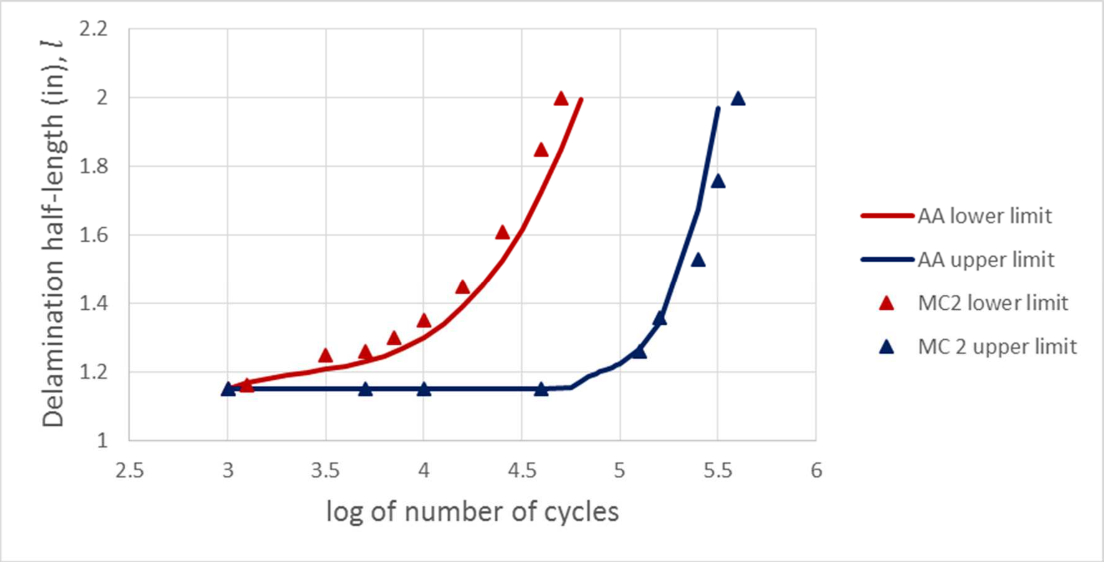

Figure 6.6. Comparison of Delamination Growth Curves Between Monte Carlo 2 and Affine Arithmetic for Specimen h/T = 0.25.

Table 6.1 shows the lifetime prediction yields by each of the simulations and their computation times. We can see that the Monte Carlo 1 simulation predicts the worst case for failure; namely, 1 day before the failure is supposed to occur (compared to the Affine Arithmetic prediction).

Table 6.1 Comparison of Lifetime Prediction and Computation Times Between Affine Arithmetic and Two Monte Carlo Simulations for Delamination for h/T = 0.25

Uncertainty propagation method	Affine Arithmetic	Monte Carlo 1	Monte Carlo 2
Number of samples	-	2000	6000
Computation time (sec)	40	250	1586
Log (n)	[4.8, 5.5]	[4.5, 5.7]	[4.7, 5.6]
Number of days for 8 Hz load frequency	[2.19, 10.98]	[1.10, 17.40]	[1.73, 13.82]

Simply increasing the number of samples to 6000 helps the Monte Carlo 2 to make a more accurate prediction but requires a longer computation time. It should be noted that the computation times of the Monte Carlo simulations are relatively small in the case of the composite materials compared to the Paris Law case for isotropic material. In addition, the lifetime range predicted in the composite case has a small width, i.e. 2 days to 10 days, which is really useful in practice. It should be noted that the Kardomateas coefficients and exponents were considered here independent as explained in the Affine derivation. But as we have seen while computing the delamination growth curve for every specimen the coefficient *C* and the exponent *m* are linked through the Kardomateas Law and hence are not independent. Taking into account the dependence of those two parameters would yield a tighter prediction range.

6.4 Experimental Results

The experimental study was conducted on the same carbon fiber material as for the Mode I and Mode II characterization tests. Test specimens were laid up by hand and cured in an Autoclave oven at a temperature of 270 F (vacuum bag was placed prior to the curing cycle). The initial delamination half-length of 1.125 in. was produced by placing at the desired location, through the entire width, a Teflon film of 0.001 in thickness. After curing, the thicknesses of the specimens were measured with a micrometer at three different points through the width and length to insure overall uniformity.

The cyclic compression tests were conducted on the specimens at a frequency of 8 Hz, and the delamination growth was monitored using a Thermal Image Capability and visual measurements. All the experiments were conducted at a constant maximum compressive strain $\mathcal{E}_{max}$. The specimens had a width of 0.48 in. and a half-length between grips of L = 2.5 in.

Three delamination configurations were tested:

(a) 16 plies, specimen thickness T = 0.112 in, delamination between the fourth and fifth layer, hence h/T = 4/16 = 0.25. This specimen is denoted 4/16

(b) 16 plies, specimen thickness T = 0.113 in, delamination between the eighth and ninth layer, hence h/T = 8/16 = 0.5. This specimen is denoted 8/16

(c) 10 plies, specimen thickness T = 0.074 in, delamination between the fourth and fifth layer, hence h/T = 4/10 = 0.4. This specimen is denoted 4/10.

Figures 6.7a, b and c show the actual experimental data against the prediction of Affine Arithmetic. It should be first emphasized that since the experimental delamination lengths were measured using the visual method and Thermal Imaging Capability, only measurements of delamination lengths at discrete points (at some specific number of cycles) were performed. At every length measurement, the fatigue test was stopped and the specimen taken out of the MTS machine before the measurements. Therefore the experimental data are given as discrete data points while the Affine Arithmetic prediction is given as curves. Table 6.2 shows a detailed record of the experimental data.

Table 6.2. Experimental Data for Delamination Half-Length

h/T Specimen type	Number of cycles	l, inches Delamination half-length
4/16 (0.25)	1000	1.15
T = 0.112	10000	1.3
	50000	1.5
	100000	2
4/10 (0.40)	1000	1.14
T = 0.074	10000	1.5
	50000	1.8
8/16 (0.50)	1000	1.15
T = 0.113	10000	1.5
	30000	2.2

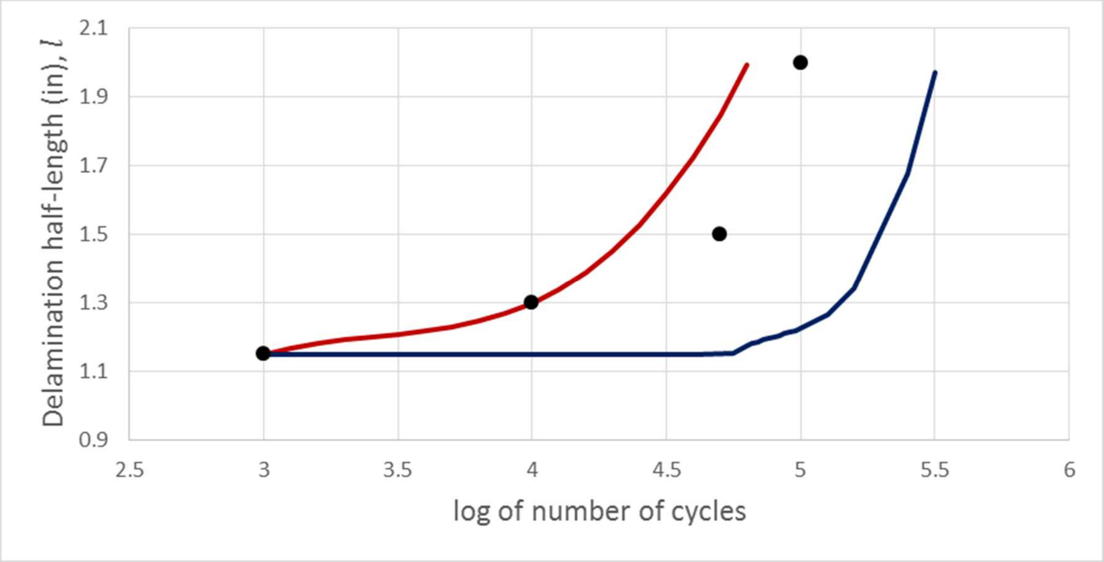

Figure 6.7a. Comparison of Experimental Data and Affine Arithmetic Prediction for *h/T* = 0.25.

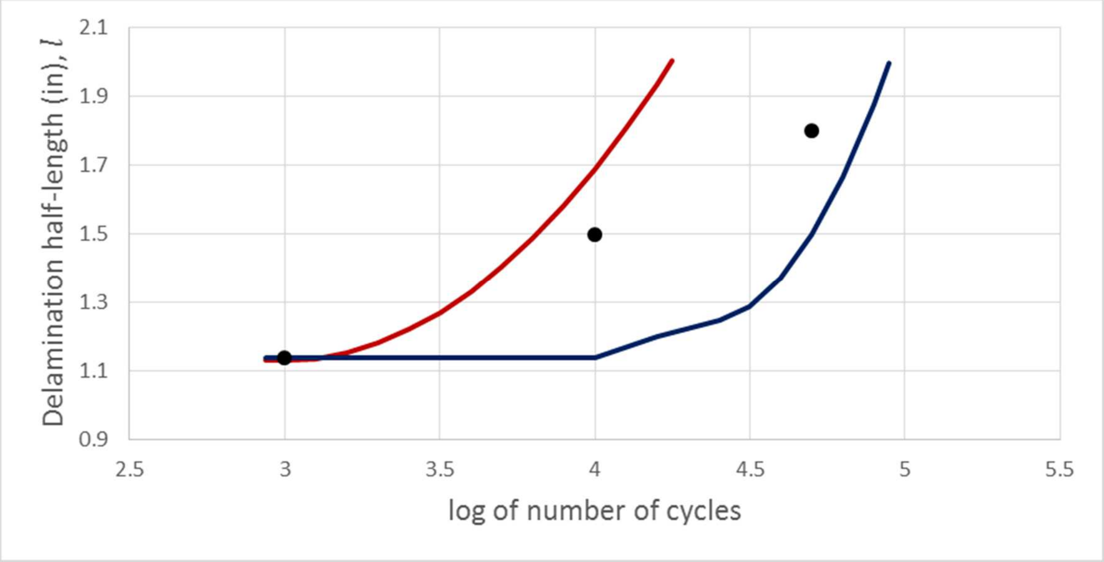

Figure 6.7b. Comparison of Experimental Data and Affine Arithmetic Prediction for *h/T* = 0.40.

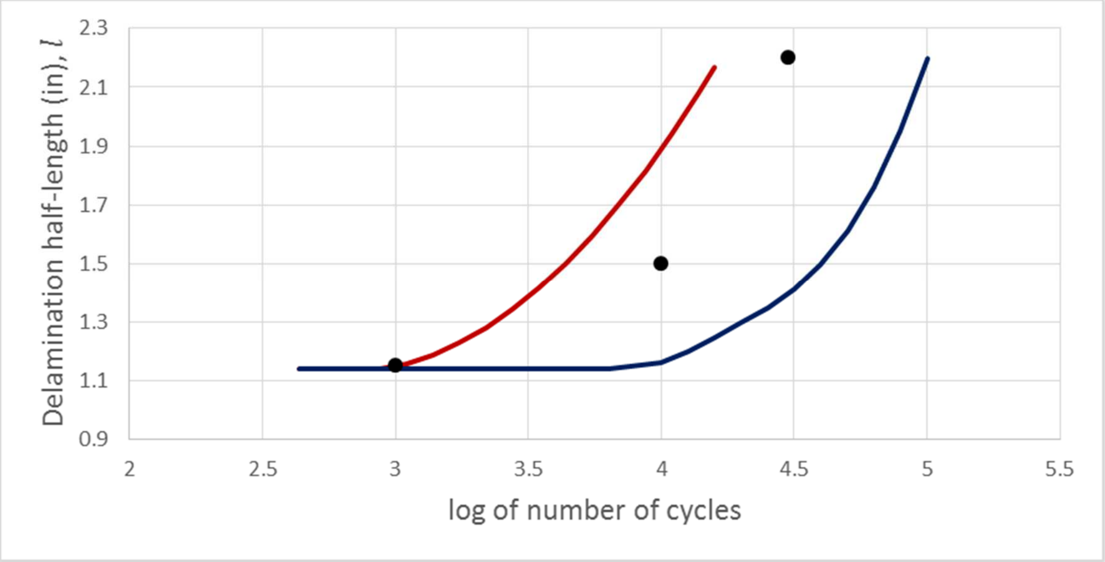

Figure 6.7c. Comparison of Experimental Data and Affine Arithmetic Prediction for *h/T* = 0.50.

We can see that in Figure 6.7 that all the experimental data points are inside the range of values predicted by Affine Arithmetic which shows that the prediction is correct.

In Figure 6.8 we can see the display of the specimens Thermal Imaging Capability. We were able to see distinctively the different part of the tested material using Thermal Imaging. It was also very helpful to measure the displayed delamination and to compare with the visual measurements. An example of visual measurements is also shown in Figure 6.9. In Figure 6.10 different stages of the delamination growth can be seen using Thermal Imaging. Figure 6.11 shows a front and side view of a specimen during the mixed-mode I and II fatigue test.

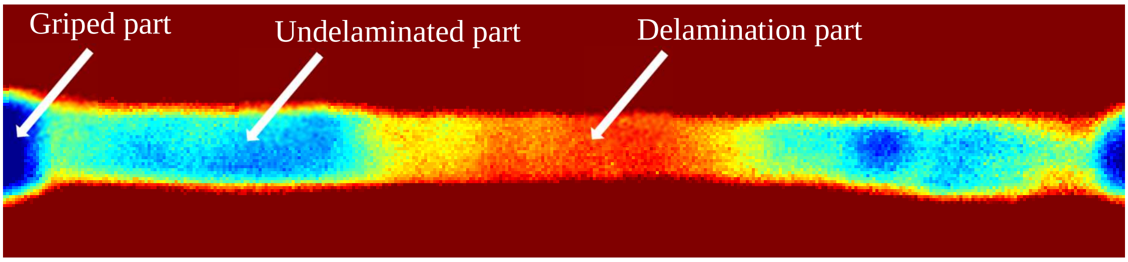

Figure 6.8 Delaminated Specimens Display Through Thermal Imaging.

Figure 6.9 Delaminated Specimen Using Visual Measurement.

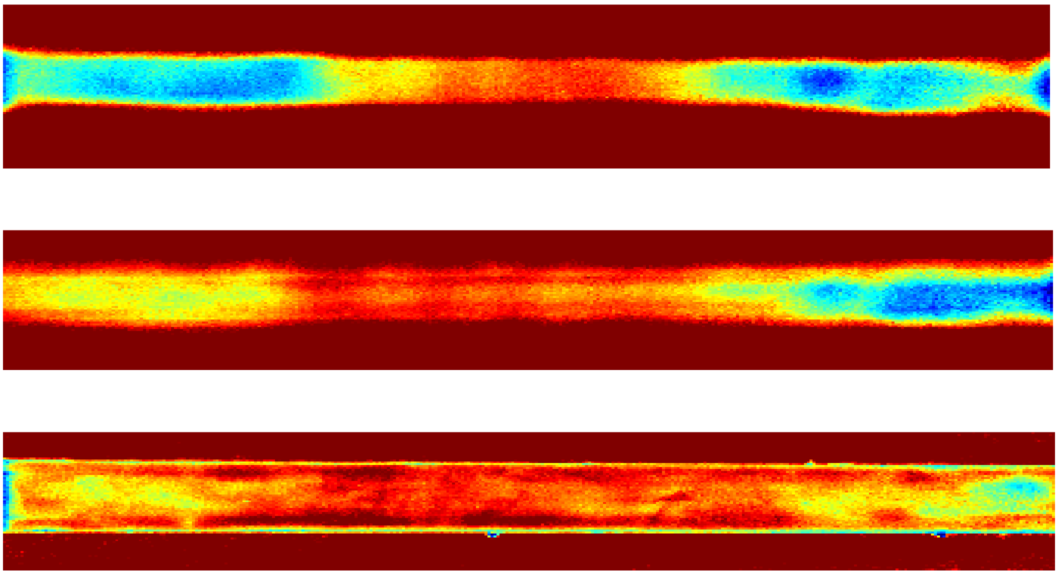

Figure 6.10 Delamination Growing from Insert to the Grips.

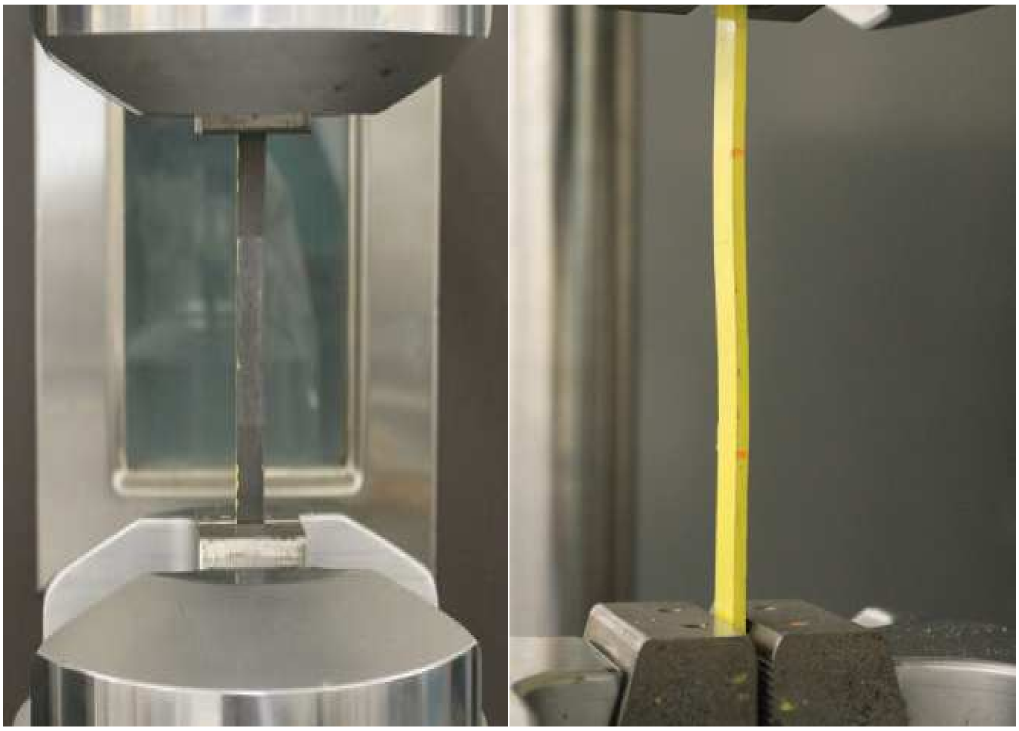

Figure 6.11 Specimen During Mixed-Modes I and II Fatigue Test.

Chapter 7

Conclusion and Future Work

In this study, an uncertainty algorithm called Affine Arithmetic was used to predict the delamination half-length and lifetime of composite specimens made of carbon fiber. The Kardomateas Law was used as the crack growth law and the derivations necessary to compute the range values of the lifetime were shown. Predictions were made using the uncertain parameters range of values instead of the probability distribution. The study showed every step necessary for the prediction of damage in SHM, starting with the derivation of the Affine Arithmetic forms, the determination of the different uncertainty parameters in Mode I and Mode II of fracture, the measurement of the mixed-mode I and II delamination length using Thermal Imaging and finally the comparison of Affine Arithmetic predictions with different Monte Carlo simulations.

Affine Arithmetic was found very accurate in its predictions and converges very quickly compared to the Monte Carlo simulations. However, the dependency between the coefficient and the exponent in Mode I as well as their dependency in Mode II was not taken in account in this study. To be sure that Affine Arithmetic predicts tight bounds for the lifetime of the specimens, more specimens should be studied on a longer number of cycles.

It would be interesting as a continuation of this research to take the dependency of these two parameters (between, on the first hand C_I and m_I and on the second hand dependency between C_{II} and m_{II}) into account and see the effects on the prediction accuracy and computation time.

Only three specimens were studied in this case for the prediction and not too many specimens were tested in Mode I and Mode II of fracture for the determination of the uncertain parameters range of values. A study focusing principally on the determination of those uncertain parameters range of values would definitely increase the accuracy of the Affine Arithmetic prediction.

Other damage mechanisms, such as, damage due to impact loading, damage due to cyclic compression – tension loading, could also be studied using Affine Arithmetic, as long as one is willing to derive the necessary equations.

References

[1] M. A. Schwabacher, “Survey of Data-Driven prognostics,” AIAA Infotech@Aerospace Conference,Arlington,Virginia,2005.

[2] J. Luo, K.R. Pattipati, L Qiao and S. Chigusa, “Model-Based Prognostic Techniques Applied to a Suspension system,” IEEE Transactions Systems Man, And Cybenetics-Part A, Vol. 38, No. 5, pp. 1156-1168, 2008.

[3] J. Yan and J. Lee, “Hybribrid Method for On-line Performance Assessment and Life Prediction in Drilling Operations,” IEEE International Conference on Automation and Logistics, Jinan, Shandong, China, 2007.

[4] M. Janssen, J. Zuidema, R. J. H. Wanhill, Fracture Mechanics in London Spon Press, 2004.

[5] You Ling and Sankara Mahadevan, “Integration of Structural Health Monitoring and Fatigue Damage Prognosis”, Mechanical Systems and Signal Processing, Vol 28,pp. 89-104, 2012.

[6] S. S. Kulkarni and J. D. Achenbach, “Structural Health Monitoring and Damage Prognosis in Fatigue,” Center for Quality Engineering and Failure Prevention,Northwestern University, Evanston, IL 60208, USA, 2008.

[7] M. Orchard and G. Vachtsevanos, “A Particle Filtering Approach for On-Line Failure Prognosis in Planetary Carrier Plate,” International Journal of Fuzzy Logic and Intelligent Systems, Vol. 7, No. 4, pp. 221-227, 2007.

[8] S. H. Leem, D. An, J. Choi, “Bayesian Parameter Estimation for Prognosis of Crack Growth under Variable Amplitude Loading,” Trans. Of the KSME(A), Vol. 35, No. 10, pp. 1299-1306, 2011.

[9] R. J. Cross, A. Makeev, E. Armanios, “A Comparison of Predictions From Probalistic Crack Growth Models Inferred From Virkler’s Data,” Journal of ASTM International, Vol. 3, No. 10, pp. 1-11, 2006.

[10] Y. Ling, S. Mahadevan, “Integration of Structural Health Monitoring and Fatigue Damage Prognosis,” Mechanical Systems and Signal Processing, Vol. 28, pp. 89-104, 2012.

[11] K. Worden, G. Manson, “Prognosis Under Uncertainty- An Idealized Computational Case Study,” Shock and Vibration, 15(3-4), pp. 231-243, 2008.

[12] C. Surace, K. Worden, “Damage Prognosis for Delamination of a Composite Plate,” Proceedings of the IMAC-XXVII, Orlando, FL, 2009.

[13] L. H. de Figueiredo and J. Stolfi, “Affine Arithmetic: Concepts and Applications,” Numerical Algorithms, Vol. 00, pp. 1-13, 2003.

[14] Stolfi, J, and L. H. de Figueirodo, Self-Validated Numerical Methods and Applications. Rio de Janeiro: Monograph for 21st Brazilian Mathematics Colloquium, IMPA, 1997.

[15] D. Broek, “Elementary Engineering Fracture Mechanics,” Kluwer Academic Publishers, 1982.

[16] M. A. Langoy and S. R. Stock, “Fatigue-Crack Growth in Ti-6Al-4V-0.1 Ru in Air and Seawater: Part I. Design of Experiments, Assessment, and Crack Growth Rate Curves,” Metallurgical and Materials Transactions, Vol. 32A, pp. 2297-2314, 2001.

[17] G. A. Kardomateas, A. A. Pelegri and B. Malik, “Growth of Internal Delaminations Under Cyclic Compression in Composite Plates,” Journal of Applied Mechanics and Physics of Solids, Vol. 43, pp. 847-868, 1995.

[18] Griffith A.A, The Phenomena of Rupture and Flow in Solids. Philos Trans Roy Soc Lon Ser A, Vol 221:163-198, 1921.

[19] ASTM D5528-13. Standard Test Method for Mode I Fiber-Reinforced Polymer Matrix Composites, 2013.

[20] F. Lahuerta, T. Westphal and Al, “Measuring the Delamination Length in Static and Fatigue Mode I Tests Using Video Image Processing”, Composites : Part B 63, 1-7, 2014.

[21] M.Y. Yarlagada S, AbuObaid A, R.D. Hager N. An Automated Technique for Measuring Crack Propagation During Mode I DCB Testing, In: Conference: SEM X International Congress and Exposition on Experimental and Applied Mechanics, 2004.

[22] Richter-Trummer V, Marques E, Chaves F, Tavares J, da Silva L, de Castro P. , “Analysis of Crack Growth Behavior in a Double Cantilever Beam Adhesive Fracture Test by Different Digital Image Processing Techniques”. Materialwissenschaft und Werkstofftechnik, 2011.

[23] O’Brien TK, Martin RH. , Results of ASTM Round Robin Testing for Mode I Interlaminar Fracture Toughness of Composites Materials NASA-TN-104222. Tech. Rep., Langley Research Center; 1992.

[24] Kageyama K, Hojo M. , Proposed Methods for Interlaminar Fracture Toughness Tests of Composite Laminates. In: Proceedings of the 5th US/Japan Conference on Composite Materials, Tokyo; p.227, 1990.

[25] ASTM E647-13a. Standard Test Method for Measurement of Fatigue Crack Growth Rates. 2013.

[26] O’Brien T K, Johnston W. M, Toland G. J., Mode II Interlaminar Fracture Toughness and Fatigue Characterization of a Graphite Epoxy Composite Material, 2010.